VACUUM ULTRAVIOLET LASER SPECTROSCOPY OF DIATOMIC HALOGEN AND INTERHALOGEN MOLECULES

ALEXANDER C. FLEXEN

DOCTOR OF PHILOSOPHY
UNIVERSITY OF EDINBURGH
1998

Vacuum Ultraviolet Laser Spectroscopy of Diatomic Halogen and Interhalogen Molecules

Alexander C Flexen

1998

Declaration

I hereby declare that this thesis has been composed by myself and, except where due acknowledgement is given, the work described in it is my own and was carried out at the University of Edinburgh and the Rutherford-Appleton Laboratory.

"...high energy photons spilling over into our atmosphere..."

sample from "High Energy Photons", Juno Reactor, Novamute Records, (c) 1996

Acknowledgements

It gives me great pleasure to be able to use this space to thank and acknowledge the support and help of a number of people who have either directly or indirectly been involved in the production of this thesis. Foremost of these must be my supervisor, Prof. Robert Donovan, from whom I have learned many valuable lessons during our regular discussions and I would like to thank him for the many opportunities afforded to me under his supervision. I must also mention and thank Dr. Kenneth Lawley for the initial offer of a Ph.D. and many instructive comments which kept the experimental work firmly on track. The wealth of experience and expertise of Dr. Trevor Ridley should not go unacknowledged and I am indebted to him for his support and understanding. Robert Maier, for his technical support, enthusiasm and the many informal discussions we had, also fits into this category. The work performed at the femtosecond laser facility at the Rutherford-Appleton Laboratory was done under the excellent guidance of Dr. Andrew Langley who always made my trips there very enjoyable and productive. Thanks also to Waseem Shaikh for his assistance in the lab. Finally, I am grateful to everyone in the Department who has contributed to making my time here educational, interesting and enjoyable, including Nasser, John, Pat, Marten, Mike, Paul and the other staff and students of the laser group.

As I mentioned above there are people who have indirectly been involved in the research and preparation of this Ph.D. over the last, approximately four years who have added to and enhanced my learning experience during that time and I must mention them briefly here. Firstly my brother Christo who has always been there, my "brothers" Chris, Mark, Merlin and Neil, also Jas, Carrie-Anne, Anna, Claire, Trudy and her troops and Helen. All of you are the best. Last, but certainly not least, my parents- thank you for all you've done.

I must also take this opportunity to thank the EPSRC for funding my CASE award Ph.D. over the three years.

Abstract

The Rydberg and ion-pair states of Cl_2, Br_2, I_2, ICl and IBr have been studied using a range of laser-based spectroscopic techniques, in the vacuum-ultraviolet (VUV) energy region. The [2+1] resonance enhanced multiphoton ionization (REMPI) spectrum of Br_2 has been re-examined in the region 56 000-86 000 cm^{-1}. Rydberg series, previously assigned to components of the ns Rydberg states have been reassigned to components of the (n-2)d Rydberg states, for $n \geq 6$. The lowest 5s Rydberg state components on each ionic core remain unchanged, based on energetic considerations. The Ω values of the Rydberg states were deduced from rotational band contour analysis and from intensity ratios under linear and circular polarization. A propensity rule for assignments based on two Ω components with significant singlet character (Ω=0 and $\Omega = 2$), on each ionic core, was determined in terms of the microconfigurations for the Hund's case (c) states. As an exception, triplet components (Ω=1) are also observed for the lowest n in a particular Rydberg series (n=4 for the d-series in Br_2).

This reassignment prompted a reinvestigation of the one- and two-photon spectra of the halogen and interhalogen molecules, Cl_2, I_2, ICl and IBr in terms of the propensity rules developed for Br_2. The one-photon spectra of I_2 and ICl were recorded using VUV laser radiation, generated by four-wave mixing in Kr gas. Ion-pair formation (X^++Y^-) *via* predissociation of Rydberg states was observed from all states seen in the one-photon absorption spectrum of each molecule. Spectra were recorded from the ion-pair threshold up to the ionization limit. The field-lowering effect induced by the high electric field in the extraction region of the time-of-flight mass spectrometer was investigated with I_2. Predissociation in I_2 and ICl is discussed in terms of a two-electron exchange mechanism connecting the electronic configurations of the Rydberg and ion-pair states.

The nonlinear response of atoms in a high intensity regime to produce high (odd) harmonic orders of an applied 750 nm, 50 fs laser source was investigated at the Rutherford-Appleton Laboratory using two experimental arrangements. The first of these involved focusing the fundamental radiation into a cell containing Ar or Xe at pressures up to 1 atm. The 5th harmonic (150 nm) was the highest order observed and the conversion efficiency of each harmonic was characterised in terms of laser power dependence, cell pressure, focusing conditions and medium used. A second, windowless arrangement, introducing the gas to the laser focus *via* a pulsed jet allowed an extension of the range of harmonic orders. In this case output up to the 7th harmonic (107 nm) was observed. The harmonic output was characterised in terms of the photon yield and conversion efficiency and optimised to test the suitability of this technique as a source of VUV radiation for spectroscopic application.

Contents

3 The [2+1] REMPI spectrum of Jet-Cooled Br_2 89

4 Ion-Pair Formation from I_2 Using VUV Laser Radiation 124

List of Tables

List of Figures

Chapter 1

Introduction and Background Theory

1.1 General Introduction and Field of Study

Spectroscopy is concerned with the observation and understanding of the interaction of electromagnetic radiation with matter. Spectroscopic techniques using electromagnetic radiation sources ranging in wavelength from radio waves to X-rays have been extensively applied to probe the nuclear, molecular and electronic structure of many molecules and the intra- and intermolecular processes occurring within or between them.

The work discussed in this thesis concentrates mainly on one region of the electromagnetic spectrum, the vacuum-ultraviolet (VUV) region which spans a range of wavelengths from 200 nm to below 100 nm. Many molecules have a variety of excited states such as Rydberg, ion-pair and autoionizing states in this energy region and the attendant dynamical processes may be initiated and probed by VUV excitation. Two experimental arrangements were developed to generate such radiation, one of which was successfully applied to study the spectroscopy of the diatomic halogen molecules, I_2 and ICl. Further complementary spectroscopic work was performed on the Br_2 molecule using a multiphoton excitation technique, resonance enhanced multiphoton ionization (REMPI). Common to each experiment discussed here, however, is the nonlinear response of matter to applied radiation, as will be explored further in later sections.

This chapter is divided into three distinct parts each introducing the theory and related work relevant to the results obtained from the experiments performed. The first section details the theoretical and experimental aspects of generating VUV laser radiation by the technique of four-wave mixing in a nonlinear medium. The following section details the recent developments in the technique of high-harmonic generation as a source of short wavelength radiation feasibly extending from the VUV to the soft X-ray region of the electromagnetic spectrum, which again exploits the polarization response of nonlinear gaseous media only using intensities at higher orders of magnitude than used for four-wave mixing. This is relevant to experiments carried out at the Rutherford-Appleton Laboratory and discussed in the final chapter. The final section outlines the electronic structure and spectroscopy of the halogen and interhalogen molecules studied in this work at energies corresponding to VUV frequencies, achieved using one- or two-photon excitation.

1.2 Generation of VUV by Four-Wave Mixing

Coherent, narrow bandwidth radiation with wavelengths in the vacuum-ultraviolet region of the electromagnetic spectrum (200 - 100 nm) can be generated by the process of four-wave mixing (FWM). The simplest occurrence of FWM arises when the tensors of three oscillating electric fields with the same frequency, ω, mix or superimpose in a medium and generate a polarization response in the medium to produce a fourth field of frequency, 3ω, in the process known as third harmonic generation (THG)[1,2].

1.2.1 Polarization response of nonlinear media

All media respond to an applied electric field by displaying an induced polarization. This induced polarization is often expressed in terms of the function which describes the oscillation of the applied electric field, $E(\omega)$:

$$P(\omega) = \chi^{(1)}.E(\omega) + \chi^{(2)}.E(\omega).E(\omega) + \chi^{(3)}.E(\omega).E(\omega).E(\omega) + ... \qquad (1.1)$$

where $P(\omega)$ is the induced polarization tensor and $\chi^{(n)}$ is the nth order susceptibility term of the medium. This non-linear relationship between applied electric field tensor and induced polarization tensor can produce a resultant $P(\omega)$ function with a component which contains a $\cos(3\omega)$ term, provided the $\chi^{(n)}$ coefficient is nonzero for n=3. This component of the induced polarization, therefore, represents the source of radiation generated in the medium with frequency 3ω (THG). Figure 1.1 shows a schematic diagram of the third harmonic generation process occuring within a nonlinear medium.

It is by a similar mechansim that second harmonics of applied radiation are generated in crystals, whereby the lowest nonzero, nonlinear component of the polarizability tensor is determined by the coefficient $\chi^{(2)}$, the second order susceptibility term, in noncentrosymmetric systems. The conversion becomes efficient when laser radiation is applied (particularly pulsed sources) since the intensity developed and hence the square of the amplitude of the interacting electric field $(|E(\omega).E(\omega)|)$ yields a large component of frequency 2ω. However, a number of factors limit the practicability of using crystals for harmonic generation. Foremost of these is the wavelength range in which crystals operate which is limited to wavelengths in the far UV above 200 nm. Secondly, due to low thermal stability of crystals, breakdown of the medium limits the available conversion efficiency when increasing the intensity of applied radiation.

Suitable media for third order harmonic generation are gaseous species, particularly those with high polarizabilities, e.g. inert gases, gaseous heavy metal atoms and alkali ions[1]. The third order polarizability of these species is proportional to the $\chi^{(3)}$ susceptibility term in equation 1.1, hence a high value of this coefficient suggests a high conversion efficiency for third harmonic generation. However, other factors must be considered when observing THG in practice and these will be discussed later. These systems are isotropic and, by virtue of their centrosymmetry, do not possess nonzero second order nonlinear terms. The lowest nonzero, nonlinear term is $\chi^{(3)}$ thus the nonlinear polarization response is due to three electric fields interacting with the medium. Suitable gaseous media have high thermal stabilities, high transmission of VUV wavelengths and low birefringency or distortion of applied and output beams.

In principle, third harmonic generation can be performed simply by focusing a pulsed UV or visible laser into a static cell containing the nonlinear medium at pressures of the order 0.1 atm. Optimum conditions for THG and other four-wave mixing processes are controlled by the beam geometry, optics and the nature and environment of the nonlinear medium used in experiment. The intensity of generated third harmonic can be given by equation 1.2

$$I(3\omega) = N^2(\chi^{(3)})^2 I(\omega)^3 F(b\Delta k) \tag{1.2}$$

where the phase shift $\Delta k = k(3\omega) - 3k(\omega) = \frac{3\omega}{c}[n(3\omega)\text{-}n(\omega)]$.

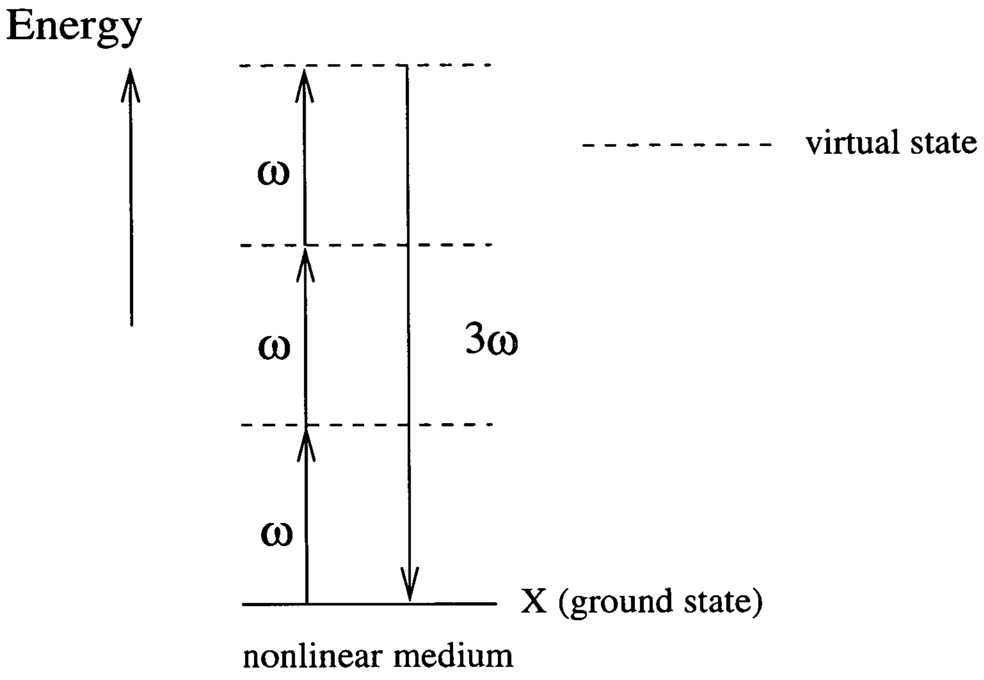

Figure 1.1: Third harmonic generation.

In equation 1.2, N is the number density of particles in the medium. The term Δk describes the phase shift or phase mismatch of the incident fundamental and generated third harmonic beams in terms of the difference in wavevectors between the generated radiation and the applied radiation. The wavevector k of radiation in the nonlinear medium is directly proportional to the refractive index of the medium at the wavelength of the radiation. The confocal parameter, b, measures the degree of focusing of the incident beam in the medium and is given by equation 1.3:

$$b = \frac{2\pi a^2 n}{\lambda_0} \tag{1.3}$$

(with a, the beam-waist radius; n, the refractive index; λ_0, the vacuum wavelength). The product $N^2F(b\Delta k)$ is considered when determining the intensity of generated radiation since varying gas density also varies the refractive index of the medium and hence alters the function F. Decreasing gas density may result in the competing process of multiphoton ionization dominating, with a consequent reduction in conversion efficiency.

1.2.2 Tunable VUV by four-wave mixing

Limitations of third harmonic generation

The apparently obvious solution to generating tunable VUV would be to apply a continuously tunable laser source, such as a pulsed dye laser, to the nonlinear gaseous medium and observe third harmonic generation over the range of applied wavelengths. However, the severe limitation on THG comes from phase mismatching of the generated VUV wavelengths and that of the applied source wavelength. This is due to the variation of refractive index in the medium used with wavelength. Under focused conditions, THG is forbidden[3] whenever the refractive index of the medium at the VUV wavelength, $n(3\omega)$, is greater than $n(\omega)$, the refractive index of the medium at the frequency of the applied radiation. Third harmonic generation may only occur if the frequency of the VUV radiation generated is to higher energy of a resonance in the nonlinear medium; in a region of so called negative dispersion. Here, the negative dispersion in the medium can be compensated by the positive wavevector mismatch incurred in third harmonic generation. This limits the range of tunability affordable by the process and therefore a more efficient four-wave mixing scheme is desirable. This is provided by resonant four-wave mixing.

Resonant four-wave frequency mixing

The conversion efficiency of VUV generation can be considerably enhanced when a real state in the nonlinear medium at energy ΔE is accessed by a resonant two-photon transition, such that $\Delta E{=}2\omega$. resonant with a two-photon transition in the generating medium. This can be derived in terms of the third order susceptibility term, $\chi^{(3)}$, which appears in the polarizability equation 1.1. This term varies with the electronic potential energy of the particles which constitute the nonlinear medium as shown in figure 1.2 for the lithium atom. The function clearly shows the $\chi^{(3)}$ term increases by several orders of magnitude at energies corresponding to resonances in the atom.

Since the third order polarization response (in gases) is proportional to the product of three oscillating electric fields ($E(\omega_1$ ... $\omega_3)$) and the susceptibility term, $\chi^{(3)}$, then it is possible to generate frequencies, ω_{gen}, according to equation 1.4.

$$\omega_{gen} = \omega_1 \pm \omega_2 \pm \omega_3 \tag{1.4}$$

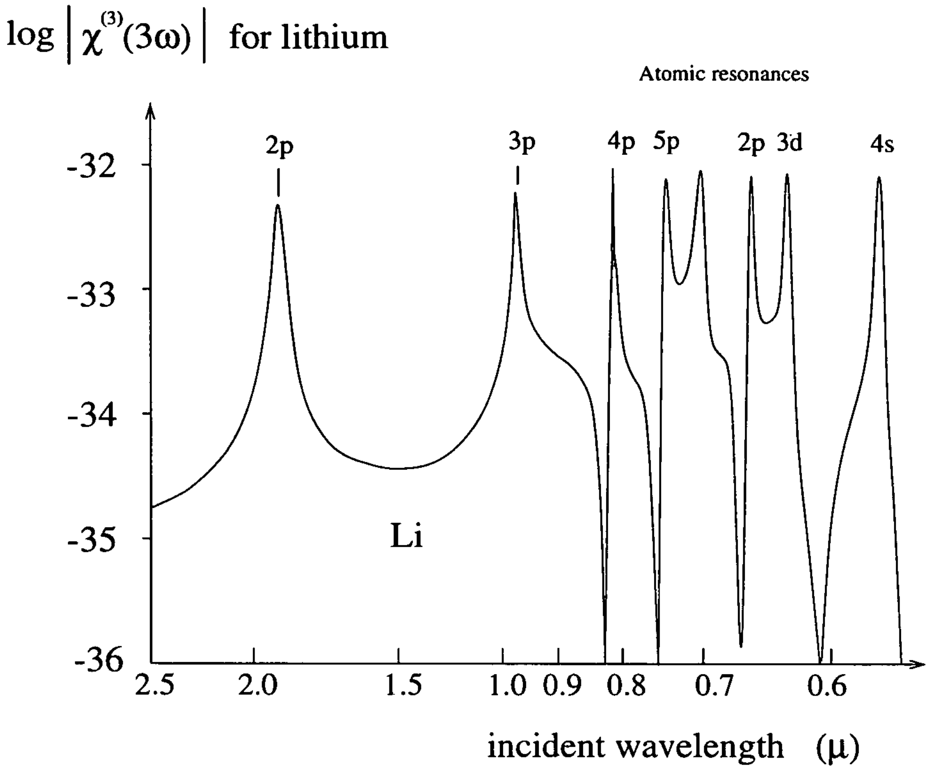

Figure 1.2: Third order susceptibility of Li versus incident wavelength.

The increase in $\chi^{(3)}$ at resonances ensures that the applied radiation has a correspondingly large conversion efficiency to its polarization response.

However, if a system is considered, with one input frequency, ω, then three possible resonant transitions are possible; one-photon, two-photon and three-photon resonance with transitions in the medium. Figure 1.3 shows that one-photon resonant and three-photon resonant transitions in the medium result in reabsorption of the fundamental, or applied, frequency and third harmonic frequency, respectively [1]. No reabsorption occurs for resonances at the two-photon level (figure 1.4) and hence a high third harmonic conversion efficiency would

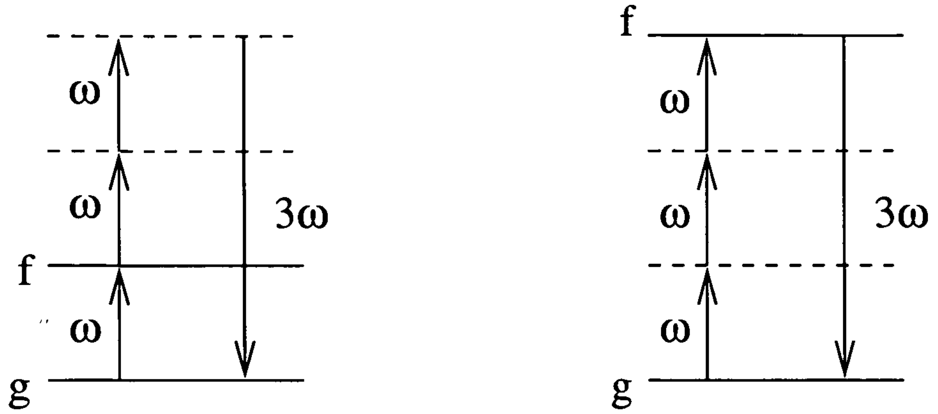

-resonance at ω ; $\omega = \Omega_{fg}$
→ absorption of fundamental

-resonance at 3ω ; $3\omega = \Omega_{fg}$
→ absorption of third harmonic

Figure 1.3: Resonant four-wave mixing processes resulting in reabsorption of fundamental or third harmonic.

be expected. However, if the three-photon frequency, 3ω, exceeds the ionization potential of the nonlinear medium then the channel leading to multiphoton ionization competes with four-wave mixing.

Returning to the question of tunability, it is apparent that by fixing the frequency of the applied source to be resonant, with two coherent photons, with a transition in the medium, then any attempt to scan this frequency will shift the excitation energy off-resonance and the intensity enhancement of the generated radiation will be lost. To introduce tunability, two colours ω_1 and ω_2, are used where ω_1 is fixed to be two-photon resonant with a transition in the medium and ω_2 is scanned. This process is known as resonant sum frequency mixing (RSFM), shown schematically on figure 1.5.

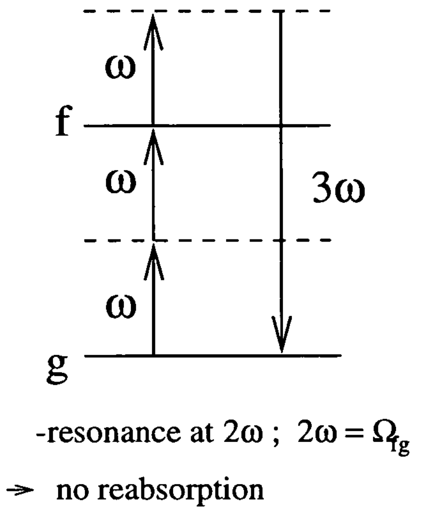

Figure 1.4: Two-photon resonant four-wave mixing process with no reabsorption.

The rules for phase matching are the same for THG and RSFM and therefore the process will only work for generated VUV frequencies to the blue of resonances in the nonlinear medium. Photon fluxes obtainable from RSFM are $\leq 10^{11}$ photons pulse^{-1} with millijoule pulses.

Resonant four-wave difference-frequency mixing

The schematic diagram for the resonant four-wave difference-frequency mixing (RDFM) process is shown on figure 1.6. Observing the VUV radiation produced by the difference between the resonant frequency in the medium and the second, tunable frequency, down-pumped from the resonance line, is experimentally advantageous [4–6]. The rules applied to the phase matching of fundamental and generated beams are less rigorous and phase matching is observed for both

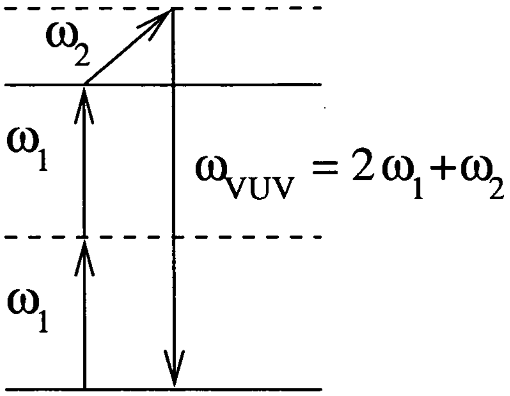

Figure 1.5: Schematic diagram of the resonant sum-frequency mixing process, where $\omega_{VUV} = 2\omega_1 + \omega_2$.

positive and negative values of Δk, making it possible to continuously tune ω_2 through the electronic potential of the nonlinear medium. RDFM is also found to be generally more efficient than RSFM when the same two-photon resonance is used. Photon fluxes obtainable are 10^{11}-10^{12} photons pulse^{-1}.

1.2.3 RDFM experimental details

Experimental considerations for optimising the generating efficiency of the VUV can be grouped according to the following factors; applied pulse energies, the optics used and pressure dependence of the chosen medium. For this discussion, the resonant transition involved in the RDFM process will be 4p-5p[1/2,0] in krypton (fig. 1.7) as carried out by Marangos *et al.* [4].

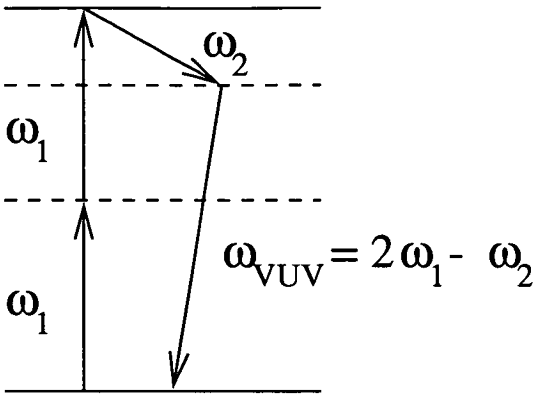

Figure 1.6: Schematic diagram of the resonant difference-frequency mixing process, where $\omega_{VUV} = 2\omega_1$ - ω_2.

This scheme represents tunability from 125-145 nm using λ_T in the range 400-700 nm. Phase matching using a buffer gas is employed when scanning in the range 121-123 nm since losses occur due to absorption of λ_{VUV} at the lower-lying 4p-5s transition. In this region, krypton is negatively dispersive which is compensated for by mixing with argon, which is positively dispersive in this region, at a ratio of pressures P_{Ar}:P_{Kr} of 3.0 : 1.

A diagram of the typical experimental arrangement is shown on figure 1.8. The arrangement consists of two dye lasers (excimer pumped) with output beams combined and directed collinearly into the four-wave mixing (FWM) cell and monochromator assembly. The beams are telescopically collimated and focused near to the exit window of the FWM cell, through which they pass into a monochromator. The figure shows a diffraction grating acting as the dispers-

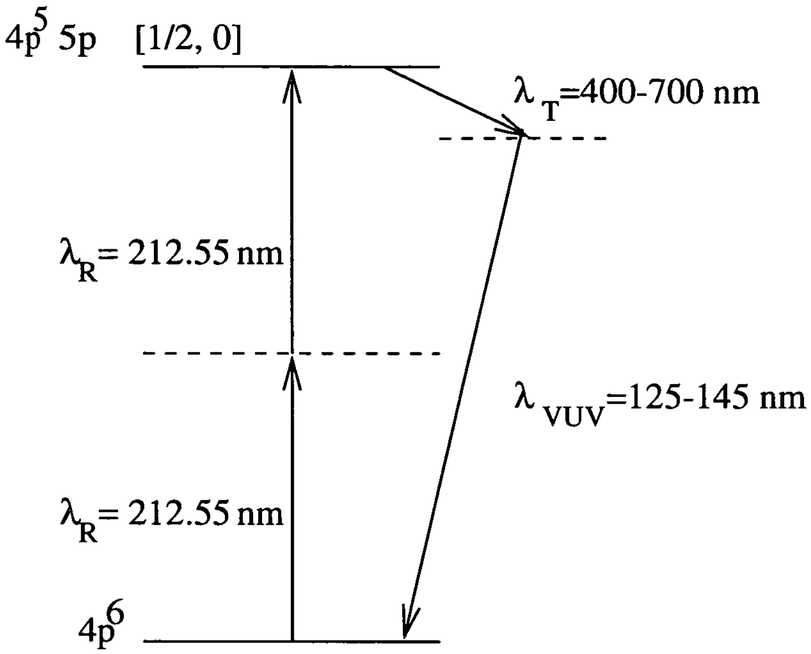

Figure 1.7: Four-wave difference frequency mixing in krypton.

ing element. However, a variety of methods, for both tuning output VUV and separating the VUV from the applied wavelengths, are available which include a system of prisms, a single prism or the grating configuration shown. A number of properties of prisms make these optical devices preferable to gratings: high tolerance to radiation damage and high throughput. In contrast, gratings damage easily if subjected to high intensity irradiation and exhibit changing efficiency with wavelength and polarization. Higher dispersion in prisms allows easier separation of wavelengths.

The grating is tilted through angles corresponding to VUV wavelengths at a certain order. Vacuum-UV output is monitored by directing a portion of the

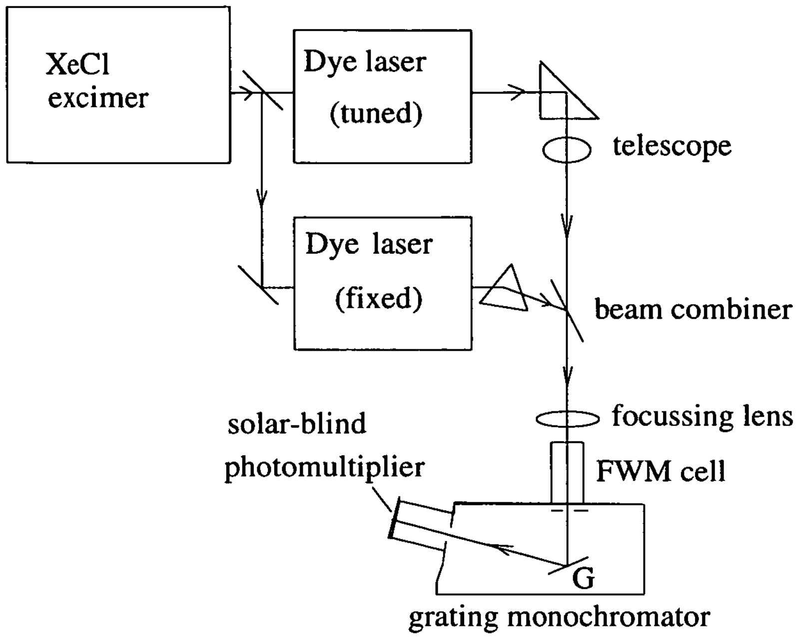

Figure 1.8: Schematic of experimental arrangement for RDFM experiments.

throughput into a solar-blind photomultiplier, *via* a partially reflecting mirror. A new material for use in VUV photodetectors has been developed by de Cesare *et al.* [7] made from hydrogenated amorphous silicon and silicon carbide on a glass substrate, which effectively eliminates photodetection of UV and visible wavelengths and has a high quantum efficiency for wavelengths extending into the XUV. Optical components such as windows, lenses and prisms, in the beam path of VUV radiation are typically constructed using crystalline MgF_2 or LiF which have transmission ranges extending to 120 nm and 110 nm, repsectively. Magnesium fluoride is generally favoured as it is somewhat more stable and less hygroscopic than lithium fluoride.

The characteristics of the input beams, λ_R and λ_T, are important for optimising the conversion efficiency to VUV. The two collinear beams are focused with, typically, a reasonably long focal length lens (100 - 300 mm) to provide a soft focus. At the focusing stage, each beam is conferred a confocal parameter which can be determined using equation 1.3. Since two confocal parameters, b_R and b_T, are set up, by virtue of the different wavelength of each applied beam, then the single b value contained in the function $F(b\Delta k)$ in equation 1.2 can be replaced by the ratio of confocal parameters $b{=}b_R/b_T$ of the resonant and tuned input beams. The respective pulse energies are ratioed such that the intensities developed at the focus are equally matched, e.g. for $b{=}0.25$ then it follows that the pulse energies are given by $E_R/E_T = 0.25$.

With the correct optics and laser beam characteristics chosen, the environment of the nonlinear medium controls the conversion efficiency of the RDFM process. Complex calculations are required to model the pressure dependence of the medium on the VUV output. The relationship has been reported in a simplified form in terms of b and Δk (equation 1.5). Figure 1.9 shows the pressure dependence of VUV intensity.

$$P_{VUV} \propto N^2 e^{-b_R C N} (C = \Delta k/N) \tag{1.5}$$

(where C is the phase mismatch per atom). An optimum number density, $N =$

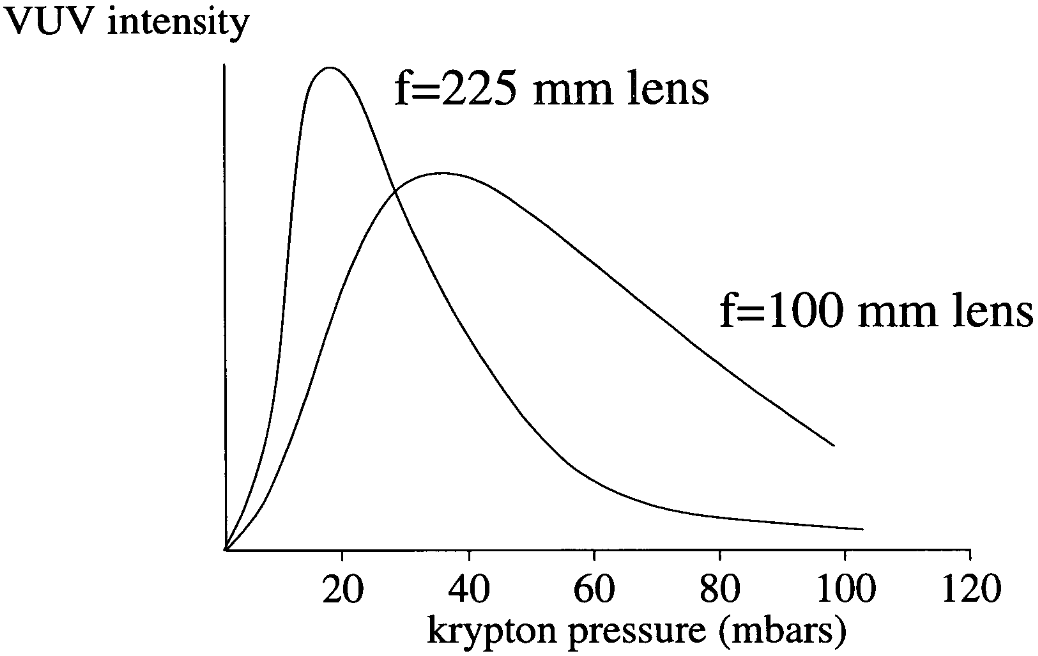

Figure 1.9: Variation of VUV intensity with krypton pressure for two different focal-length lenses.

$2/b_R C$ is derived from equation 1.5.

Phase mismatching (i.e. Δk nonzero) still occurs in Kr in RDFM experiments but restrictions on the value $F(b\Delta k)$ are not imposed. However, F is still maximised when phase matching is present ($\Delta k = 0$), therefore, it may be necessary to introduce a buffer gas which compensates for positive and negative dispersion in the medium at the VUV wavelength being scanned.

Resonant four-wave mixing of conventional laser radiation in a polarizable medium is a useful technique for providing a tunable, intense and coherent vacuum ultraviolet light source which has been used in practical applications in spectroscopy [8,9].

1.3 High-Order Harmonic Generation

With the advent of high power, short pulse length laser systems it has been possible to probe the response of nonlinear media to applied radiation at intensities several orders of magnitude higher than used for four-wave mixing and third harmonic generation techniques. Femtosecond sources with pulse lengths $\leq 10^2$ fs when focused can develop intensities of $10^{13} - 10^{18}$ W cm^{-2}. The experiments described in section 1.2 of this chapter on four-wave mixing and third harmonic generation operate at saturation intensities of $\leq 10^{12}$ W cm^{-2}, therefore, it is evident that at these higher intensities, the conventional polarization response of typical nonlinear media given in equation 1.1 is expected to be perturbed in some way.

This is manifested in the process of high-order harmonic generation [10–12], whereby several photons of an intense, applied radiation source may be absorbed simultaneously in a nonlinear medium with a consequent reradiation of several odd-number harmonics or orders of the applied radiation, shown schematically in figure 1.10. Typically, the harmonic spectra produced show characteristic features (see figure 1.12) and a number of well defined factors influence the range

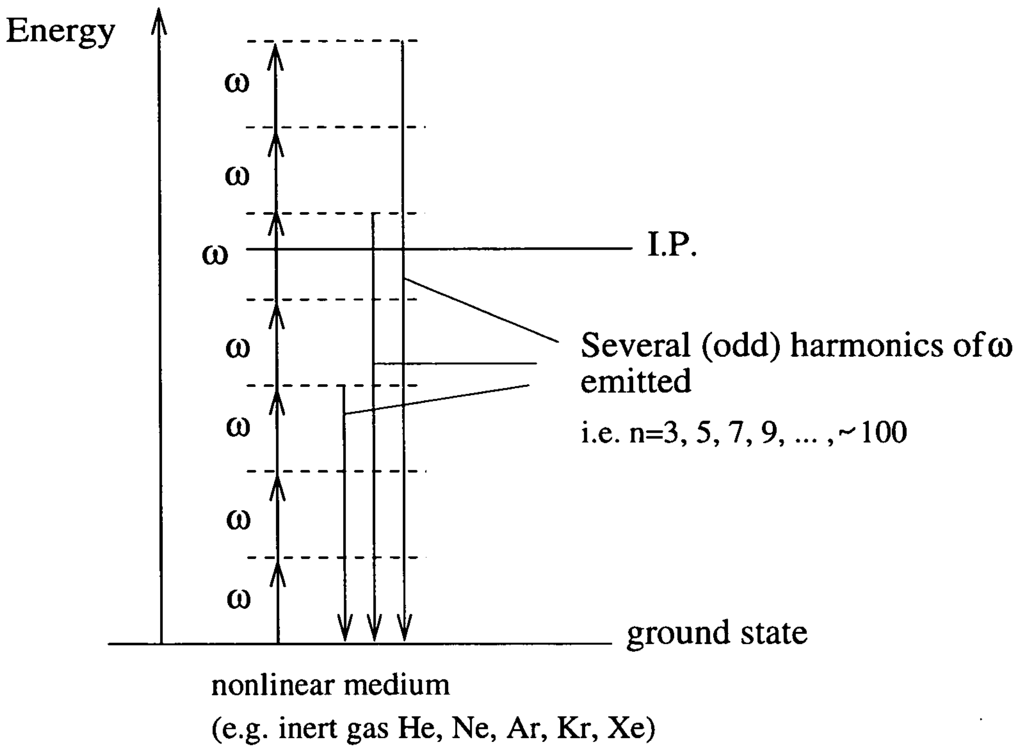

Figure 1.10: Schematic diagram of processes in high-order harmonic generation.

and intensity of output harmonics. High harmonic generation provides a route to generating coherent, high brightness radiation extending into the soft X-ray spectral region, with wavelengths as short as 2.7 nm reported [13]. This exceeds the operational capabilities of synchrotron sources with the advantage of being available as a compact, table-top source. Certain terawatt (10^{12} W) sources have a comparable bandwidth to synchrotron radiation, determined by the Fourier transform limit of pulses with duration in the picosecond range. Shorter pulse length sources operating on the subpicosecond or femtosecond timescale have found useful applications in the study of molecular dynamics by pump-probe experiments. Several applications to molecular systems using high harmonics with picosecond and subpicosecond pulse lengths have been reported.

1.3.1 High power lasers

In order to develop the high intensities required for the harmonic generation process (I >10^{13} W cm^{-2}) a high power laser source must be used if a significant focal volume is to be achieved. Large scale laser sources with pulse energies in the kJ range and pulse lengths of ns duration can operate with peak powers in the terawatt range, but require special facilities. With the development and improvement of ultrashort pulse length laser systems, it has been possible to achieve these very high peak powers with low pulse energies of the order 0.1-1 J using table-top laser systems on a scale more suited to a moderately sized laboratory [14].

Suitable media for generating short pulse durations are those which have a spectral bandwidth large enough to support the transform limited bandwidth of the pulses (typically 20-40 nm) and include excimers and dyes. These media may be limited in their use as amplifiers or oscillators by low saturation fluences or thermal stability. Titanium-doped sapphire (Ti:S) [15] is a widely-used solid state laser medium which possesses a very broad frequency bandwidth of >300 nm, with a peak around 800 nm and hence can, in principle, support pulses of a few fs in length [16]. The material also has the advantage of having a high thermal conductivity and mechanical rigidity allowing a wide range of operational capability and ease of handling.

However, optical components are easily damaged when subjected to radiant intensities greater than 10^9 W cm^{-2}, hence to amplify or even propagate pulses with peak powers at the TW level requires large beam diameters, at the expense of requiring large crystals or rods. This limitation has been overcome with the introduction of the technique known as chirped pulse amplification (CPA) [17–20] where low energy ultrashort pulses are first stretched temporally by a factor of around 1000, by multiple passes through a pair of gratings to form a well defined frequency "chirp" of the pulse. This greatly reduces the peak intensity before the amplification stage in the gain medium and allows the optical component to be kept relatively small since a large beam diameter is no longer required. The amplified, stretched pulse is then recompressed temporally to the desired pulse length and is output as an ultrashort, very high peak power, clean pulse. CPA is described in relation to the table-top femtosecond laser facility at the Rutherford-Appleton Laboratory in more detail in Chapter 2.

1.3.2 Nonlinear response of atoms at high intensities of radiation

Atoms in a strong laser field can produce coherent radiation at energies exceeding the ionization potential (figure 1.10). In the weak-field limit, the atomic response to an applied field is treated by the lowest-order perturbation theory [21]. Here, the polarization of the medium induced by the laser field at the q^{th} harmonic is expressed as $\chi^q|E|^q$, the product of the q^{th} order susceptibility term and the q^{th} power of the laser electric field. For intensities $\leq 10^{12}$ W cm^{-2}, the n^{th} order response is vanishingly small due to diminished χ^n values for n>3.

At laser intensities $\geq 10^{13}$ W cm^{-2}, the atomic response departs largely from the weak-field limit and the atom becomes strongly perturbed by the radiation field. For intensities in the range 10^{14}-10^{18} W cm^{-2}, the field strength approaches that of the Coulombic potential or binding energy of the atom (ca. 10^9) V cm^{-1}. A barrier is formed between the atomic potential and the external laser field which lowers the binding energy of the atom and through which electrons excited by the laser field may tunnel by the process of tunnel ionization. Multiphoton ionization (MPI) may also occur [22] by the absorption of sufficient photons simultaneously to exceed the ionization potential (IP) of the atom. The extent to which either process contributes to the removal of an electron from the atomic potential depends on the IP of the atom and the optical pulse duration. An electron liberated from the atomic potential oscillates in the laser field thus conferring a kinetic energy to the particle the average of which is referred to as the ponderomotive energy, U_p. This quantity is related to the wavelength, λ and intensity, I, of the exciting source by equation 1.6.

$$U_p/\text{eV} = 9.33.10^{-14}.I\lambda^2 \tag{1.6}$$

This extra energy in the system therefore raises the ionization potential of the atom but it is important to remember that this represents the average kinetic energy of the electron in the laser field. Treating the motion classically it has been derived that the maximum kinetic energy acquired by the electron is $3.2U_p$ [23], hence the total, maximum energy above the zero-point level is I_p+$3.2U_p$, where I_p is the ionization potential of the atom. Harmonic generation occurs when the tunnel ionized electron which is oscillating in the laser field returns to the nucleus by recombining with the ionic core in the ground state. The energy or frequency of the harmonic is an odd multiple of a frequency within the bandwidth of the laser pulse and has a maximum value, E_{max}, in the single-atom case given by equation 1.7.

$$E_{max} = I_p + 3.2U_p \tag{1.7}$$

It will be shown in a later section that in practise the maximum extent of the harmonic spectra produced is somewhat lower than this due to phase matching requirements in a bulk sample of the medium.

1.3.3 Experimental details

Harmonic generation is experimentally very similar to third harmonic generation. In both cases harmonics are generated by focusing a pulsed laser into a cell containing some nonlinear medium with the output separated from the fundamental radiation and dispersed by some tuning element. Detection is typically provided by either a solar-blind photomultiplier tube or, for high energy radiation, a microchannel plate (MCP), electron multiplier (EM) detector or charge-coupled device (CCD) which has been developed to provide absolute energies of output harmonics [24]. Figure 1.11 shows a typical experimental arrangement for harmonic generation (Miyazaki *et al.*, [25]). The medium is usually introduced into the laser focus by a pulsed nozzle with the gas efficiently extracted by diffusion pump in order to maintain a high vacuum for safe operation of the MCP or EM detector, in a windowless system. Alternatively a thin cylinder housing the medium may be used [26]. A double-ended hole in the cylinder allows throughput of the applied and generated radiation with the medium at much lower pressures than achieved in a jet. Furthermore, alignment with the laser beam is easier when using this device.

1.3.4 Experimental results

Many experiments have been performed on characterising the output of generated harmonics in terms of the applied laser intensity, pulse duration, wavelength and environment and type of medium used [27–36]. Typically, the rare gases are often used as the nonlinear medium [27–30], given their ease of handling and electronic stability with respect to ionization. The alkali metal ions, Li^+, Na^+ and K^+ [31], which share the same electronic structure as the rare gas atoms have been used

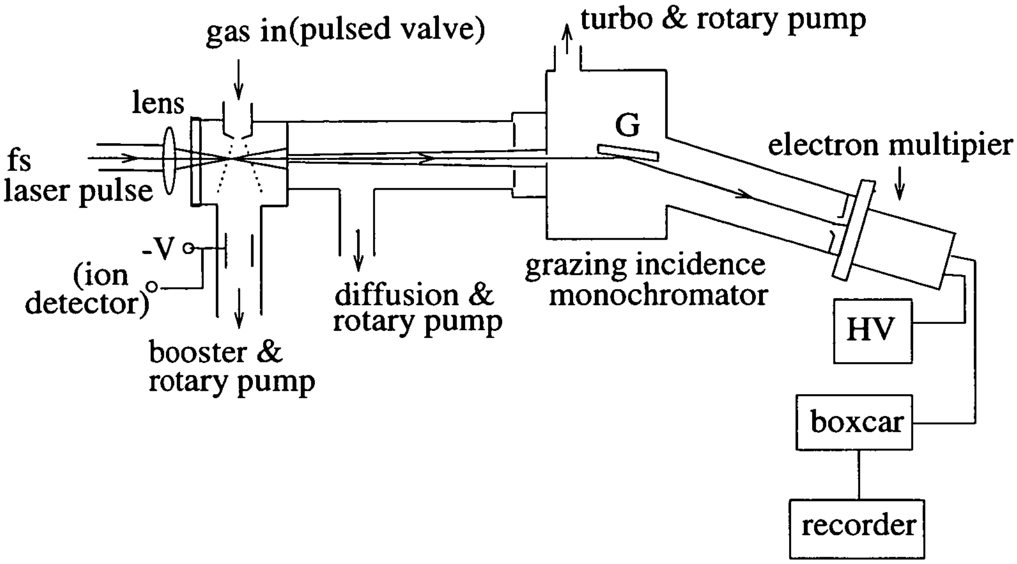

Figure 1.11: Schematic diagram showing example of typical experimental arrangement for generating and observing high-order harmonics.

and respond in a similar way. These species have much greater ionization potentials, theoretically extending the range of observable harmonic orders, however, ions are more difficult to produce and handle than neutral gaseous species. Conversions efficiencies of harmonic generation in molecular media such as diatomics (O_2, H_2, N_2, CO) [32] and simple organic molecules (C_4H_{10} and C_4H_6) [33] have also been investigated but are generally found to be less efficient than rare gases or rare gas-like ions. Other variable parameters investigated include atomic density [34], laser intensity [35] and ultrashort pulse duration [36].

Peak laser intensities are dependent to a large extent on pulse duration but are found to lie in the range 10^{13}-10^{17} W cm^{-2} with pulse durations from as low as 25 fs [35] up to 40 ps, using a variety of sources operating with peak wavelengths in the infrared (e.g. Nd:YAG laser at 1064 nm) to the ultraviolet (e.g. KrF excimer laser at 248 nm). It is found that the variation of harmonic yield with laser intensity is strongly dependent on the intensity regime presented. At lower intensities, harmonic yields vary according to conventional nonlinear polarization response as $|I|^q$, where I is the laser intensity and q is the harmonic order. Here, only the lower harmonic orders are observed which fall rapidly in strength with increasing order up to around q=5 or 7. As the laser intensity is increased, successive higher harmonic orders appear, with the previously lowest observed orders joining a plateau region of harmonics of approximately uniform intensity. As the laser intensity is increased still further, higher orders of harmonics join the plateau until a maximum energy is reached and there is an abrupt 'cut-off' in the harmonic spectrum. This cut-off energy is due to the combination of the ponderomotive potential and ionization potential of the atom described in equation 1.20. Harmonic spectra have a characteristic structure comprising these three features. Figure 1.12 shows a schematic representation of a typical harmonic spectrum including the sharp, initial fall in intensity of the lowest order harmonics before joining an extensive plateau region of harmonics with approximately uniform intensity, terminated by an abrupt cut-off. At higher laser intensities, the ionization rate increases until a saturation intensity is attained at which point, no further contribution to the HG process can be made. The saturation intensity is specific to the medium used, with the heavier rare gas atoms such as Xe having a lower value than the lighter atoms such as He. This

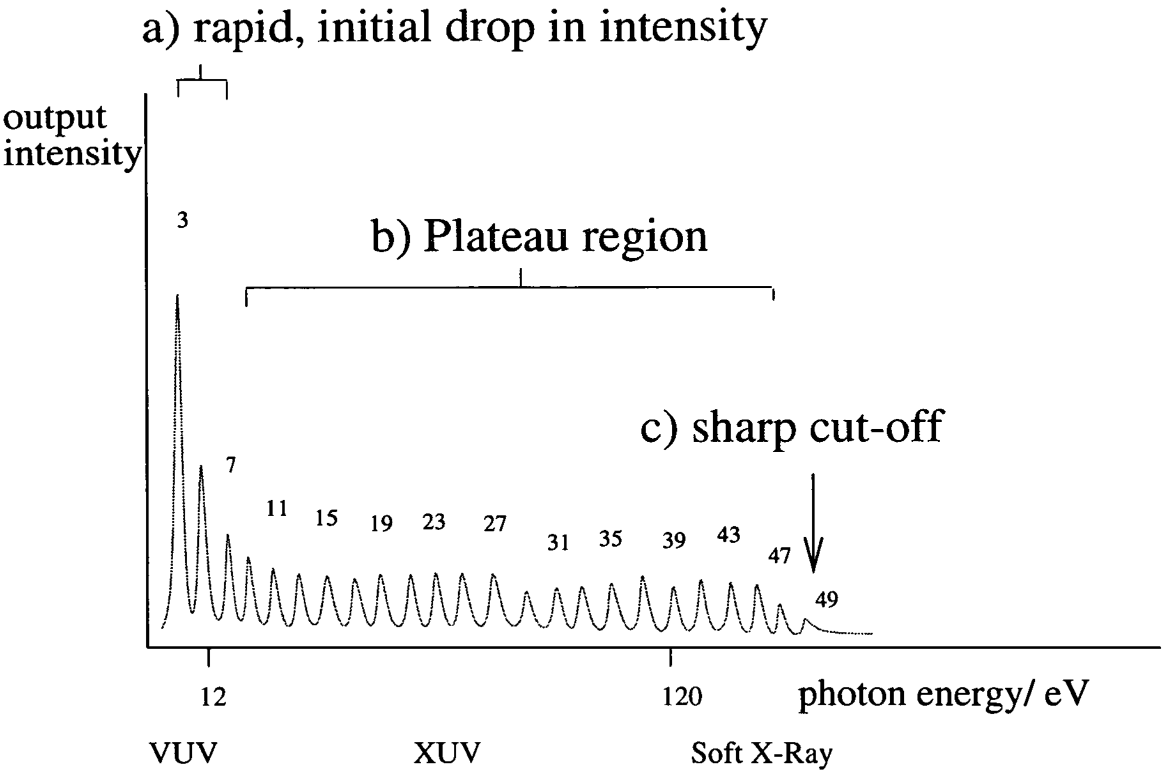

Figure 1.12: Representation of a typical harmonic spectrum.

explains why the plateau of the harmonic spectrum generated in He or Ne is much more extensive than is observed for Xe. However, higher conversion efficiencies are observed for the heavier rare gases due to higher recombination cross-sections.

The plateau may also be extended by choosing a long wavelength laser source such as an Nd:YAG or Ti:sapphire over an excimer laser operating in the ultra-violet. Decreasing pulse lengths have also been shown to have a marked effect on the location of the cut-off [35]. The ponderomotive energy, U_p, is related to λ^2, according to eqn. 1.19. Electrons oscillating within a high frequency, short-wavelength laser field have a lower probability of being driven back to the nucleus than those within a low frequency, long wavelength laser field.

Table 1.1 contains a summary of some of the experimental parameters used and results obtained from a number of harmonic generation experiments; giving the maximum harmonic order achieved for the combination of laser parameters (wavelength, peak intensity developed and pulse duration) and medium used. It is important to note that the experimental results presented in the table do not represent the optimum values produced from the experimental parameters listed. Instead, a number of other factors must be considered which limit or compete against the efficiency of the harmonic generation process.

1.3.5 Factors affecting conversion efficiency of output harmonics in HG experiments

A number of factors arising from the nature of the optics, beam geometry, environment of the generating medium and competing processes in the medium which limit or enhance the output of harmonics are presented and discussed below. These factors are grouped into headings.

Confocal parameter

The confocal parameter, b, of the system provides a value for the degree of focusing of the applied beam and is given in equation 1.3. The magnitude of b

Laser (λ)	nonlinear medium	I/W cm^2	E/mJ	δt	maximum harmonic	ref.
XeCl (308 nm)	He	3 x 10^{15}	30	340 fs	15	25
Ti:Sapph. (806.5 nm)	Ne	10^{15}	15	125 fs	109	29
Ti:Sapph. (794 nm)	Ne	6 x 10^{14}	100	250 fs	83	23
Nd:YAG (1064 nm)	Xe	10^{13}	-	40 ps	13	30
Ti:Sapph. (806.5 nm)	He	3 x 10^{15}	-	120 fs	69	28
KrF (248 nm)	He	6 x 10^{17}	-	280 fs	23	28
Nd:Glass (527 nm)	He	8 x 10^{14} 6 x 10^{14}	- -	600 fs	45 33	22*
KrF (248 nm)	Li^+ Na^+ K^+	10^{15}	6	0.5 ps	9 11 13	31
Nd:YAG (1064 nm)	Xe	5 x 10^{13}	20	36 ps	17	21
Nd:YAG (1064 nm)	Xe	5 x 10^{12}	-	36 ps	21	21*
Ti:Sapph. (790 nm)	He	-	-	65 fs	127	40
Ti:Sapph. (800 nm)	He	-	-	26 fs	221	13

Table 1.1: Summary of experimental parameters and results relating to HG experiments performed in references quoted. * denotes a simulated HG experiment.

is determined by the unfocused beam diameter and the focal length of the lens which focuses the beam into the generating cell. A large value of b describes a loosely-focused laser pulse since b is directly proportional to the cross-sectional area of the beam at focus. Short wavelength sources confer a larger confocal parameter than longer wavelength sources according to equation 1.3.

It is observed [29] that phase matching of higher order harmonics improves when the confocal parameter is much larger than the interaction length of the medium, i.e. the medium is contained within the focal volume. This result can be explained in terms of the coherence lengths of the output harmonics. The coherence length of a harmonic of order, q is related to the confocal parameter by equation 1.8:

$$L_{coh} = \frac{b}{2}\tan[\pi/(q-1)] \tag{1.8}$$

Hence, for increasing harmonic orders, q, L_{coh} decreases. Therefore, if the coherence length of a harmonic is less than the path length through the medium in which it is propagating, then dispersion effects in the medium will dephase the generated beam with a consequent drop in intensity.

Phase matching

Phase matching is the term applied to the phase shifts of all harmonics propagating through the medium [22,38]. Ideally, all harmonics should be generated in phase with each other in order to preserve coherence and eliminate destructive interference. However, phase matching all harmonics is difficult, especially for higher order harmonic orders. A phase mismatch is introduced by dispersion in the medium and at the focus in the medium. Tight focusing produces a phase slip of $q \times \pi$ radians for harmonics q in a Gouy phase shift.

Phase matching is improved with increasing laser intensity. However, in order to develop high intensities, one can only either increase the laser pulse energy used, decrease the pulse duration or increase the degree of focusing in the medium. Since the first two of these criteria are dependent on the operating capacities of the laser system then only the third alternative is viable, at the expense of decreased confocal parameter and phase matching.

Ionization effects

One of the greatest contributions to reducing harmonic generation efficiency arises from ionization of the medium by the intense laser field [31,38]. The limiting effect of ionization is twofold. Firstly, free electrons cannot contribute to HG since the HG process involves deexcitation of electrons to the ground state from which they were promoted. Secondly, free electrons contribute to dephasing of generated harmonics and hence reduce conversion efficiency.

Observations which can be attributed to ionized media are blue-shifts of laser and harmonic wavelengths. Ionization decreases the refractive index of the medium which blue-shifts the laser spectrum. A harmonic blue-shift follows from this. Also, when high sensitivity of HG efficiency to the intensity of the applied laser is observed, then ionization effects are predicted to be occuring. Ionization rates increase as the 5th power of intensity and drastic reductions in the extent of harmonic generation have been observed for small increases in laser intensity (Krause *et al.* report 90% ionization for a 50% increase in intensity [38]).

These limitations can be overcome using a number of experimental features. The deleterious effect of free electrons on phase matching is greater at longer incident wavelengths than at shorter wavelengths. The use of shorter wavelength ultraviolet lasers (e.g. KrF and XeCl excimers) has an advantage for XUV generation, since these wavelengths are produced at lower orders than long wavelength sources. However, these lasers promote MPI in rare gases. The most efficient method of reducing the extent of ionization is to use ultra-short pulse lengths ($< 10^2$ fs), which allow the HG process to occur on a timescale shorter than MPI.

Alkali ions are isoelectronic with rare gases but have much higher ionization potentials. Therefore, it is expected that a lower proportion of MPI is observed and that the extent of the harmonics will be somewhat greater (according to equation 1.7). However, the higher ionization potential implies a lower nonlinear response of these species and so will require higher intensities and high gas densities.

The inert gases exhibit characteristic harmonic spectra owing to the increase in polarizability and decrease in ionization potential down the group. The result of these properties are shown on figure 1.13. Xenon has a high polarizability and displays a high yield for low harmonics. The low ionization potential of and saturation intensity of xenon increases the efficiency of MPI at high harmonics with a consequent rapid decrease of harmonic yield at higher energies. Helium, in contrast, displays the exact converse of this behaviour: a low yield over all harmonics extending over a broad plateau to a maximum photon energy.

Experimental conditions

Variable factors in the design of a harmonic generation experiment influence the efficiency and include pressure dependence of the medium [34], polarization dependence [41,42] and method of detection.

The pressure dependence relationship is similar to that discussed for four-wave mixing, where low density promotes MPI and high density results in dispersion effects. In high-order harmonic generation, increasing pressure favours low orders of harmonics but decreases the output of high order harmonics. This is principally due to dispersion effects in the medium producing a phase mismatch over high harmonic orders.

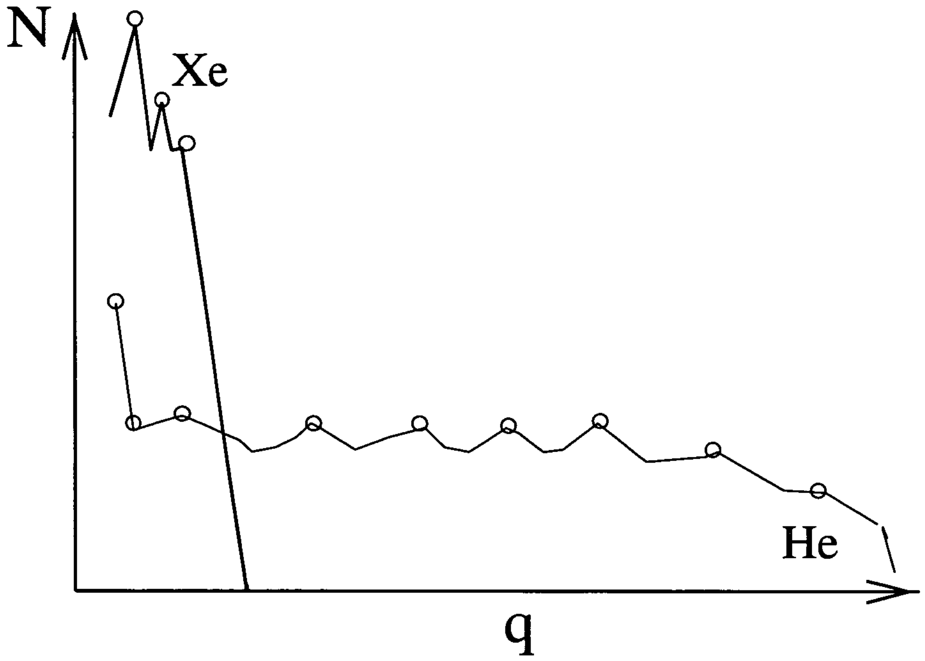

Figure 1.13: Harmonic intensity distribution curves for Xe and He

At the detection stage, a grating is most often used as the tuning element to separate the fundamental and harmonic wavelengths and direct the output through a slit to the detector. The grating surface is often coated with gold or platinum which has a high radiation damage threshold and reflectivity to VUV and XUV wavlengths. The resolution of detected harmonics is limited by the slit widths of the monochromator.

1.3.6 Applications of high harmonics as a coherent XUV source

With the improvements in conversion efficiencies gained from characterising XUV output from high harmonic generation, the technique has recently been utilised to provide a source of coherent, high brightness XUV radiation for application to spectroscopic experiments, such as photoionization. An excellent review is provided in ref. [43], detailing experiments by Balcou *et al.* [44] on measurement of photoionization cross sections in rare gases and on lifetime measurement of the $1s3p^1$ Rydberg state in He, by a pump-probe experiment [45] using excitation by the 13th harmonic of an 80 ps Ti:Sapphire laser. Applications in molecular spectroscopy have also been reported by Erman *et al.* on the measurement of the autoionization widths of high Rydberg states in NO [46]. It is now becoming apparent that the generation and use of high harmonics provides a valuable and practical complement to synchrotron radiation as a source of VUV to soft X-ray radiation.

1.4 Electronic Structure of the Halogens and Interhalogens

Important to the work presented in this thesis is the application of VUV radiation, generated by four-wave mixing, as a light source for one-photon spectroscopy of the halogen and interhalogen molecules studied (I_2 and ICl). This section first outlines the electronic structure of these molecules before discussing the spectroscopic processes occuring at energies corresponding to VUV frequencies. Two-photon excitation was also employed as a complementary experiment on Br_2 and is discussed here also.

All of the diatomic halogen and interhalogen molecules have been studied spectroscopically, to varying extents, in the VUV region of the spectrum by a variety of experimental techniques including one-, two- and more photon excitation. The two classes of molecule differ principally in their symmetry classification and are distinguished as homonuclear and heteronuclear diatomics. The homonuclear diatomics display common characteristics in their spectra, a consequence of sharing similar electronic structures throughout the group. However, differences in the electronic structure arise throughout the group, which can be correlated with the structure of the component atoms, such as the effect of spin-orbit coupling and can be helpful for predicting electronic processes within the molecule. The heteronuclear diatomics possess a lower symmetry and consequently display somewhat more congested spectra. However, it is found that many of the same arguments can be applied in the interpretation of the spectra of these molecules as with their homonuclear analogues.

The VUV regions of these molecules (i.e. at excitation energies in the range

50 000-100 000 cm^{-1}) are rich in high-lying excited states, including ion-pair and Rydberg states, both of which have been observed spectroscopically. The following sections introduce and discuss the characteristics and properties of these states from a theoretical viewpoint.

1.4.1 The Rydberg states

Electronic states formed in either atomic or molecular species by promotion of an electron from an orbital in the ground state to an orbital with a higher principal quantum number, n, are termed Rydberg states. For a given electron with orbital angular momentum, l, successive values of n form a Rydberg series converging on a particular atomic or molecular ion core, as n tends to infinity. The Rydberg series may therefore be denoted $[J]nl$ or $[\Omega]nl$ for atoms and molecules respectively. The core state may be classified by the term or total angular momentum of the ionic state to which the Rydberg series converges.

The energies of Rydberg states within a series can be determined mathematically using the Rydberg equation (1.9)

$$E([core^{+}]nl) = IE[core^{+}] - \frac{109737.1}{[n - \delta(l)]^2} \tag{1.9}$$

where $\delta(l)$ is roughly constant for the particular orbital which the Rydberg electron occupies and is known as the quantum defect. The significance of this term lies in the interaction of the wavefunction of the Rydberg electron with the core region. The Rydberg electron, although occupying an orbit at a large distance from the core does not experience a point charge, similar to a hydrogenic atom model. Instead, the presence of core electrons shields the Rydberg electron from the nucleus. The magnitude of this shielding effect depends on the angular momentum, l, of the electron because the nl radial wavefunctions penetrate into the core region to varying extents. Hence, δ is a function of l and decreases in the order s>p>d>f, with electrons in s orbitals most penetrating.

For any given l on a particular core, a range of components are available based on the microconfiguration of the core state and the Rydberg electron which is coupled to it. These components are distinguished as having either a purely triplet or significant singlet character and take a range of overall angular momentum values, each of which characteristics determines the relative energy ordering of each component. In molecules containing heavier atoms, including iodine and bromine, only a weak electric field is present along the internuclear axis [47]. Hence, the interaction between L and S on a particular atom centre may be stronger than the interaction of either of these angular momenta with the internuclear axis. Hence, the projections of L and S on the axis; Λ and Σ are not defined. This form of coupling is analogous to that in an atom where no Paschen-Back effect occurs, which is a consequence of L and S angular momenta being uncoupled by a strong external electric field, leading to space quantization, with respect to the direction of the field, into two independent components $m_L(h/2\pi)$ and $m_S(h/2\pi)$. Instead, in the molecular system, L and S on the atom centre combine to form a resultant J or total angular momentum which couples to the internuclear axis with projection Ω, which is defined for electronic states of the molecule and hence is a "good" quantum number. This type of coupling is Hund's case (c) coupling scheme and all electronic states in the halogens and interhalogens discussed in this thesis are represented by this coupling scheme.

In Br_2, ICl and I_2 the spin-orbit coupling is strong at each atom centre indicating that Hund's case (c) is the most appropriate coupling scheme. The coupling of the Rydberg electron to the core is by jj-coupling. Here, an overall angular momentum, Ω, is defined as the sum or difference of the total angular momenta of the core Ω_c and the Rydberg electron, ω_{Ryd} represented by equation 1.10. It is entirely valid to represent the Rydberg state component as $[\Omega_c]nl\lambda;\ \Omega$ since, owing to weak coupling between the Rydberg electron and the core through electron exchange, Ω_c, ω_{Ryd} and l_{Ryd} are each good quantum numbers. The properties of spin can also be included in the overall assignment of the Rydberg state. In the halogen and interhalogen diatomic molecules, the lowest Rydberg states are associated with an ionic core in a doublet spin state ($^2\Pi$), resulting in a singlet and a triplet Rydberg series.

$$\Omega = \Omega_c \pm \omega_{Ryd} \tag{1.10}$$

The Rydberg states of the halogen/interhalogen molecules are generally found to hold similar characteristics to atomic Rydberg states. For I_2 and ICl, the quantum defects for each l are similar to those found in atomic iodine. Similarly, for Br_2 the molecular quantum defects are based on those in the single atom.

1.4.2 The ion-pair states

The ion-pair states of the halogens form a sub-set of the valence states of the molecules and, while all molecules have ion-pair states, which in some may constitute the ground state of the molecule (e.g. alkali group metal compounds), they are found to be excited states in the halogens, formed by electron promotions within the valence shell. Ion-pair states are, by definition, states which may diabatically dissociate into a pair of oppositely charged ions (A^++B^-) rather than neutral fragments. However, crossings at large R of the asymptotic branches of these states with Rydberg or valence states can result in adiabatic dissociation into neutral products correlating with the crossed state, provided the two states involved are of the same symmetry. Bound levels of the ion-pair states are represented by a pair of ions bonded by Coulombic attraction (e^2/R).

Such ion-pair states share a number of characteristics which have largely been determined by spectroscopic investigation [48]. As a first step, the potential, $V(R)$, of an ion-pair state is given by the Rittner (or Born-Mayer) potential (equation

1.11):

$$V(R) = Ae^{-\alpha R} - e^2/4\pi\epsilon_0 R + E_i(A,B) - E_{ea}(B,A) \tag{1.11}$$

where $V(R)$ is measured relative to the neutral, ground state dissociation potential. E_i and E_{ea} are the ionization potential and electron affinity of the ionic fragments. The dissociation energy of the ion-pair state, relative to v'=0 of the ground state, or ion-pair threshold is derived from the sum of E_i, E_{ea} and D_0(A-B). The Rittner potential (1.11) can be further refined by including long-range charge/quadrupole terms ($\propto R^{-3}$), polarization (for atomic ions) ($\propto R^{-4}$) and dispersion terms ($\propto R^{-6}$).

Term values can be derived from a combination of equation (1.11) and the expression for the dissociation energy of the ion-pair state, given by (1.12)

$$D_e \approx -e^2/4\pi\epsilon_0(r_{A^-} + r_{B^+}) \tag{1.12}$$

to give the term value at equilibrium distance (1.13)

$$T_e \approx D_e(X) - e^2/4\pi\epsilon_0(r_{A^-} + r_{B^+}) + E_i(A,B) - E_{ea}(B,A) \tag{1.13}$$

These equations (1.11-1.13) provide a model of a typical individual ion-pair state and the position of the state in $R-E$ space. Typical T_e values for the lowest lying ion-pair states are in the range 30 000-40 000 cm^{-1}, R_e values are around

3 Å and D_e may be up to 30 000 cm^{-1}, representing a deeply bound potential. Consequently, such a potential supports many vibrational levels and, owing to the wide amplitude of vibration created by the large internuclear separation and shallow potential, the energy spacing between vibrational levels is relatively low (of the order 100 cm^{-1} in I_2).

The electronic structure of the valence states of the halogens with configuration given by $[ijkl]$ which denotes the orbital occupancy of the valence shell, gives rise to 20 ion-pair states for both the halogens and interhalogens. These states correlate with dissociation products X^++X^- (or X^++Y^-/ X^-+Y^+ for the interhalogens). Terms arising from the product ions, determined by the configuration of the positive ion fragment (the negative ion is always $^1S_0$), indicate the tier to which an ion-pair state belongs. In the case of I_2, four tiers of ion-pair states exist, with each tier comprising closely spaced clusters of states, each of which correlates with a dissociation product determined by the configuration of the I^+ ion. The energy spacing of these tiers is close to that between the term values of the $^3P_2$, $^3P_{1,0}$, $^1D_2$ and $^1S_0$ atomic ion states, in order of increasing energy.

In ICl, the lowest ion-pair states are those correlating with dissociation products I^++Cl^-. With the loss of g/u symmetry only half the number of states occupy each tier, although the ordering is still determined by the term values of the I^+ ion states. Therefore, ten ion-pair states correlate with I^++Cl^- and ten with I^-+Cl^+ at higher energy.

1.4.3 Rydberg/ion-pair state interactions: predissociation

Several studies have been made on the interaction of bound levels of ion-pair states with Rydberg states in the same energy region [49–51]. In the case of the halogens and interhalogens these represent the lowest tier ion-pair states and some of the lower members of the relevant Rydberg series. These interactions have been probed using one- or two-photon excitation and a great deal of information can be inferred depending on the experimental methodology employed. This is highlighted in the next section, however such interactions are discussed from a theoretical viewpoint here.

Essential to the results obtained from experimental work presented in this thesis is the process of ion-pair formation in I_2 and ICl. This represents a form of Rydberg/ion-pair interaction where bound levels of a Rydberg state, through interaction with an ion-pair state at energies above the dissociation limit of the ion-pair state, are converted into unbound ion-pair fragments by predisscociation and subsequently experimentally observed by mass-analysis of ionic products. It has been shown that the various selection and propensity rules associated with bound-bound interactions between Rydberg/ion-pair states apply to the predissociation mechanism introduced above.

Hund's case (c) coupling scheme is appropriate for the ion-pair states of the halogens and interhalogens discussed here. If two Hund's case (c) states with the same total angular momentum, Ω, cross each other or overlap at an internuclear separation, R, then a homogeneous interaction takes place resulting in an avoided crossing at R. Ion-pair states in the halogens cross Rydberg states near their equilibrium bond distances with their repulsive or inner limbs, hence a number of avoided crossings have been deduced experimentally as perturbations in the vibrational ordering of the ion-pair state or even loss of intensity through intensity borrowing by the Rydberg state. However, this case applies only to the bound levels of the ion-pair states crossing lower members of the Rydberg series. Above the ion-pair threshold, the positions of the inner limbs of the Rydberg and ion-pair potentials in $R-E$ space are computed to lie in close proximity, such that the Rydberg state appears to be nested within the ion-pair continuum. These potentials, on the inner limbs, are at sufficiently small internuclear separation that it becomes appropriate to consider each state with a single molecular orbital (MO) configuration, identified by the orbital occupancy of the valence shell $[ijkl]$ in $(\sigma)^i(\pi)^j(\pi)^k(\sigma)^l$. This is important in the treatment of the predissociation mechanism where a number of factors determine the extent of the interaction. The close proximity of the potentials ensures an appreciable vibrational overlap between wavefunctions on the (bound) Rydberg state vibronic level and the ion-pair wavefunction. Homogeneous interactions (predissociation) are assumed to be the most efficient mechanism involved such that $\Delta\Omega$=0 or Ω_{Ryd}= $\Omega_{i.p.}$ and g↔g/u↔u (homonuclear halogens only), +↔+ selection rules apply. The various factors which determine the extent or strength of the predissociation mechanism are discussed fully for I_2 and ICl in the relevant chapters in the thesis. Briefly, however, the strongest interactions are those between states with the same spin multiplicity and which differ in orbital occupancy by one or two electrons. The configurations of the Rydberg and ion-pair states are connected by a two-electron exchange which is most favourable if conversion is by parallel electron transitions (i.e. $\sigma \rightarrow \sigma$ or $\pi \rightarrow \pi$).

1.5 Experimental Methodology

The interpretation of results obtained in this thesis is derived from the raw data obtained from the experimental procedures at our disposal. This data is, in turn, subjected to various treatments to allow us to test the results against known theories and to compare with other results from similar experimental procedures. With advanced features available in the apparatus used, the interpretation can be refined further relative to previous related experiments.

Two laser-based experimental techniques were used in this work to observe the Rydberg states of the halogen containing molecules Br_2, I_2 and ICl. Rydberg states were principally accessed using either one-photon excitation (I_2 and ICl) or two-photon excitation (Br_2). This section introduces and discusses how the experimental techniques used are related to the theoretical interpretation of the results.

1.5.1 One-photon spectroscopy

According to the Born-Oppenheimer approximation, electronic transitions occur effectively instantaneously relative to the motion of the nuclei within a molecule. Hence, in the case of diatomic molecules transitions will only arise within certain geometries of the nuclear framework, defined by the internuclear separation of the initial state. This forms the basis of the Franck-Condon Principle whereby in vibronic transitions between an initial and final state, the nuclei do not change position or velocity appreciably and so only excited states which are encountered within a region of $R-E$ space bounded by the vibrational amplitude of the initial state (known as the Franck-Condon region) are accessible. Intensities of transitions are derived from the Franck-Condon factor; a product of the vibrational wavefunctions of the initial and final states integrated over some molecule-fixed coordinate. The vertical dashed lines in figure 1.14 show the Franck-Condon region schematically for the iodine molecule and some of the vibronic states within this region.

A molecule excited in a resonant transition from its electronic ground state by a single photon, will access, primarily, an excited state configuration with an orbital occupancy differing by one electron relative to the ground state configuration. A resonant state will only be accessed provided the transition is allowed by selection rules. The most rigorously applied selection rule is the electric dipole transition selection rule. Essentially, for a transition to possess a nonzero electronic transition moment, R_e, the product of the symmetry species of the upper and lower electronic state wavefunctions ($\psi_e^{'}$ and $\psi_e^{''}$, respectively) and the transition dipole moment, μ, must be totally symmetric. For example, for molecules with point group $D_{\infty h}$ (e.g. I_2) equation (1.14) applies.

$$\Gamma(\psi_e^{'}) \times \Gamma(\mu) \times \Gamma(\psi_e^{''}) = \Sigma_g^+ \tag{1.14}$$

The ground electronic state in the diatomic halogens is always a closed shell and therefore has a totally symmetric wavefunction (equation 1.15).

$$\Gamma(\psi_e^{''}) = \Sigma_g^+ \tag{1.15}$$

Hence, the symmetry species of the upper electronic state, $\Gamma(\psi_e^{'})$, and the transition dipole moment, $\Gamma(\mu)$, must be equivalent. Furthermore, an allowed electronic transition is identified from the character table by a symmetry operation corresponding to a translation. If the symmetry of the upper electronic state can be represented by a translation such that $\Gamma(\psi_e^{'})$=$\Gamma(T_x)$ and/or $\Gamma(T_y)$ and/or $\Gamma(T_z)$, then the corresponding state is accessible by one-photon selection

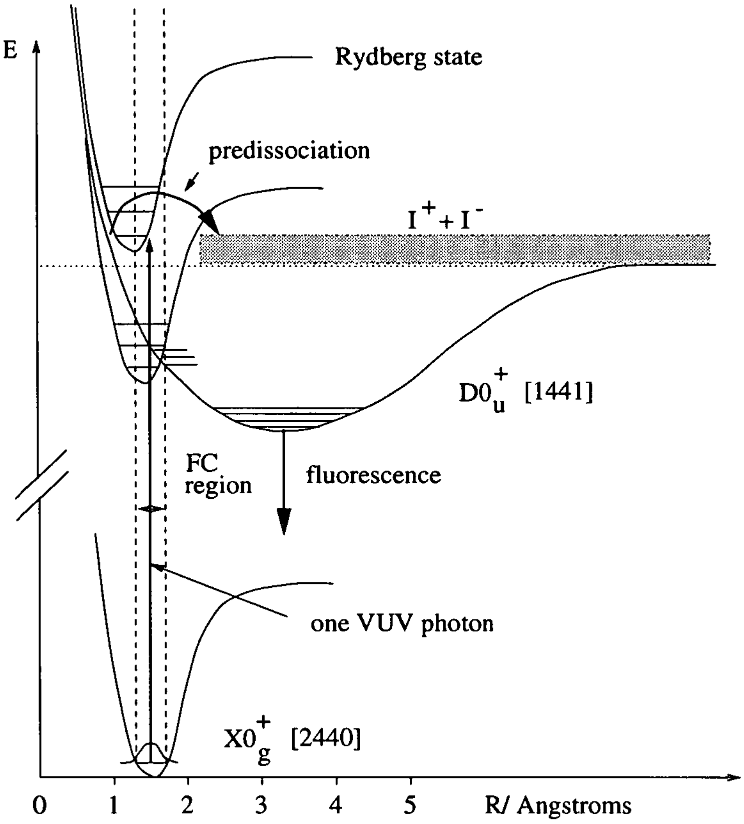

Figure 1.14: Schematic of potential energy curves and radiative and non-radiative processes occuring in I_2 on excitation by one VUV photon.

rule. For example, from the $D_{\infty h}$ character table, finding the symmetry species equivalent to translation symmetry operations gives $\Gamma(T_x, T_y) \equiv \Pi_u$ and $\Gamma(T_z) \equiv \Sigma_u^+$. Therefore, the allowed transitions in I_2 are $\Sigma_g^+ \rightarrow \Sigma_u^+, \Pi_u$.

This result produces a consequence of the Laporte selection rule which states that "the only allowed electric dipole transitions are those involving a change of parity", which applies to the homonuclear case described above whereby electronic states may be symmetric with respect to inversion through the centre of symmetry (called *gerade* or g states) or antisymmetric (*ungerade* or u states). Hence the selection rule (1.16) applies.

$$g \leftrightarrow u \tag{1.16}$$

Of course, the electronic states in the "heavier" diatomic molecules discussed here are classified by the overall angular momentum quantum number, Ω, according to Hund's case (c) coupling scheme. Nevertheless, states described by Hund's case (a) which adopt terms given by the symmetry species in the appropriate character table can be correlated with Hund's case (c) states, the difference being that the spin multiplicity, a 'good' quantum number in Hund's case (a), is not rigorously applied in transitions between Hund's case (c) states. This gives rise to two further selection rules (1.17) and (1.18) in one-photon transitions.

$$\Delta\Omega = 0, 1 \tag{1.17}$$

$$\Delta S = 0 \tag{1.18}$$

By applying the selection rules (1.16)-(1.18) (in the homonuclear case, (1.17), (1.18) in the heteronuclear case), the expected observable states can be deduced. One final important consideration must be made for the Rydberg states of I_2. The lowest energy ionic core has an overall *gerade* parity since it is formed by promotion of an electron from a π_g antibonding orbital. The Rydberg electron coupled to the ionic core must necessarily have an *ungerade* parity to be observed in a one-photon transition. This is determined by the symmetry of the atomic-like orbital occupied by the Rydberg electron. Hence, in the case of iodine, only np and nf Rydberg states are observed. For ICl, with the loss in g/u symmetry this selection rule breaks down and the Rydberg electron may occupy ns, np, nd and nf orbitals. This is discussed further in the relevant experimental chapters on both molecules.

To summarise the overall observations which can be made by employing one-photon spectroscopy to a diatomic molecule, the schematic diagram on figure 1.14 shows some of the radiative and non-radiative processes occuring within I_2. Using a tunable source of radiation with vacuum-UV wavelengths, a number of vibronic states within the Franck-Condon region of the molecule can be accessed including ion-pair and Rydberg states. The $D0_u^+$ ion-pair state has been deduced to have a configuration [1441] since this differs from the ground state configuration [2440] by an orbital occupancy of one electron. The transition is strong since it involves a parallel transition ($\sigma \rightarrow \sigma^*$). The D state correlates with a $^1\Sigma_u^+$ state in Hund's case (a) notation and so is allowed according to the selection rules detailed above. This state has been observed as a long vibrational progression in absorption and fluorescence. The presence of Rydberg states has been deduced due to intensity borrowing from this ion-pair state, manifested as dips in the fluorescence spectrum, a consequence of Rydberg/ion-pair state interaction. The nature and mechanism of predissociation of Rydberg states observed above the first ion-pair threshold in absorption will be discussed fully in the chapters on ion-pair formation from I_2 and ICl.

1.5.2 Two-photon spectroscopy

The observation of excited states lying at energies in the VUV wavenumber range has been approached in a number of ways. Until around the mid-1970's, with the development of lasers, electronic spectroscopy was limited to using conventional light sources such as continuum or line sources, depending on the application. Spectroscopy in the VUV range was especially difficult because of oxygen absorption, requiring the VUV source and beam path to be contained within an evacuated environment; a method which is both operationally demanding and expensive. The introduction of synchrotron radiation sources overcame some of these problems and added the benefit of higher brightness in the VUV range, however high resolution work is precluded by use of these sources where $\Delta\nu$ is typically *ca.* 50 cm^{-1}. Latterly, of course, the use of two conventional table-top tunable dye laser sources to generate a source of laser radiation with VUV wavelengths by four-wave mixing in a highly polarisable nonlinear medium, a technique employed in the work described in this thesis, has been developed and used in a number of applications. However, regardless of the experimental method employed, the electric dipole selection rules governing one-photon transitions impose a limit on the number of excited states accessible.

The exploitation of multiphoton transitions has made the observation of high-lying electronic states highly practicable by using conventional tunable dye lasers, operating with UV or visible wavelengths. Furthermore, a number of states inaccessible by one-photon transition can be observed by introducing alternative selection rules in the transition scheme.

A high photon density is required to overcome the very low cross sections for multiphoton processes ($\sigma \sim 10^{-51}$ cm^4s for two-photon processes to be considered here). This can be achieved through the use of pulsed dye lasers. A significant enhancement of the cross-section in a two-photon process is encountered when the total energy of two photons is equal to the transition energy of a resonant state. This process may occur *via* a virtual, continuum or real intermediate state at the one-photon level. A coherent multiphoton process, exciting a two-photon resonant state through a virtual intermediate, relies on the nonlinear polarizability of the molecule. Such a state exists for a very short time ($\sim 10^{-15}$ s) and so the second photon must be absorbed effectively simultaneously. Once the molecule is populated in the resonant excited state a further, third photon with sufficient energy may ionize the molecule. This process is known as [2+1] resonance enhanced multiphoton ionization (REMPI) which is a particular, widely used example of the general [m+n] REMPI process, where m is the number of photons used to reach the resonant state and n the number of photons required to ionize the molecule from this state. Several examples have been reported where $m > 2$, but the cross-sections of such higher-order processes decrease rapidly with m.

Figure 1.15 shows a schematic diagram of the [2+1] REMPI process, indicating the possible intermediate states involved at the one-photon level. Some intermediate states may influence the appearance of the two-photon spectrum as will be discussed in more detail in the chapter on the [2+1] REMPI spectrum of Br_2. In general, [2+1] REMPI experiments indicate that a vertical transition, with two-photons, accesses the resonant state. Other related experiments such as DRINCS [52–54] (double resonance ionization of nozzle-cooled species) employ two photons of different frequency *via* a real or continuum intermediate as a way of expanding the Franck-Condon region to observe states at larger interatomic distance, such as ion-pair states. Each method employs ion detection in the experimental arrangement which allows a high sensitivity and may be coupled with a time-of-flight mass spectrometer for the mass resolution of component ions produced in the process.

Considering the two-photon spectra of the homonuclear halogen diatomics, of which Br_2 has been studied here, the selection rules governing transitions within this molecule are given by equations (1.19)-(1.21).

$$g \rightarrow\rightarrow g \tag{1.19}$$

$$\Delta\Omega = 0, 1, 2 \tag{1.20}$$

$$\Delta S = 0 \tag{1.21}$$

Hence, only *gerade* states with Ω=0, 1 or 2 are accessed at the two-photon level. It will be shown in subsequent chapters that states with an appreciable singlet character are mostly observed according to propensity rule. Rydberg states have been shown to dominate the [2+1] REMPI spectra of the homonuclear halogens, which according to selection rule (1.19) are necessarily ns or nd states coupled to the lowest *gerade* ionic core ($[3/2]_g$ and $[1/2]_g$). The $E0^+$ ion-pair state in IBr [55] and ICl [56] has been observed to dominate the [2+1] REMPI spectrum. This represents an allowed transition in the heteronuclear halogens but the analogous

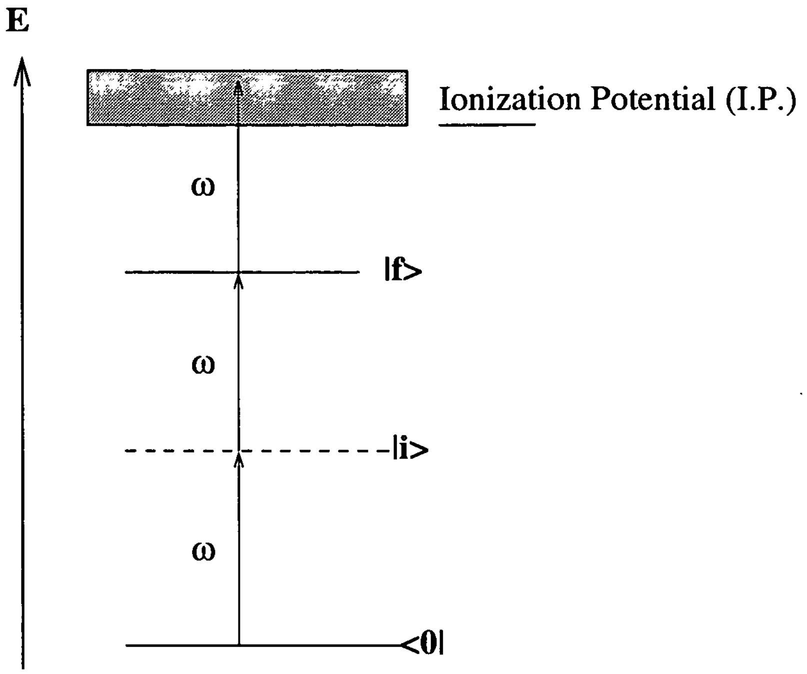

Figure 1.15: Schematic diagram of [2+1] REMPI process using one colour, ω. The intermediate state, |i>, may be a virtual, real or continuum state. Enhancement of the ion signal comes from third ionizing transition from the bound, resonant state |f>.

state $D0_u^+$ is forbidden in the homonuclear case.

The presence of ion-pair states may be inferred from the rotational contours of Rydberg state bands which may show evidence of Rydberg/ion-pair interactions. The experimental technique of polarization spectroscopy is also available in [2+1] REMPI experiments whereby the appearance of the spectrum is altered, often drastically, by the use of circularly polarized light. Here, the linestrengths of two-photon transitions, which have been theoretically determined in terms of the Ω value of the state and the dipole moment of the transition, can be used to identify and assign states (see chapter 3). Such a technique is experimentally more difficult in one-photon VUV spectroscopy since an optical device is required in the throughput of the beam, conventionally constructed from quartz, a more suitable VUV transparent material (such as MgF_2 or LiF) would be required in the construction.

1.6 References

[1] W. Jamroz and B.P. Stoicheff, *Progress in Optics*, **20**, 325 (1983)

[2] S.E. Van Bramer and M.V. Johnston, *Appl. Spec.*, **46**, 255 (1992)

[3] M.N.R. Ashfold and J.D. Prince, *Mol. Phys.*, **73**, 297 (1991)

[4] J.P. Marangos, N. Shen, H. Ma, M.H.R. Hutchinson and J.P. Connerade, *J. Opt. Soc. Am. B*, **7**, 1254 (1990)

[5] R. Hilbig and R. Wallenstein, *IEEE J. Quant. Elect.* **QE-19** (1983) 194

[6] C.E.M. Strauss and D.J. Funk, *Opt. Lett.* **16** (1991) 1192

[7] G. De Cesare, F. Irrera, F. Palma, G. Naletto, P. Nicolosi and E. Jannitti, *Appl. Opt.* **36** (1997) 2751

[8] K. Yamanouchi, *J. Elect. Spec. & Rel. Phenom.* **80** (1996) 267

[9] A.H. Kung and Y.T. Lee, *Recent Progress in the Study of Vacuum Ultraviolet Ionization and Dissociation of Molecules and Clusters*, ed. C.Y. Ng, World Scientific, Singapore (1991)

[10] K. Miyazaki, *J. Nonlinear Opt. Phys. & Mat.* **4** (1995) 567

[11] C.-G. Wahlstrom, *Physica Scripta* **49** (1994) 201

[12] S.L. Chin, Y. Liang, S. Augst, P.A. Golovinski, Y. Beaudoin and M. Chaker, *J. Nonlinear Opt. Phys. & Mat.* **4** (1995) 667

[13] Z.H. Chang, A. Rundquist, H.W. Wang, M.M. Murnane, H.C. Kapteyn, *Phys. Rev. Lett.* **79** (1997) 2967

[14] G. Mourou and D. Umstadter, *Phys. Fluids B* **4** (1992) 2315

[15] P.F. Moulton, *J. Opt. Soc. Am. B* **3** (1986) 125

[16] K. Yamakawa, P.H. Chiu, A. Magana and J.D. Kmetec, *IEEE J. Quant. Elect.* **30** (1994) 2698

[17] Annual Meeting of the Optical Society of America 1986, *Symposium on Advances in Ultrashort Pulses*, p97

[18] P. Maine, D. Strickland, P. Bado, M. Pessot and G. Mourou, *IEEE J. Quant. Elect.* **24** (1988) 398

[19] Y.-H. Chuang, L. Zheng and D.D. Meyerhofer, *IEEE J. Quant. Elect.* **29** (1993) 270

[20] T. Zhang, L.S. Bhushan and H. Daido, *Elect. Lett.* **31** (1995) 1684

[21] P. Balcou and A. L'Huillier, *Phys. Rev. A* **47** (1993) 1447

[22] S.C. Rae, K. Burnett and J. Cooper, *Phys. Rev. A*, **50** (1994) 3438

[23] A. L'Huillier, M. Lewenstein, P. Salieres, P. Balcou, M.Y. Ivanov, J. Larsson and C. G. Wahlstrohm, *Phys. Rev. A* **48** (1993) R3433

[24] T. Ditmire, J.K. Crane, H. Nguyen, L.B. DaSilva and M.D. Perry, *Phys. Rev. A* **51** (1995) R902

[25] K. Miyazaki, H. Sakai, G. Kim and H. Takada, *Phys. Rev. A* **49** (1994) 548

[26] J. Peatross and D.D. Meyerhofer, *Rev. Sci. Instrum.* **64** (1993) 3066

[27] C.-G. Wahlstrom, J. Larsson, A. Persson, T. Starczewski, S. Svanberg, P. Salieres, P. Balcou, A. L'Huillier, *Phys. Rev. A* **48** (1993) 4709

[28] K. Kondo, N. Sarukura, K. Sajiki and S. Watanabe, *Phys. Rev. A*, **47** (1993) 2480

[29] J.J. Macklin, J.D. Kmetec and C.L. Gordon III, *Phys. Rev. Lett.*, **70** (1993) 766

[30] A. L'Huillier, P. Balcou and L.A. Lompre, *Phys. Rev. Lett.*, **68** (1992) 166

[31] Y. Akiyama, K. Midorikawa, Y. Matsunawa, Y. Nagata, M. Obara, H. Tashiro and K. Toyoda, *Phys. Rev. Lett.* **69** (1992) 2176

[32] C. Lynga, A. L'Huillier, C.-G. Wahlstrom, *J. Phys. B: At. Mol. Opt. Phys.* **29** (1996) 3293

[33] D.J. Fraser, M.H.R. Hutchinson, J.P. Marangos, Y.L. Shao, J.W.G. Tisch and M Castillejo, *J. Phys. B: At. Mol. Opt. Phys.* **28** (1995) L739

[34] C. Altucci, T. Starzcewski, E. Mevel, C.-G. Wahlstrom, B. Carre and A. L'Huillier, *J. Opt. Soc. Am. B* **13** (1996) 148

[35] J. Peatross, M.V. Federov and K.C. Kulander, *J. Opt. Am. Soc. B* **12** (1995) 863

[36] J. Zhou, J. Peatross, M.M. Murnane, H.C. Kapteyn and I.P. Christov, *Phys. Rev. Lett.* **76** (1996) 752

[37] A. L'Huillier, P. Balcou, S. Candel, K.J. Schafer and K.C. Kulander, *Phys.*

Rev. A **46** (1992) 2778

[38] J.L. Krause, K.J. Schafer and K.C. Kulander, *Phys. Rev. Lett.*, **68** (1992) 3535

[39] M. Lewenstein, P. Balcou, M.Y. Ivanov, A. L'Huillier and P.B. Corkum, *Phys. Rev. A* **49** (1994) 2117

[40] K. Miyazaki, M. Kakehata and H. Takada, *IOP Conf. Ser.*, **154** (1997) 168

[41] F.A. Weihe and P.H. Bucksbaum, *J. Opt. Soc. Am. B* **13** (1996) 157

[42] F.A. Weihe, S.K. Dutta, G. Korn, D. Du, P.H. Bucksbaum and P.L. Shkolnikov, *Phys. rev. A* **51** (1995) R3433

[43] P. Balcou, P. Salieres, K.S. Budil, T. Ditmire, M.D. Perry and A. L'Huillier, *Z. Phys. D* **34** (1995) 107

[44] A. L'Huillier, T. Auguste, P. Balcou, B. Carre, P. Monot, P. Salieres, C. Altucci, M.B. Gaarde, J. Larsson, E. Mevel, T. Starczewski, S. Svanberg, C.-G. Wahlstrom, R. Zerne, K.S. Budil, T. Ditmire and M.D. Perry, *J. Nonlinear Opt. Phys. & Mat.* **4** (1995) 647

[45] J. Larsson, E. Mevel, R. Zerne, A. L'Huillier, C.-G. Wahlstrom and S. Svanberg, *J. Phys. B: At. Mol. Opt. Phys.* **28** (1995) L53

[46] P. Erman, A. Karawajczyk, E. Rachlew-Kallne, E. Mevel, R. Zerne, A. L'Huillier and C.-G. Wahlstrom, *Chem. Phys. Lett.* **239** (1995) 6

[47] G. Herzberg, *Molecular Spectra and Molecular Structure- Spectra of Diatomic Molecules*, Vol.1, Van Nostrand Reinhold Company (1989)

[48] K.P. Lawley and R.J. Donovan, *J. Chem. Soc. Farad. Trans.* **89** (1993)

1885

[49] A.R. Hoy, S.M. Jaywant and J.C.D. Brand, *Mol. Phys.* **60** (1987) 749

[50] K.P. Lawley, T. Ridley, Z. Min, P.J. Wilson, M.S.N. Al-Kahali and R.J. Donovan, *Chem. Phys.* **197** (1995) 37

[51] K.P. Lawley, E.A. Kerr, R.J. Donovan, A. Hopkirk, D. Shaw and A.J. Yencha, *J. Phys. Chem.* **94** (1990) 6201

[52] R.J. Donovan, T. Ridley, K.P. Lawley and P.J. Wilson, *Chem. Phys. Lett.* **196** (1992) 173

[53] R.J. Donovan, K.P. Lawley, Z. Min, T. Ridley and A.J. Yarwood, *Chem. Phys. Lett.* **226** (1994) 525

[54] P.J. Wilson, T. Ridley, K.P. Lawley and R.J. Donovan, *Chem. Phys.* **182** (1994) 325

[55] A.J. Yencha, T. Ridley, R. Maier, R.J. Donovan and A. Hopkirk, *J. Phys. Chem.* **97** (1993) 4582

[56] R.J. Donovan, J. Goode, K.P. Lawley, T. Ridley and A.J. Yencha, *J. Phys. Chem.* **98** (1994) 2236

Chapter 2

Experimental Methods

2.1 Vacuum Ultraviolet and Two-Photon Studies

Experimental work performed in Edinburgh, has included extensive work on the high-lying excited states of the halogen and interhalogen molecules. The ability to perform two-colour experiments has expanded the accessible regions of *R-E* space *via* pump-probe excitation through expansion of the Franck-Condon window. This formed the principle behind double-resonance ionization of nozzle cooled species (DRINCS)[1,2] which allowed the vibrational manifolds of ion-pair states, lying at large internuclear separation, to be observed.

Furthermore, resonance-enhanced multiphoton ionization (REMPI) experiments in which vertical excitation using two or more photons to access resonances in the Rydberg series of states, followed by ionization by one or more photons, have also been extensively carried out [3–5]. Hence, a great deal is known about two or more photon transitions in several molecules, from utilisation of the power and flexibility of the laser system available.

The work described in this thesis includes the development and use of the present laser system to generate VUV wavelengths in order to probe the Rydberg and ion-pair states of the same molecules at the one-photon level.

2.1.1 The Lambda Physik laser system

An excimer pumped dye laser system was used for the [2+1] REMPI and four-wave mixing experiments performed in Edinburgh. Up to two dye lasers could be pumped from the XeCl excimer pulsed source, with the output from each independently tunable. Pulse lengths of the dye laser output were given as 15 ns, with a linewidth <0.2 cm^{-1} and typical average power from the fundamental of the dye of the order 10 mW, depending on the dye solution used. A description of the operation of each laser is given in the next two sections.

Excimer laser EMG 201MSC

The XeCl (xenon chloride) excimer laser operates on transitions between an electronic state of the excited dimer molecule, XeCl* (properly termed an *exciplex*, or excited state complex, but commonly referred to as an excimer), and the repulsive state occupied by xenon and chlorine atoms in their ground states [6]. The relevant states are shown on figure 2.1. The pumping transition is provided by a high voltage electric discharge, typically around 21 kV, applied transversely across the cavity, which creates a high proportion of bound, excited XeCl molecules. Since this species is only weakly bound in its electronic ground state and dissociates rapidly (a lifetime of the order of a few picoseconds), a population inversion is automatically maintained in the upper bound state. The EMG 201MSC excimer laser contains a mixture of Xe, HCl and He gases. On discharging, excited Xe atoms are formed and HCl molecules may dissociate to form excited Cl atoms. Excimer formation is promoted *via* reaction between excited Xe atoms and Cl atoms or HCl molecules, moderated by a large concentration of He gas which acts as a buffer. A radiative decay process follows with a wavelength of 308 nm, determined by the transition energy between two states (see figure 2.1) and hence, a two-level lasing action is produced.

The excimer laser used in this work produced output pulses of around 500 mJ, with a pulse length of 15 ns, at a repetition rate of typically 5-10 Hz.

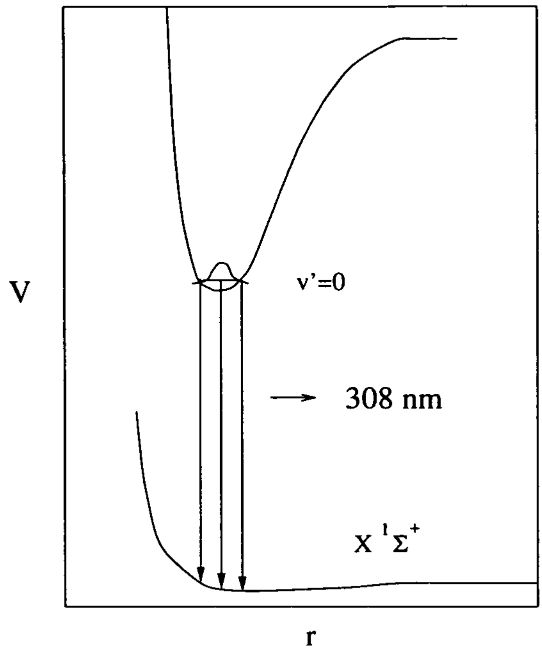

Figure 2.1: Potential curves for a very weakly bound ground state and strongly bound excited state of XeCl, highlighting the electronic states involved in a gas-discharge XeCl excimer laser.

Dye lasers FL2002, FL3002E

Radiation of wavelength 308 nm (UV) can access strong absorption regions of certain dye molecules. Figure 2.2 shows the four-level lasing action in a dye laser medium, in terms of the radiative and nonradiative processes involved [6]. An initial pump transition, provided by the excimer laser source (λ=308 nm), excites the dye molecule into the first excited singlet state, S_1. This is followed by a very fast nonradiative decay, *via* collisional deexcitation by solvent molecules, on a timescale of the order 10 ps to lower vibrational levels within the excited state manifold of the dye molecule. Fluorescence then occurs over a wide range of wavelengths on a timescale of around 10 ns. A large fluorescence quantum yield ($\Phi_f \rightarrow 1$) is a characteristic property of laser dyes and hence an intense emission can be obtained given a suitably bright pumping source. Fluorescent transitions terminate in upper vibrational levels of the ground state, S_0. These excited vibrational states are depleted rapidly *via* collisional deexcitation, again on a timescale of around 10 ps, thus maintaining a population inversion between upper electronic state, low vibrational levels and ground electronic state, high vibrational levels.

Tunability is possible in dye lasers owing to the high density of vibrational and rotational states in S_0 and S_1 of the dye molecule, which are broadened to a continuum by collisions in the liquid phase environment of the medium. Continuous tuning over the fluorescent band system is therefore possible.

The tuning element of the dye laser consists of a diffraction grating which forms one end of the laser cavity. The angle of the grating is adjusted mechanically by the vertical motion of a precision milled screw, the position (height) of which is computer controlled (Lambda Physik FL3002E only). It should be mentioned here that the motion of the screw introduces a sinusoidally varying error in the calibration of the computer generated display. Wavelength ranges, bounded by the angle of the grating (in a particular order) from the shortest to the longest

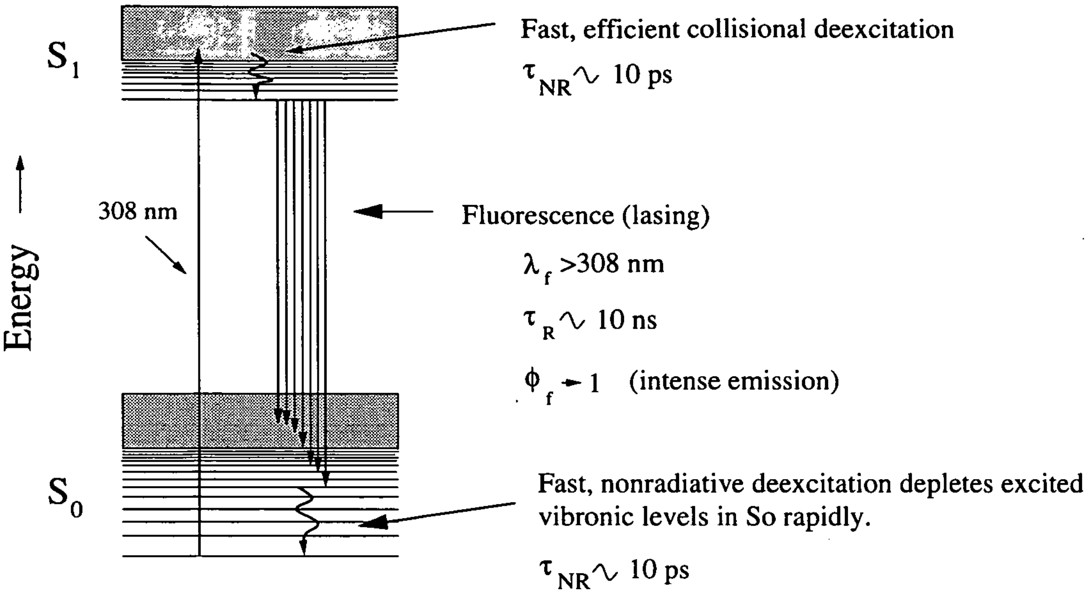

Figure 2.2: Radiative and nonradiative transitions in a dye molecule producing laser radiation.

wavelength are programmed at the computer interface and are scanned through linearly over a certain time period, given a certain scan rate, also programmed at the computer. The height of the screw, however, due to the milling, does not track perfectly linearly, at any moment in time, with the wavelength reading generated on the computer. Instead, a low amplitude sinusoidal variation with the output wavelength reading relative to the actual wavelength output, due to the grating, is observed. This calibration error is encountered only in the use of the FL3002E dye laser which, in the experiments described here, provides the required continuously scanned wavelengths.

Laser action is produced by directing around 20% of the incident 308 nm radiation into the dye cell in the cavity (oscillator). Laser pulses are then amplified by passing through a second dye cell, outside the cavity (amplifier), which is pumped by the remaining 80% of the 308 nm radiation, thus invoking stimulated emission to produce an intense laser pulse. Dye solutions are continuously flowed through the cells in order to prevent overheating and photoinduced decomposition.

Both dye lasers used in the experiments performed in this work principally operate in the same way. The FL2002 dye laser, used in the four-wave mixing experiments, can not be continuously scanned with computer control and was used to provide a fixed wavelength corresponding to a two-photon resonance in krypton. The FL3002E provided a range of frequencies, continuously tunable, to produce the range of VUV wavelengths generated by the resonant difference frequency technique (see chapter 1 and later sections in this chapter).

2.1.2 Time-of-flight mass spectrometer

The spectroscopic experiments carried out in this work all required the detection of ionic species and, furthermore, a measure of the ion signal, or extent of ionization, was necessary to infer information about the efficiency of the ionization process. A method for determining the ion signal due to several ionic species, with differing masses, created simultaneously or possessing an opposite charge, was also required. These requirements were met by using a linear time-of-flight mass spectrometer (TOF-MS). The main advantage of the TOF-MS over a simple charge collecting device is that, when coupled to an appropriate detector, it offers mass resolution of all ionized species formed by laser excitation. The principal components of the TOF-MS are listed on a schematic diagram of the instrument on figure 2.3.

The basic principle of the operation of this instrument is quite simple. Laser radiation can photoionize a sample molecule at a well defined frequency at a point defined by the intersection of the laser beam and molecular beam containing the sample molecule.

If, along the third perpendicular axis, a strong electric field is applied, then ionic species formed at the intersection are repelled by the field, provided that the ionic charge is the same as the polarity of the repelling plate. Repelled ions are then directed through a small hole into a series of ion optics (called an Einzel lens) which focuses and collimates the ion packet before entering a field-free drift region or flight tube.

The ionic species, at the point of ionization, acquire a kinetic energy and hence constant velocity, equal to the electrical energy within the field. The velocity of each ionic species is inversely proportional to their mass. Subsequently, as they travel through the field-free region, called a 'flight-tube', over a fixed distance or length, the time at which they arrive at the detector, positioned at the bottom of the flight-tube, depends upon their velocity. Thus masses are resolved in terms of the flight-time of ionic species from the ionization region to the detector. The relationship between flight-time and mass can be derived easily by equating expressions for electrical energy and kinetic energy. Neglecting constants, the relationship is; $t \propto \sqrt{M}$. An appropriate detector is a microchannel plate (MCP) which possesses a sufficiently short rise time and high sensitivity.

Supersonic jet-cooling

The gas delivery system incorporated in this experimental arrangement is provided by a pulsed nozzle, which offers the significant advantage of delivering jet-cooled sample molecules to the ionization region of the TOF-MS. This technique is commonly referred to as supersonic jet-cooling [6]. Sample molecules are seeded, at low partial pressure, into an inert carrier gas, typically helium or argon, to form a mixture with an overall backing pressure of 0.5-1.5 atm. The mixture is forced through a nozzle with a small diameter (d=250 μm) into the ionization region or jet cell of the TOF-MS, which is evacuated to <10^{-6} Torr. In the nozzle, random collisions between sample molecules and carrier gas atoms are converted into a highly directional flow. Collisions occur along the direction of the flow within and just beyond the nozzle aperture, which has the effect of

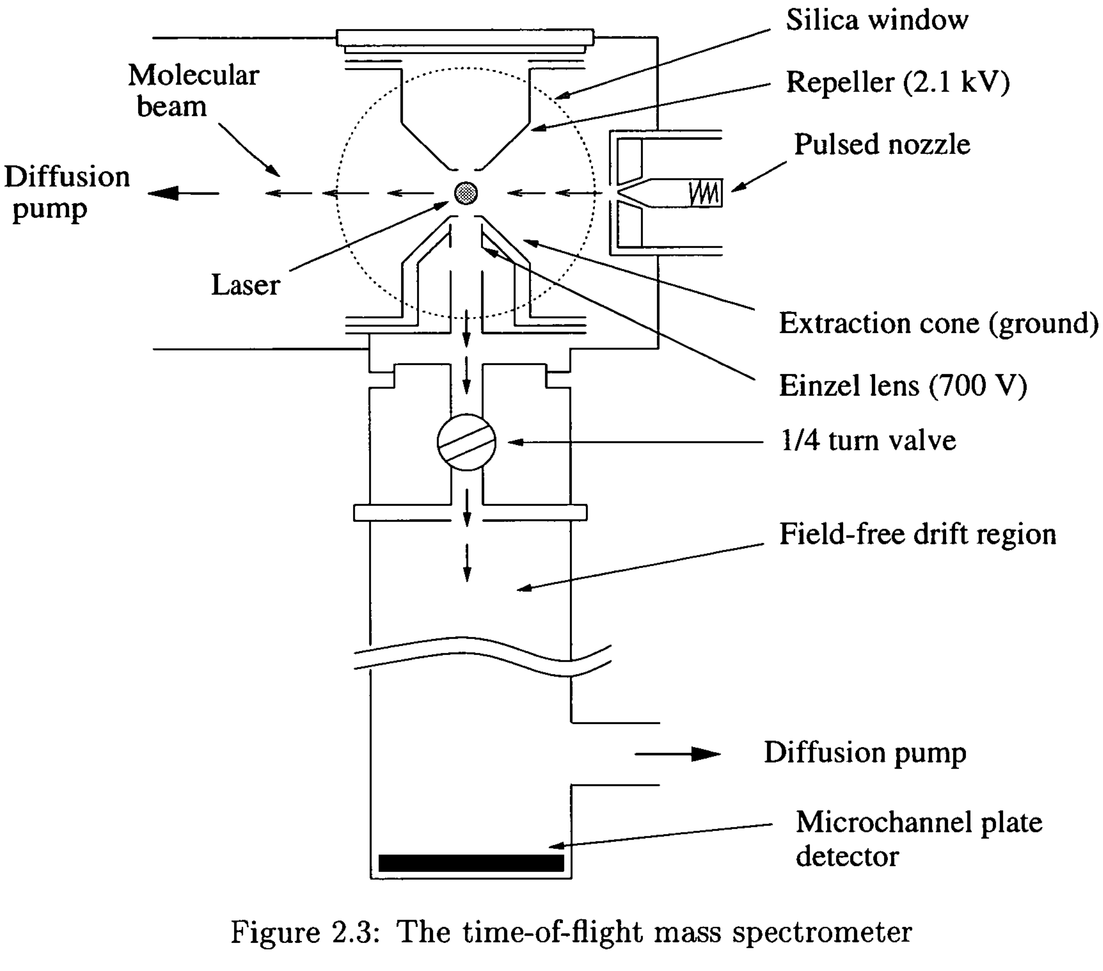

Figure 2.3: The time-of-flight mass spectrometer

producing a narrow, well-defined beam with a very small range of velocities in a highly directional sense and therefore expands into the vacuum region under strictly collision-free conditions. This produces a very low translational temperature in the jet, with the effect of drastically altering the Boltzmann distribution of populated states in the sample molecule *via* energy transfer to bulk carrier-gas translation. Consequently, non-translational motions within the molecule are converted into translational motion by collisions with carrier gas atoms in the nozzle.

The most efficient cooling is therefore in the translational modes of the molecule in the jet, producing translational temperatures of around 1 K. Rotational cooling is less efficient, however, rotational temperatures of the order 10 K are typical while vibrational cooling is least efficient with effective vibrational temperatures of 200 K produced. However, this is sufficient to ensure that the majority of sample molecules exist in the ground vibrational state. Transitions observed in the spectra of jet-cooled molecules are characterised by their narrow rotational band contours and weak hot band structure.

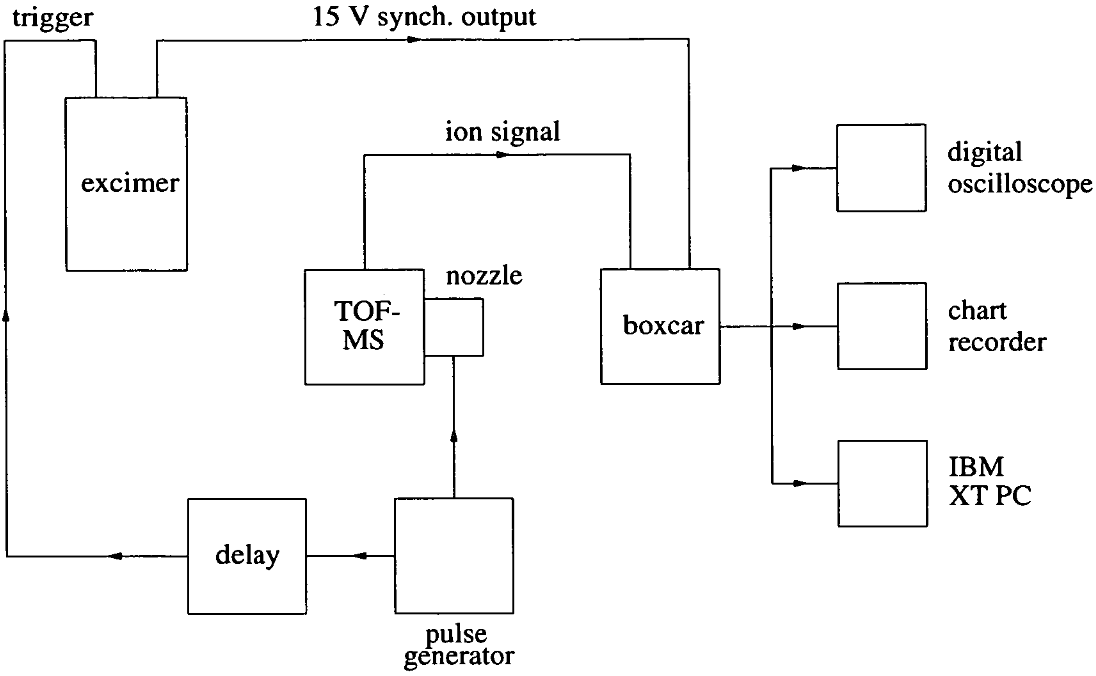

Figure 2.4: Flow diagram of electronic components controlling the firing of the laser, opening the nozzle and processing the output ion signal to chart, oscilloscope and computer.

2.1.3 Data acquisition

The overall operating mechanism of the apparatus, from the firing of the laser and the synchronised opening of the nozzle to the processing of the ion signal and subsequent output to the various diagnostic interfaces, i.e. the digital oscilloscope, chart recorder and computer, is controlled by a series of electronic devices. A flow diagram of the relevant components is shown on figure 2.4.

The nozzle is pulsed at a repetition rate determined by the pulse generator with the open time also set from this unit. The output from the pulse generator also triggers the firing of the excimer laser. This signal is sent *via* a delay generator to an input on the control unit of the excimer laser. A variable delay allows optimisation of the timing between the firing of the laser and the opening of the valve and the admission of gas pulses into the ionization chamber of the TOF-MS, allowing a period of a few microseconds for the gas pulse to travel from the nozzle aperture to the point of intersection of the laser beam and the entrance to the flight-tube.

The control unit of the excimer is also equipped with a synchronous output which is connected to the trigger input of a boxcar averager (Stanford Research Systems SRS 265). The boxcar averager essentially consists of a switch connected between the input source and an averaging device, usually a low-pass filter with a time constant greater than the period between repetitions [7]. On triggering (switch open), the boxcar averager operates by opening for a defined period of time, shorter than the time interval between successive pulses. During this open time, the boxcar collects and stores any electrical signal (and noise) from some input source, in this case the amplified output from the MCP detector situated at the base of the TOF-MS flight-tube. At each laser shot, the boxcar is triggered and, because of the long time constant of the low-pass filter, the final output is the average of signals that are present during the open times over a set number of repetitions. The open time of the boxcar is determined by the range of flight-times to be measured. The output of the boxcar is displayed on a digital oscilloscope in the form of the averaged time-of-flight spectrum detected at the

MCP. In order to record the spectrum due to a single ionic fragment, a device coupled to the boxcar, known as a gate, allows the boxcar to collect and integrate only those signals arriving at a specific time delay. This is done by introducing the position of the gate, in time, on to the display of the oscilloscope and adjusting the position to the appropriate peak in the time-of-flight spectrum, corresponding to the ionic fragment to be collected. This mass-resolved signal is then output to a chart recorder and, for subsequent data analysis, to an IBM XT personal computer.

2.1.4 Resonant four-wave difference frequency mixing

Vacuum-ultraviolet (VUV) laser radiation was generated using resonant four-wave difference frequency mixing (RDFM) in krypton gas [8,9]. Two dye lasers, pumped by a XeCl excimer laser (Lambda Physik EMG 201 MSC), were used in the experiment: the frequency doubled output of a Lambda Physik FL2002 dye laser, using Stilbene 3 dye, was tuned to one of three two-photon resonances in krypton at 92 308 cm^{-1}, 93 123 cm^{-1} and 94 094 cm^{-1}[10]. The third photon in the RDFM process was provided by a tunable dye laser (Lambda Physik FL3002E) operating with a range of dyes in the visible frequency range. The dyes used in the experiments on ion-pair formation from I_2 and ICl are detailed separately in the appropriate chapters.

Figure 2.5 shows the arrangement of the laser system and optics used to overlap the two beams collinearly and direct into the mixing cell. The precise wavelength of the two- photon resonance in krypton was determined by extracting a small portion of the UV laser beam into an ionization cell, containing krypton at *ca.* 20 Torr and measuring the ionization signal. A large increase in signal was observed at a resonant frequency. The two beams were passed through a series of prisms and overlapped at a beam combiner.

Figure 2.6 shows in detail the experimental arrangement for VUV generation by RDFM, ionization of jet-cooled sample molecule, subsequent detection of ions by time-of-flight mass spectrometry and on-axis detection of VUV radiation. Collinear UV and visible beams were focussed into a 40 cm length, 2.5 cm diameter glass cell containing *ca.* 20 Torr krypton. Vacuum-UV radiation exiting the cell was focussed by a translatable 5 cm focal length LiF lens into the ionization region of a time-of-flight mass spectrometer (TOF-MS).

Ions formed were extracted perpendicularly to the laser and molecular beams, by a repeller at 2.1 kV, into the TOF-MS. In our set-up, a slight modification to the high voltage supply allowed negative ions to be detected. A microchannel plate (MCP) detector, held at 5 kV, at the bottom of the flight tube detected iodine ions. The ion signal was amplified and processed by a boxcar integrator

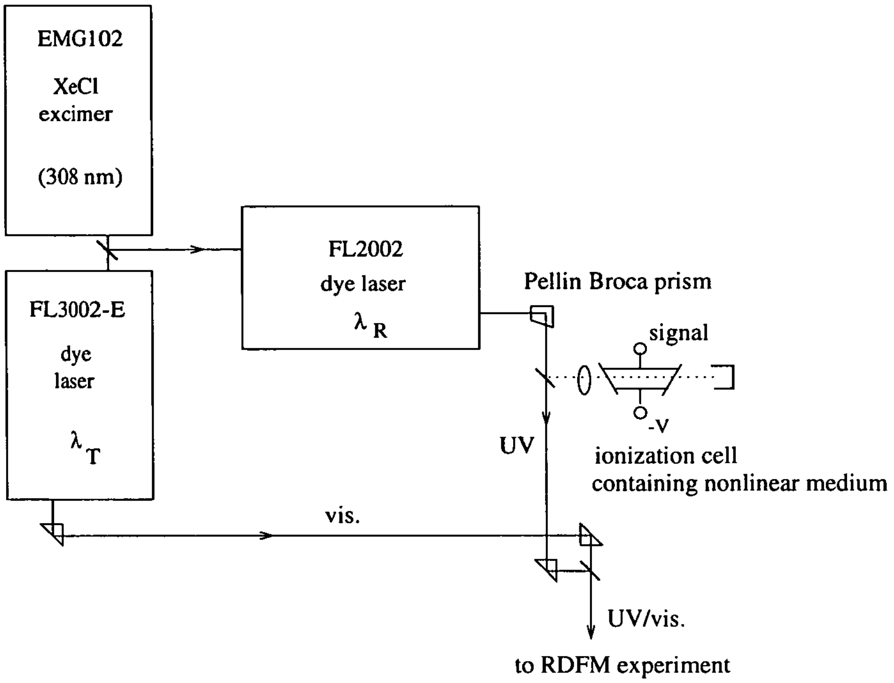

Figure 2.5: Experimental arrangement of lasers and optics for collinear UV and visible beam paths.

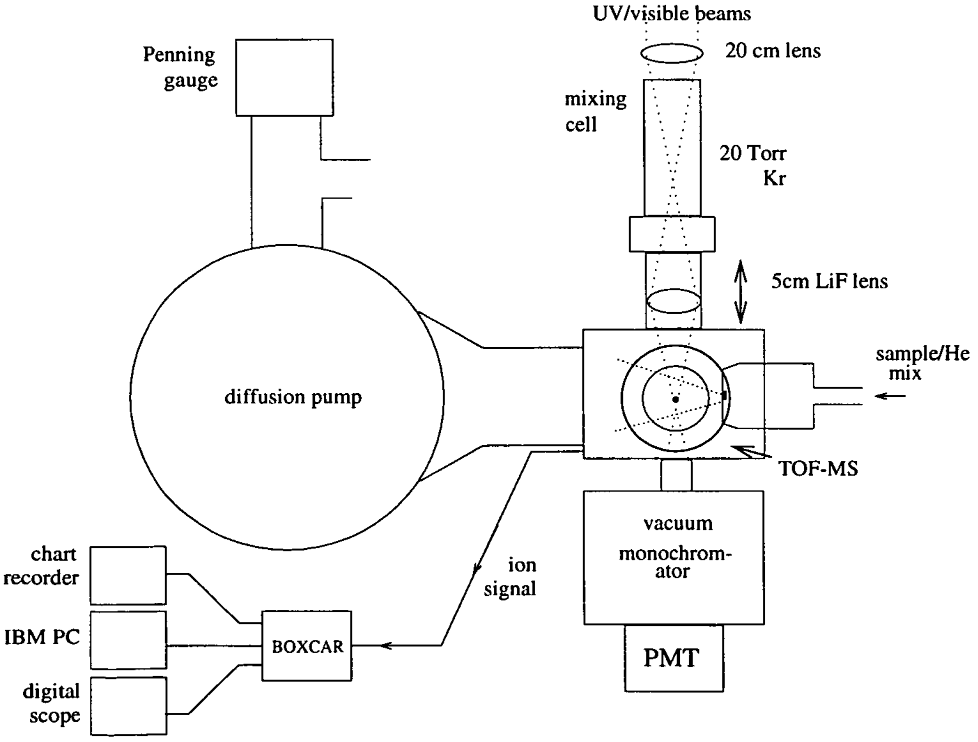

Figure 2.6: Detailed diagram of four-wave mixing cell, supersonic jet cell and detection apparatus.

(Stanford Reaserch Systems SRS265) and output to a digital oscilloscope, chart recorder and IBM XT PC computer.

A vacuum monochromator (Acton Research Corporation, Model VM-502) was coupled to the jet cell, on the laser beam axis. The monochromator chamber pressure was maintained at $<10^{-6}$ Torr using a turbo/rotary pump combination. Vacuum-UV entering the monochromator through a MgF_2 window, incident on a concave holographic grating was directed to the exit slit and detected by a solar blind photomultiplier (Hamamatsu R1459).

The presence of water in the four-wave mixing cell was observed during the experiments on ion-pair formation from ICl. At VUV wavenumbers above 80 300 cm^{-1} a discrete band system superimposed on the ion pair excitation function due to $^{35}Cl^-$ ions was observed. This was detected as a series of dips in the ion function at wavenumber positions corresponding to structure in the absorption spectrum of the $C \leftarrow X$ band system of water[11]. Figure 2.7 shows the $^{35}Cl^-$ mass-resolved ion-pair excitation function in this wavenumber region with pronounced dips due to water absorption, at wavenumber positions 80 600, 80 685, 80 707 and 80 730 cm^{-1}, superimposed on the spectrum.

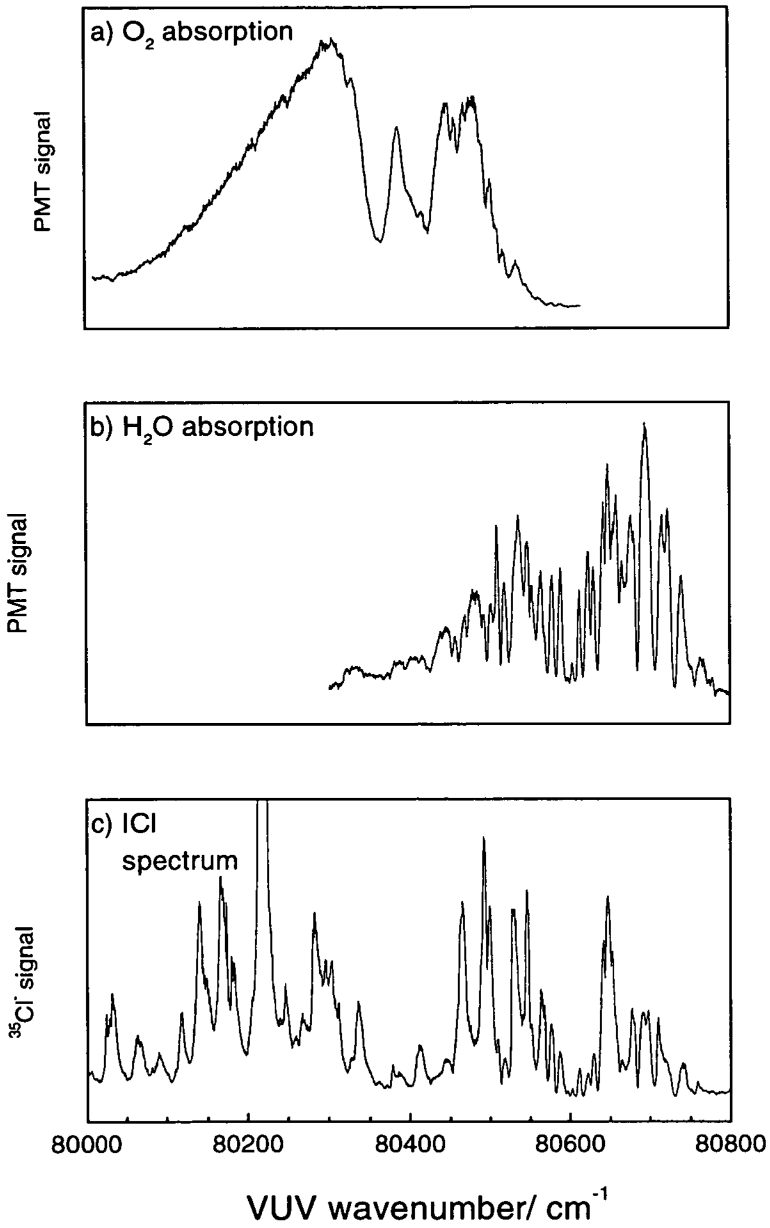

Figure 2.7: VUV transmission spectrum of a) O_2 and b) H_2O with PMT signal detecting VUV, recorded as a function of wavenumber. The ICl spectrum (c), recorded on the $^{35}Cl^-$ mass channel in the same region, shows dips corresponding to minima in the transmission spectra of O_2 and H_2O.

2.1.5 [2+1] REMPI experiments, with polarization studies and rotational band contour analysis

The experiment was performed using one-colour, [2+1] REMPI with mass- analysis of molecular and atomic ion signals by time-of-flight mass spectrometry. Molecular bromine contained in a bulb was jet-cooled by seeding in He carrier gas. The experimental arrangement is shown on figure 2.8.

Tunable UV radiation was generated by a Lambda Physik 3002E dye laser pumped by a Lambda Physik EMG 201MSC excimer laser. The two-photon frequency range was covered using the frequency doubled output of the dyes Coumarin 153, Coumarin 307 and Coumarin 102 and the fundamental of PTP. A BBO crystal was used for frequency doubling, with the resultant UV output separated from the fundamental using an arrangement of Pellin Broca prisms. Circular polarization was achieved by passing the beam through a Soleil-Babinet compensator, a description of which follows later in this section. Slow scans of the dye laser were used to collect some spectra to produce fully resolved rotational band contours.

The molecular beam was formed by passing a mixture of Br_2 and He gas through a pulsed nozzle (General Valve) with a 250 μm diameter aperture. The resultant supersonic jet provided jet-cooled bromine molecules in the ionization

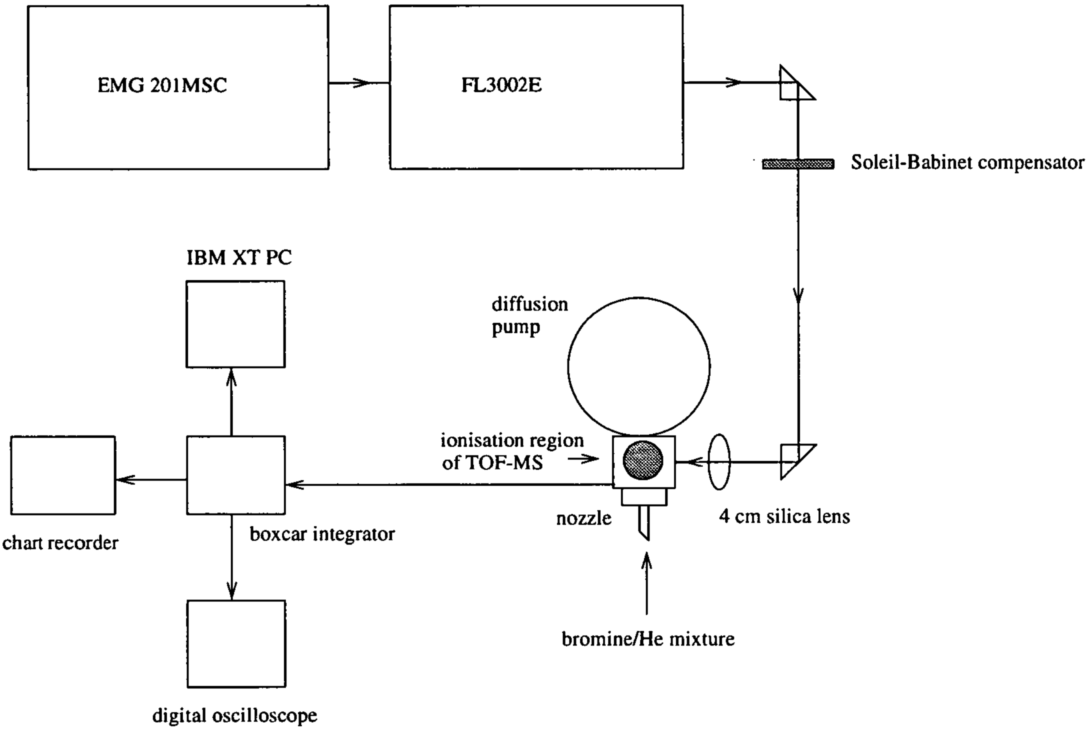

Figure 2.8: Experimental arrangement for [2+1] REMPI studies of jet-cooled Br_2, incorporating jet-cooling of the sample molecule and control over the polarization aspect, *via* the Soleil-Babinet compensator, of the exciting laser radiation.

region of the linear time-of-flight mass spectrometer. The mixture contained 50 Torr of Br_2 with *ca.* 500 Torr of He carrier gas for vibrationally resolved spectra and with *ca.* 150 Torr of He for the rotational band contour scans, giving a rotational temperature in the beam of around 20 K. Ions were collected perpendicular to the laser and molecular beams. Mass resolved ion signals, due to $^{79}Br^+$, $^{81}Br^+$ and $^{79}Br_2{}^+$ were processed by a Stanford Research SR20 boxcar integrator and stored on an IBM XT personal computer.

The Soleil-Babinet compensator[12] is an optical device which can vary the polarization of radiation continuously from linear to circular. The compensator consists of two schlieren-free crystalline quartz plates shaped as wedges, cut so that the crystalline optical axes are parallel to the surfaces of the plates. These plates are stacked on top of each other, such that the crystalline optical axes of each wedge are perpendicular to each other, with one fixed and the other with variable movement. In this way, the relative thickness of the plates is continuously adjustable. When both are of equal thickness, any phase difference from the first plate is exactly cancelled out on passing through the second plate. By varying the thickness, a net phase difference can be introduced on passing through the second plate. Circular polarization results only when this phase difference is 45^{o}, with vertical or horizontal linear polarization at 0^{o} and 90^{o} angles, respectively and, indeed, the scale on these devices is circular, graded from 0^{o} to 360^{o}.

A Soleil-Babinet compensator was used in this experiment to select a desired polarization state of laser radiation (ie. circular polarization) but can conversely be applied to determining the polarization aspect of emitted light very precisely.

2.2 Femtosecond Lasers Used for Harmonic Generation

Part of this project comprised the use of the Laser Support Facility (LSF) based at the Rutherford-Appleton Laboratory in England. The LSF operates a suite of state of the art table-top laser systems and associated instrumentation and support. Beam time using the femtosecond laboratory was applied for and granted for two separate sessions of one month at a time. Appartus constructed in Edinburgh was used to investigate the possibility of using high intensity femtosecond pulses to generate high order harmonics, in a suitable nonlinear medium, with wavelengths in the VUV frequency range. The generated short wavelength radiation was characterised and optimised in order to test its suitability as a source for spectroscopic experiments. These experiments are detailed in Chapter 6.

2.2.1 The Tsuanmi 50 fs laser system

The experimental arrangement is shown on figure 9. Laser pulses of around 50 fs pulse length and 10 nJ energy were generated by a mode-locked titanium sapphire laser (Spectra-Physics Tsunami) pumped by the 7 W output of a cw argon-ion laser (Spectra-Physics 171). This produced an 82 MHz train of pulses, tuneable from 730 nm to >800 nm wavelength. Pulses were stretched first to around 500 fs by passing twice through a prism pair (SF10 glass), using negative group velocity dispersion (GVD), with a path length of around 2 m. Pulses were then amplified using a modified three stage dye laser amplifier (Spectra-Physics PDA1), pumped by the frequency-doubled output of a conventional Q-switched Nd:YAG laser. Rhodamine 700 dye gave the best performance yielding 750 nm radiation with pulse energy 100 μJ at a repetition rate of 10 Hz. Pulses were then recompressed temporally using the positive GVD of an SF10 glass block, to around 50 fs.

This technique of stretching, amplification and recompression of pulses is known as chirped pulse amplification (CPA) which has a number of advantages for generating clean, ultrashort pulse length radiation [13,14].

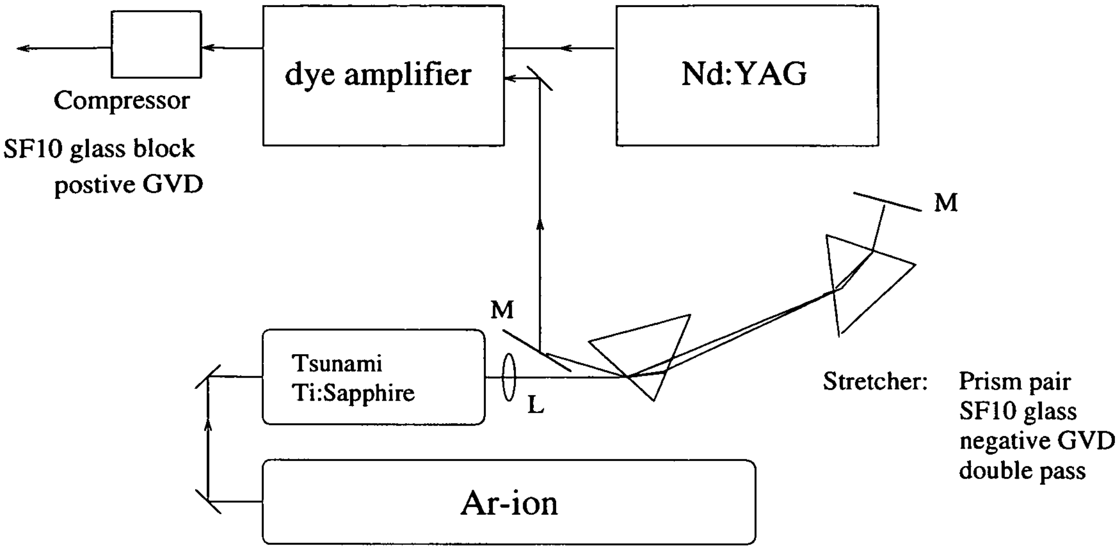

Figure 2.9: The femtosecond laser system at the RAL-LSF.

2.2.2 Chirped-pulse amplification

The amplification of ultrashort laser pulses to high energy levels demands three major requirements. First, the bandwidth of the amplifying, or gain, medium must be large enough to accomodate the full spectrum of the laser pulse. Second, the amplifying medium should ideally possess a high energy storage at the pulse wavelengths to be amplified. Third, the laser intensity should be kept low enough to avoid nonlinear effects in the amplifying medium from distorting the pulse wave-front.

The first of these requirements is a consequence of the relationship between the laser pulse duration and the bandwidth, given by the Fourier transformation from the time domain into the frequency domain, given by the time-bandwidth equation $\Delta\nu\tau$=0.5. Hence, for a 50 fs pulse, with wavelength 750 nm, a medium with bandwidth >330 cm^{-1} is required, equivalent to $\Delta\lambda$=20 nm at this wavelength. However, in order to avoid gain narrowing; an effect where the various frequencies in the spectrum of the laser pulse are unequally amplified, given the frequency dependence of the amplifying medium, the pulse must first be stretched temporally. This technique forms the basis of chirped pulse amplification (CPA).

The second requirement, regarding the energy storage of the medium, depends on the saturation fluence, F_s, or maximum flux capacity, of the amplifying medium. Ideally, the input fluence should be of the same order as F_s, which is given by $h\nu/\sigma$ (where σ is the stimulated emission cross-section). The saturation fluence of a dye laser is of the order of mJ/cm^2, due to the large emission cross-section, whereas solid state media such as Nd:YAG and Ti:sapphire can store up to 1 J/cm^2.

However, a balance must be met between this condition and the third condition, that the input laser intensity should be sufficiently low to avoid nonlinear effects in the medium causing wavefront distortion of the input pulses. This excludes solid-state materials as suitable amplifying media due to their high saturation fluences since the input laser intensity required, of the order 1 TW/cm^2 with subpicosecond pulse lengths, is far greater than the acceptable level at which

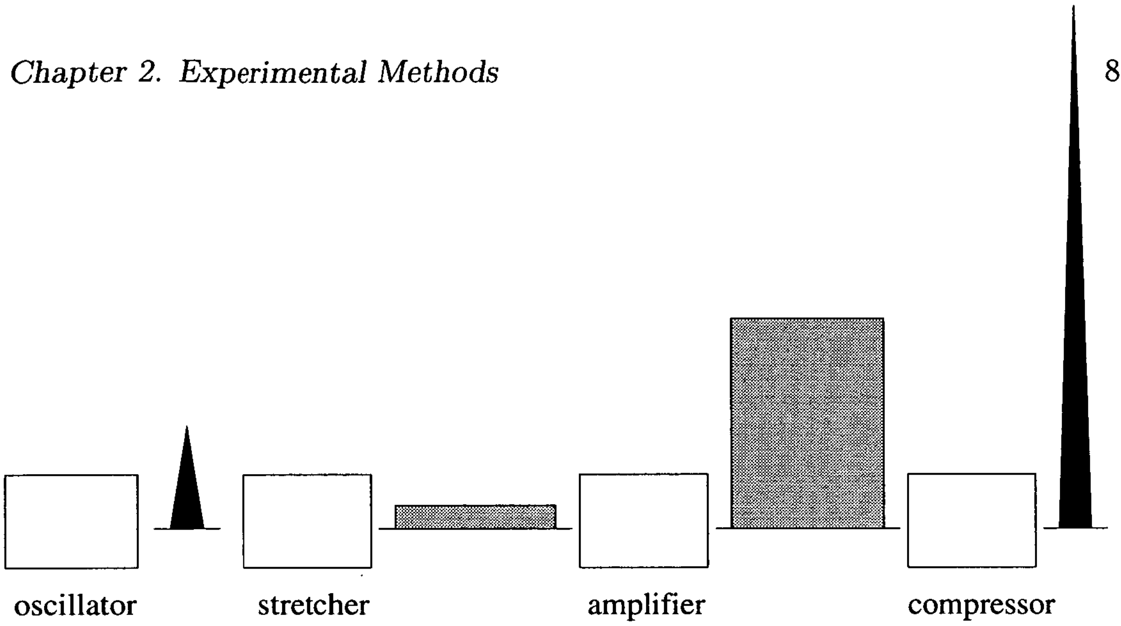

Figure 2.10: Chirped pulse amplification. The pulse is stretched temporally in order to lower the peak intensity before amplification. After the stored energy is extracted from the amplifier, the pulse is compressed temporally to the initial pulse length.

adequate beam quality can be maintained.

The advantage of chirped pulse amplification is that saturation fluences can be achieved with low power pulses. The power of the input pulse can be reduced significantly by first stretching the pulse temporally, by up to a factor of a hundred. The pulse can then be amplified producing a clean pulse, safely within the saturation level of the gain medium. The pulse can then be recompressed carrying the same power output as the stretched, amplified pulse. This process is shown schematically on figure 10. Hence, the output pulse is an ultrashort, high power pulse, of the order of 1 GW for a dye or excimer amplifier and of the order 1 TW for a solid state (Nd:glass, Ti:sapphire) amplifier.

The femtosecond laser system at the RAL-LSF has been developed as a source of GW pulses, using a dye laser amplifier. Typical peak intensities of the order 10^{14} W cm^{-2} can be developed with focusing.

2.3 References

[1] P.J. Wilson, T. Ridley, K.P. Lawley and R.J. Donovan, *Chem. Phys.* **182** (1994) 325

[2] R.J. Donovan, J. Goode, K.P. Lawley, T. Ridley and A.J. Yencha, *J. Phys. Chem.* **98** (1994) 2236

[3] M.S.N. Al-Kahali, R.J. Donovan, K.P. Lawley, Z. Min and T. Ridley, *Chem. Phys.* **208** (1996) 165

[4] R.J. Donovan, R.V. Flood, K.P. Lawley, A.J. Yencha and T. Ridley, *Chem. Phys.* **164** (1992) 439

[5] K.P. Lawley, T. Ridley, Z. Min, P.J. Wilson, M.S.N. Al-Kahali and R.J. Donovan, *Chem. Phys.* **197** (1995) 37

[6] J.M. Hollas, *Modern Spectroscopy*, 2nd ed., John Wiley & Sons

[7] R.P. Wayne, *Chemical Instrumentation*, Oxford University Press (1994)

[8] J.P. Marangos, N. Shen, H. Ma, M.H.R. Hutchinson and J.P. Connerade, *J. Opt. Soc. Am. B* **7** (1990) 1254

[9] C.E.M. Strauss and D.J. Funk, *Opt. Lett.* **16** (1991) 1192

[10] J. Sugar and A. Musgrove, *J. Phys. Chem. Ref. Data* **20** (1991) 859

[11] G. Herzberg, *Electronic Spectra of Polyatomic Molecules*, Van Nostrand Rheinhold Company (1966)

[12] C.G. Zimba, T.B. Freedman, K.M. Spencer, X.M. Hu and L.A. Nafie, *Chem. Phys. Lett.* **134** (1987) 233

[13] G. Mourou and D. Umstadter, *Phys. Fluids. B* **4** (1992) 2315

[14] K. Yamakawa, P.H. Chiu, A. Magana and J.D. Kmetec, *IEEE J. Quant. Electron.* **30** (1994) 2698

Chapter 3

The [2+1] REMPI spectrum of Jet-Cooled Br_2

3.1 Introduction

The Rydberg states of Br_2 have previously been studied extensively by Venkateswarlu using high resolution vacuum ultraviolet absorption spectroscopy[1] and have subsequently been re-examined using a synchrotron radiation source[2–4] at lower resolution. However, in each of these studies, excited states were accessed and observed at the one-photon level, thus it has only been possible to observe the *ungerade* Rydberg states. Transitions to the *gerade* states are only symmetry allowed at the two- (or higher, even number) photon level by the selection rule

$$\mathrm{g} \rightarrow \mathrm{u} \rightarrow \mathrm{g}$$

With the introduction of moderate power lasers, coherent excitation of molecules, *via* virtual states, by two or more photons has been made possible. The technique of [2+1] resonance enhanced multiphoton ionization (REMPI) spectroscopy is an efficient method for studying two-photon transitions within molecules. In general, two UV/visible photons coherently excite a molecule. If an allowed vibronic transition is reached with two photons, a third photon, possibly of the same frequency ionizes the molecule from the populated vibronic state. The spectrum is recorded by collecting the ion signal as a function of wavelength.

The [2+1] REMPI spectrum of Br_2 has been previously obtained using linearly polarized light only[5], in the region 61 000-85 000 cm^{-1} on a room temperature, low pressure sample of bromine, detecting all ions. The spectrum obtained showed a characteristic pattern of strong transitions to two Ω states based on each of the two spin-orbit components of the ionic core (Ω_c=3/2, 1/2). The quantum defects of the Rydberg states correlated well with expected quantum defect values for *n*s series and the spectrum was assigned as such. In the experiments reported here, the one-colour [2+1] REMPI spectrum of Br_2 has been recorded using linearly and circularly polarized light excitation, jet-cooling of the sample and mass resolution of the ionic products. Jet-cooling provided a cleaner spectrum with sharper peaks, due to narrower rotational band contours while analysis of the polarization behaviour and selected rotational band contours, strongly suggested a significant re-assignment of the spectrum with *n*d series, not *n*s series, being dominant.

Complete vibronic assignments of several Rydberg states are given here, including six new progressions. The anomalous behaviour of one of the 5s Rydberg states observed using linear and circular polarization is discussed here in terms of processes occuring at the one-photon level of the two-photon excitation mechanism. Evidence of Rydberg/ion-pair interactions has been inferred from the experimental results and is discussed also. The re-assignment of the spectrum from predominantly ns states to nd states prompted a re-examination of the [2+1] REMPI spectra of Cl$_2$ and I$_2$, given the similarity of these spectra to that of Br$_2$, presented here.

3.2 Experimental

The experimental arrangement is described in chapter 2, section 2.4. The two-photon frequency range was covered using the frequency doubled output of the dyes Coumarin 153, Coumarin 307 and Coumarin 102 and the fundamental of PTP.

No power normalisation of the spectra was carried out since reliable intensity data were available from previous work on this system using [2+1] REMPI on a low pressure, room temperature sample of bromine[5]. An offset of +2 cm^{-1} has been included in the wavenumber positions of vibronic assignments, determined from an internal calibration using the accurately known wavenumber positions of several atomic lines observed throughout the spectrum.

3.3 Results

3.3.1 General features

The two-photon spectrum of Br_2 has been recorded in a [2+1] REMPI experiment, between 56 000 and 86 000 cm^{-1}. Using time-of-flight mass spectrometry, spectra from ion signals due to $^{79}Br^+$, $^{81}Br^+$ atomic ions and the $^{79}Br_2{}^+$ molecular ion were obtained simultaneously. A composite of spectra recorded on the $^{79}Br^+$ and $^{79}Br_2{}^+$ mass channels in the range 68 000 to 86 000 cm^{-1} with linearly polarized light is shown on the upper and lower traces, respectively, on figure 3.1.

Spectra in the range 68 000 to 86 000 cm^{-1} recorded with linearly polarized light on the $^{79}Br^+$ mass channel are shown, labelled, in figures 3.2 to 3.5. Spectra recorded on the molecular ion mass channel ($^{79}Br_2^+$) show no structure due to Rydberg states with n ≥6, with the exception of the two [1/2]7d states which lie above the first ionization potential (IP) and are observed to autoionize.

Transitions to the higher energy Rydberg states were therefore assigned from spectra recorded on the $^{79}Br^+$ atomic ion mass channel. Isotopomer shift data were used to confirm some vibrational assignments by comparison of spectra recorded on the $^{79}Br^+$ and $^{81}Br^+$ mass channels. However, since structure in each spectrum is due to an equal probability of contributions from the $^{79}Br^{81}Br$ isotopomer and either $^{79}Br_2$ or $^{81}Br_2$, then it is necssary to deconvolute each peak into mass-resolved components. This was not practicable since the typical bandwidth of individual bands in the spectra was measured to be *ca.* 12 cm^{-1} (fwhm), which is comparable to the isotopomer shift between v'=4 levels of the $^{79}Br^{81}Br$ and $^{79}Br_2$ species. Hence, at the resolution of the peaks observed, it was difficult to identify isotopomer shifts precisely. Origin bands were assigned to congruent peaks, in terms of wavenumber position, in both mass-resolved spectra. Therefore, at best it was possible to distinguish between origin and vibrational bands. However, in some cases, it was possible to measure the shift between peaks in two isotopomer spectra and assign with some confidence a vibrational quantum number, based on calculated frequency shifts between vibrational levels of different isotopomers. A full vibrational analysis of all the Rydberg states assigned in the spectrum is presented in tables 3.1 and 3.2.

Analysis of the spectra recorded on the atomic mass channels revealed several atomic transitions which have been identified and assigned. Accurate measurement of the positions of these lines provided a suitable means of calibrating the spectrum by interpolation. The observed and accurately known[6] positions of atomic lines in the [2+1] REMPI spectrum of bromine are given in table 3.3. Terms for each transition and the initial state of the bromine atom are also given here. It is seen from the calculated difference between the observed and literature wavenumber positions of the atomic bromine transitions that a systematic error with an average value of +2 cm^{-1} is present throughout the spectrum. Hence, accurate values for wavenumber positions of vibronic structure in the spectrum were derived by subtracting this error.

Despite the congestion of the spectrum recorded on the atomic ion mass channel, six additional Rydberg state progressions, not previously assigned in the room temperature studies[5], were identified. Wavenumber positions of all assigned vibronic transitions, observed on spectra recorded on the atomic ion mass channels, are presented in tables 3.1 and 3.2.

3.3.2 Assignment of Rydberg states

In the previous, room temperature study, Rydberg states were assigned using quantum defects derived from the Rydberg equation. The IP's of the [3/2] and [1/2] ionic states of (^{79}Br$_2^+$) were determined accurately, by zero electron kinetic energy (ZEKE) photoelectron studies[7], to be 84 823 and 87 645 cm^{-1}, respectively. Quantum defect values for each Rydberg state assigned are given in table 3.1 and 3.2 and generally agree well with the predicted range of values for nd Rydberg states of the bromine atom ($\delta(n\mathrm{d})\approx 0.9\text{-}1.4$)[6].

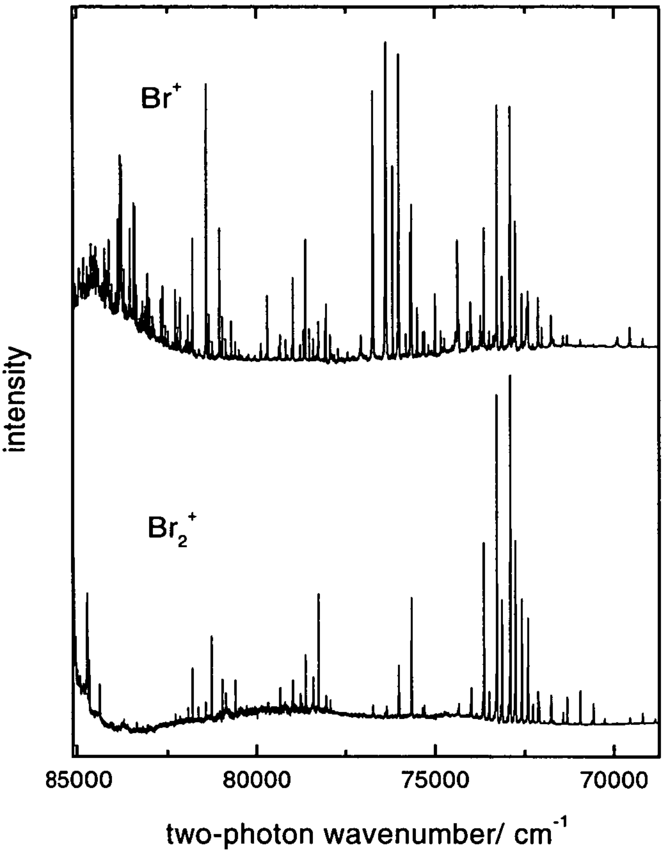

Figure 3.1: [2+1] REMPI spectrum of Br_2 between 69 000 and 86 000 cm^{-1} using linearly polarized light. The upper trace shows the spectrum recorded on the $^{79}Br^+$ mass channel. The lower trace shows the spectrum recorded on the $^{79}Br_2{}^+$ mass channel.

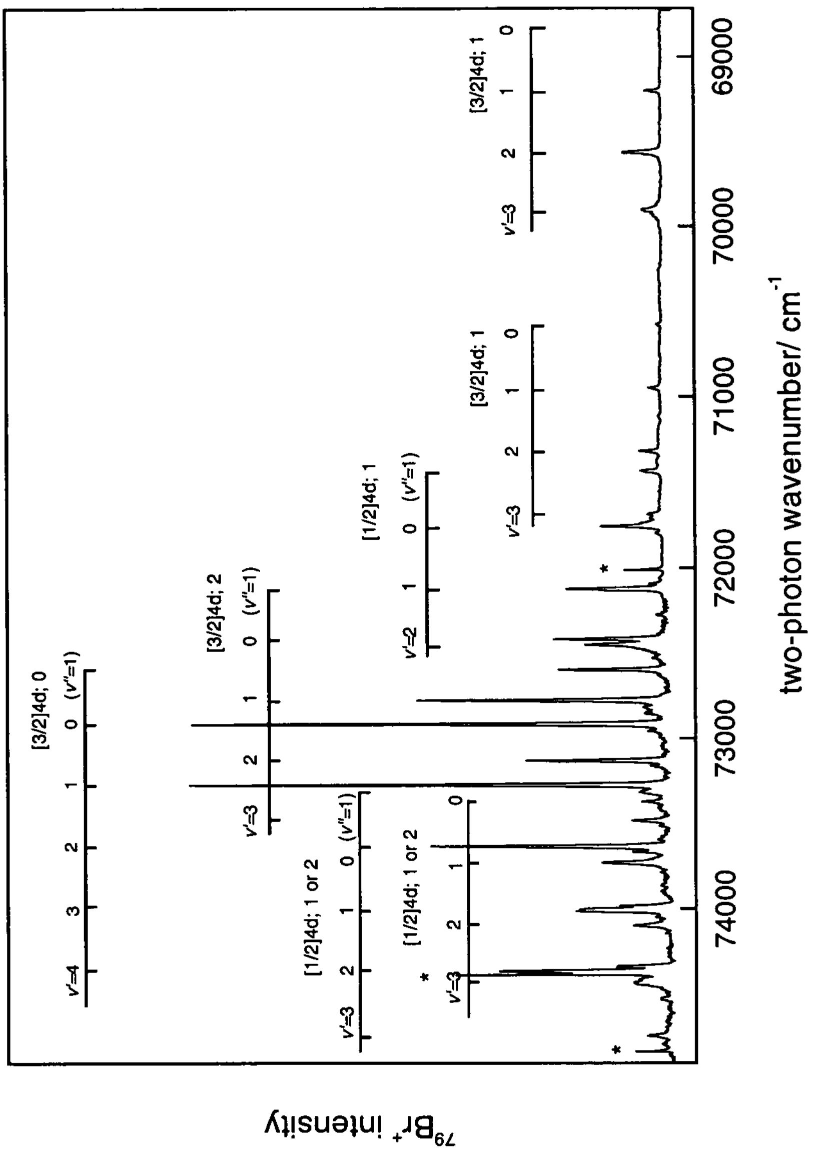

Figure 3.2: [2+1] REMPI spectrum of Br_2 between 69 000 and 75 000 cm^{-1} using linearly polarized light. The spectrum was recorded on the $^{79}Br^+$ mass channel. Atomic transitions are marked with an asterisk.

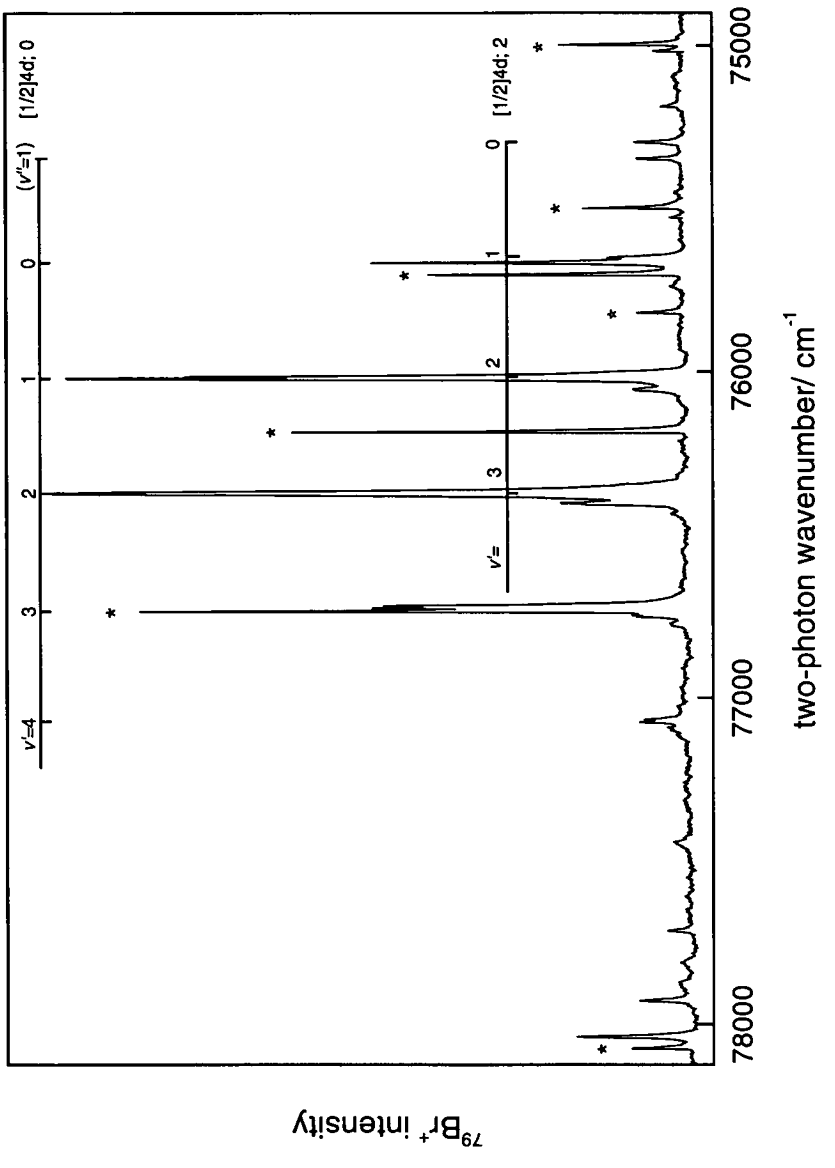

Figure 3.3: [2+1] REMPI spectrum of Br_2 between 75 000 and 78 000 cm^{-1} using linearly polarized light. The spectrum was recorded on the $^{79}Br^+$ mass channel. Atomic transitions are marked with an asterisk.

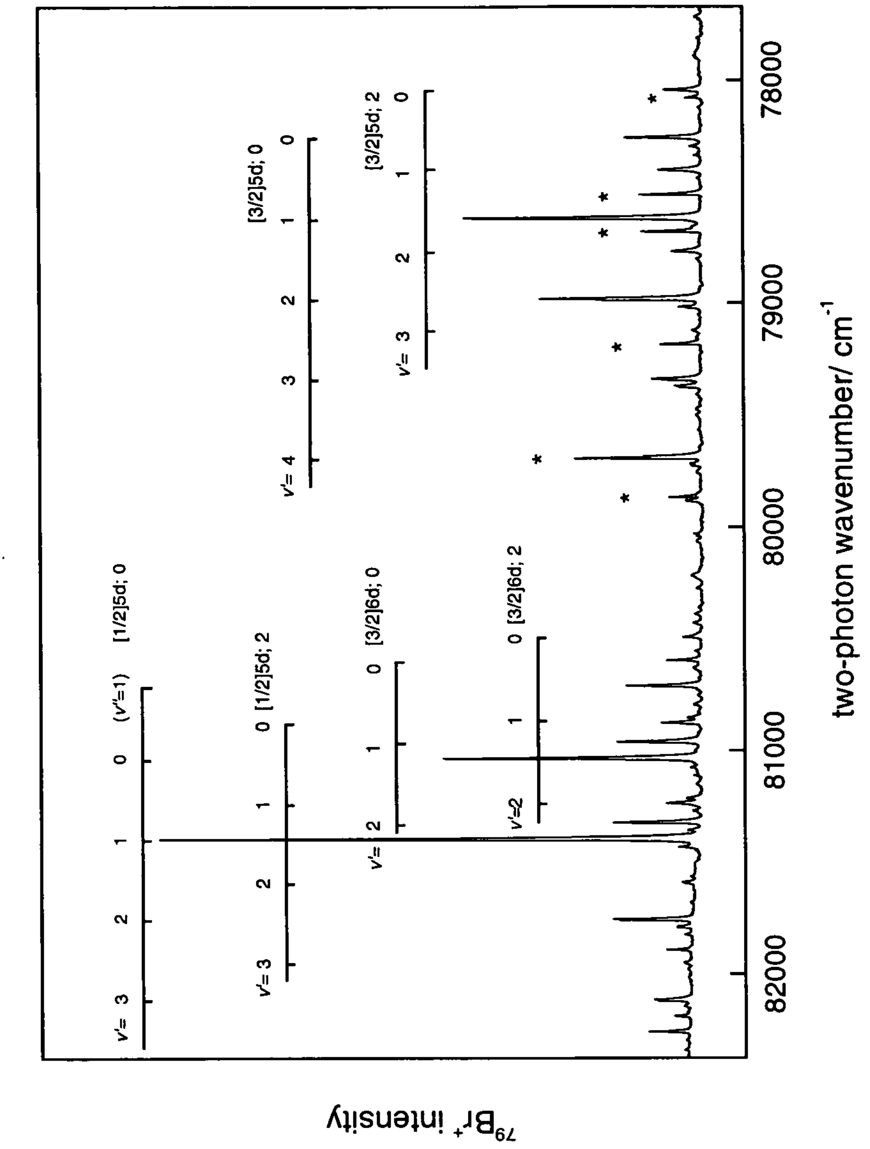

Figure 3.4: [2+1] REMPI spectrum of Br_2 between 78 000 and 82 000 cm^{-1} using linearly polarized light. The spectrum was recorded on the $^{79}Br^{+}$ mass channel. Atomic transitions are marked with an asterisk.

However, quantum defect analysis was not sufficient to assign the entire spectrum unambiguously. In this work, as an aid to assignment, spectra were recorded with both linearly and circularly polarized light and, in addition, slow scans of certain electronic origin bands have been recorded which show a characteristic rotational band contour. Three bands in the region 72 000 to 75 000 cm^{-1} are discussed here and the conclusions reached extrapolated to assign the remainder of the spectrum.

The isotopomer data confirmed some vibronic assignments of the Rydberg state progressions. Progressions in v' up to $v'=4$ are observed for some of the Rydberg states. The isotope shifts between vibrational levels $v'=0$, 1, 2, 3 and 4 for isotopomers $^{79}Br_2{}^+$ and $^{79}Br^{81}Br^+$, calculated using an ω_e' value of 360 cm^{-1} are 0, 2, 4, 7 and 9 cm^{-1}, respectively. Wavenumber separations between vibrational progression members of Rydberg states typically lie in the range 345-378 cm^{-1}, as shown in tables 3.1 and 3.2.

3.3.3 Linear and circular polarization effects

The [2+1] REMPI spectra between 72 300 and 74 800 cm^{-1}, collected on the $^{79}Br^+$ mass channel, using linearly polarized light (upper trace) and circularly polarized light (lower trace) are shown on figure 3.6. The figure shows that vi-

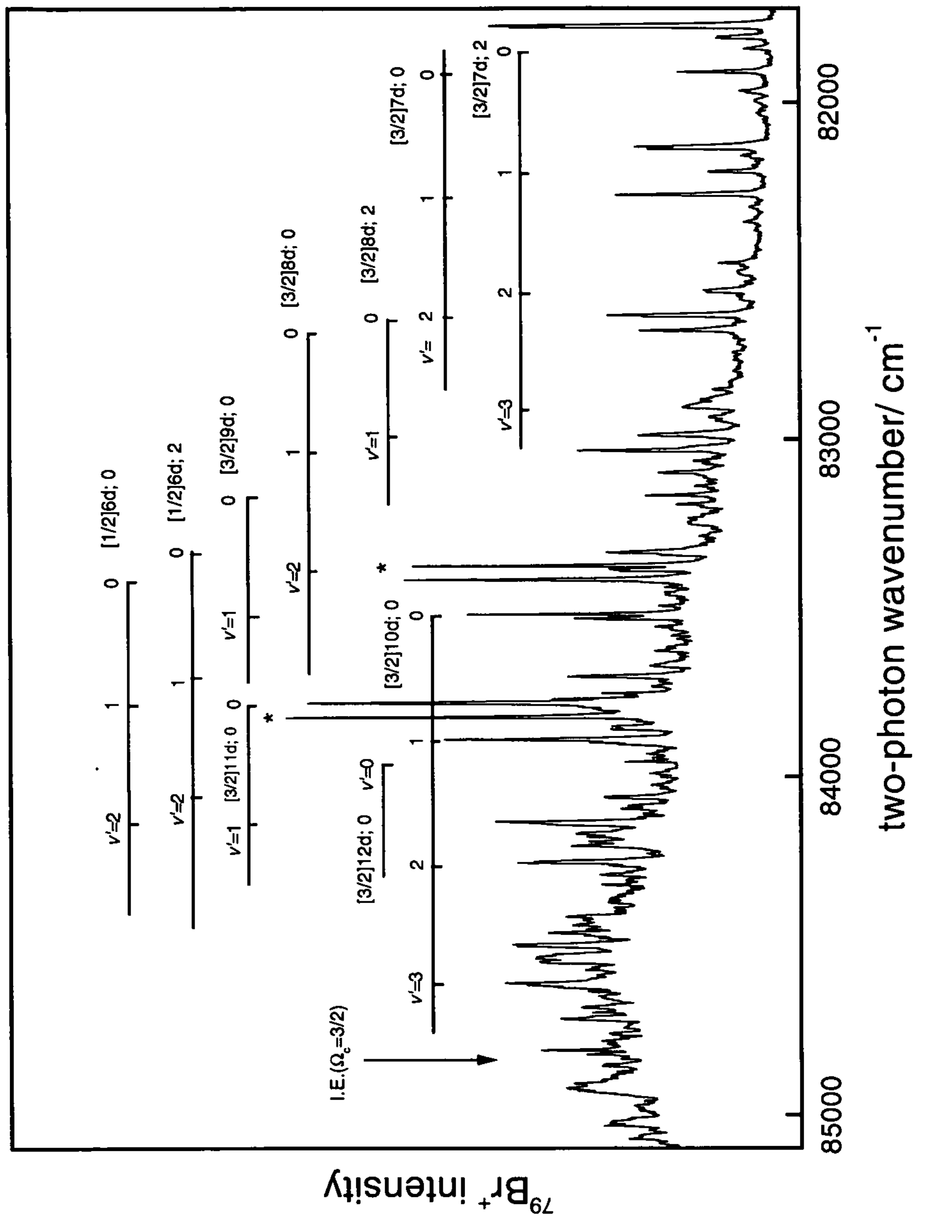

Figure 3.5: [2+1] REMPI spectrum of Br_2 between 82 000 and 85 000 cm^{-1} using linearly polarized light. The spectrum was recorded on the $^{79}Br^+$ mass channel. Atomic transitions are marked with an asterisk.

Rydberg state	$(n-\delta)$	(0,1)	(0,0)	(1,0)	(2,0)	(3,0)	(4,0)
[3/2]4d; 1	2.62		68 835 *366*	69 201 *360*	69 561 *339*	69 900	
[3/2]4d; 1	2.78		70 576 *371*	70 947 *370*	71 317 *366*	71 683	
[1/2]4d; 1	2.63	71 428 *-324*	71 752 *367*	72 119 *328*	72 447		
[3/2]4d; 2	2.97	72 086 *-325*	72 414 *359*	72 773 *356*	73 129 *350*	73 479	
[3/2]4d; 0	3.04	72 594 *-320*	72 914 *359*	73 273 *358*	73 631 *351*	73 982 *352*	74 334
[1/2]4d; 1	2.77		73 369 *358*	73 727 *368*	74 095 *324*	74 419	
[1/2]4d; 1	2.77	73 311 *-320*	73 631 *374*	74 005 *358*	74 363 *373*	74 736	
[1/2]4d; 2	2.98		75 295 *353*	75 648 *373*	76 021		
[1/2]4d; 0	3.03	75 346 *-319*	75 665 *356*	76 021 *353*	76 372 *347*	76 721 *348*	77 069
[3/2]5d; 2	4.02		78 043 *359*	78 402 *363*	78 765 *354*	79 119	
[3/2]5d; 0	4.09		78 257 *361*	78 618 *360*	78 978 *358*	79 336 *347*	79 683
[3/2]6d; 2	5.03		80 490 *360*	80 850 *362*	81 212		
[3/2]6d; 0	5.04		80 595 *363*	80 958 *361*	81 319		
[1/2]5d; 2	4.03		80 877 *361*	81 238 *357*	81 595 *372*	81 967	

Table 3.1: Wavenumber positions of Rydberg state vibronic levels in mass-resolved [2+1] REMPI spectrum of Br_2 run on $^{79}Br^+$ mass channel. The effective quantum number of each Rydberg state $(n-\delta)$ is given. Bottom (italics) entry corresponds to the wavenumber difference between adjacent vibrational levels of the Rydberg state. Hot bands (0,1) are denoted by a negative wavenumber difference from the (0,0) vibronic transition energy. Column headings correspond to vibronic transitions (v', v'').

Rydberg state	$(n - \delta)$	(0,1)	(0,0)	(1,0)	(2,0)	(3,0)	(4,0)
[1/2]5d; 0	4.07	80 707 *-327*	81 034 *361*	81 395 *374*	81 769 *360*	82 129	
[3/2]7d; 2	6.07		81 838 *365*	82 203 *354*	82 557 *346*	82 903	
[3/2]7d; 0	6.14		81 907 *365*	82 272 *357*	82 629		
[3/2]8d; 2	7.08		82 629 *357*	82 986			
[3/2]8d; 0	7.15		82 676 *355*	83 031 *342*	83 373		
[3/2]9d; 0	8.14		83 164 *364*	83 528			
[1/2]6d; 2	5.04		83 331 *369*	83 700			
[1/2]6d; 0	5.09		83 413 *367*	83 780			
[3/2]10d; 0	9.17		83 516 *372*	83 888 *362*	84 250		
[3/2]11d; 0	10.20		83 767 *365*	84 132			
[3/2]12d; 0	11.24		83 953				

Table 3.2: Wavenumber positions of Rydberg state vibronic levels in mass-resolved [2+1] REMPI spectrum of Br$_2$ recorded on the ^{79}Br$^+$ mass channel. The effective quantum number of each Rydberg state $(n - \delta)$ is given. Bottom (italics) entry corresponds to the wavenumber difference between adjacent vibrational levels of the Rydberg state. Hot bands (0,1) are denoted by a negative wavenumber difference from the (0,0) vibronic transition energy. Column headings correspond to vibronic transitions (v', v'').

ν_{obs} (cm^{-1})	ν_{lit} (cm^{-1})	ν_{obs}-ν_{lit} (cm^{-1})	Upper state term ($4s^24p^45p$)	Lower state term† ($4s^24p^5$)
72 012	72 012	0	$^4\mathrm{D}^0_{5/2}$	$^2\mathrm{P}^0_{1/2}$
78 083	78 076	+7	$^2\mathrm{D}^0_{3/2}$	$^2\mathrm{P}^0_{1/2}$
78 520	78 514	+6	$^4\mathrm{S}^0_{3/2}$	$^2\mathrm{P}^0_{1/2}$
75 000	75 009	-9	$^2\mathrm{P}^0_{3/2}$	$^2\mathrm{P}^0_{3/2}$
79 185	79 178	+7	$^4\mathrm{S}^0_{3/2}$	$^2\mathrm{P}^0_{3/2}$
75 820	75 814	+6	$^2\mathrm{P}^0_{1/2}$	$^2\mathrm{P}^0_{3/2}$
79 872	79 868	+4	$^2\mathrm{P}^0_{1/2}$	$^2\mathrm{P}^0_{3/2}$
76 738	76 743	-5	$^4\mathrm{D}^0_{3/2}$	$^2\mathrm{P}^0_{3/2}$
78 076	78 076	0	$^2\mathrm{S}^0_{1/2}$	$^2\mathrm{P}^0_{3/2}$
78 515	78 512	+3	$^2\mathrm{D}^0_{5/2}$	$^2\mathrm{P}^0_{3/2}$
78 681	78 677	+4	$^2\mathrm{D}^0_{3/2}$	$^2\mathrm{P}^0_{3/2}$
79 185	79 178	+7	$^4\mathrm{S}^0_{3/2}$	$^2\mathrm{P}^0_{3/2}$
79 693	79 696	-3	$^2\mathrm{P}^0_{3/2}$	$^2\mathrm{P}^0_{3/2}$
79 867	79 868	-1	$^2\mathrm{P}^0_{1/2}$	$^2\mathrm{P}^0_{3/2}$
87 061	87 061	0	$^2\mathrm{F}^0_{5/2}$	$^2\mathrm{P}^0_{1/2}$
87 511	87 499	+12	$^2\mathrm{P}^0_{1/2}$	$^2\mathrm{P}^0_{1/2}$

Table 3.3: Atomic bromine transitions observed in the [2+1] REMPI spectrum of jet-cooled Br_2, recorded on the $^{79}Br^+$ mass channel. † indicates the energy difference between the lower state components of the Br atom where $\Delta E(^2\mathrm{P}^0_{1/2}$-$^2\mathrm{P}^0_{3/2})$ =3 685 cm^{-1}.

bronic bands in three of the four progressions (with electronic origins at 72 416, 73 371 and 73 633 cm^{-1}) in the circular polarization spectrum are enhanced relative to those observed with linear polarization. However, the remaining progression, with an origin at 72 916 cm^{-1}, has almost no intensity under circular polarization conditions, whereas this is the most intense in the linear polarization spectrum.

This is explained by considering the expressions derived by Bray and Hochstrasser for rotational linestrengths for two-photon transitions[8]. They showed that, with one exception, rovibronic transitions from an Ω=0 state have a factor of 1.5 greater intensity, for all lines of all branches, in circular polarization spectra than those in linear polarization spectra. The exception is that the Q branch of a $0 \leftarrow 0$ transition can decrease by a variable amount under circular polarization conditions. It must be concluded that bands which show a reduction in intensity with circular polarization have an overall angular momentum, Ω=0.

This result represents a change in the previous assignment of the band at 72 916 cm^{-1}, given before[5,9] as [3/2]6s; 1. A reassignment of the Rydberg orbital must also be made since a [3/2]6s; 0 state can not exist by considering the orbital momenta of the core and the Rydberg electron under Ω_c-ω coupling. Hence, the Rydberg state is reassigned as [3/2]4d; 0. The $(n - \delta)$ value of 3.04 is slightly higher than that found for the 4d states in atomic bromine (2.60-2.86), but is reasonable when considering that the $(n - \delta)$ values for the 5s states of the molecule

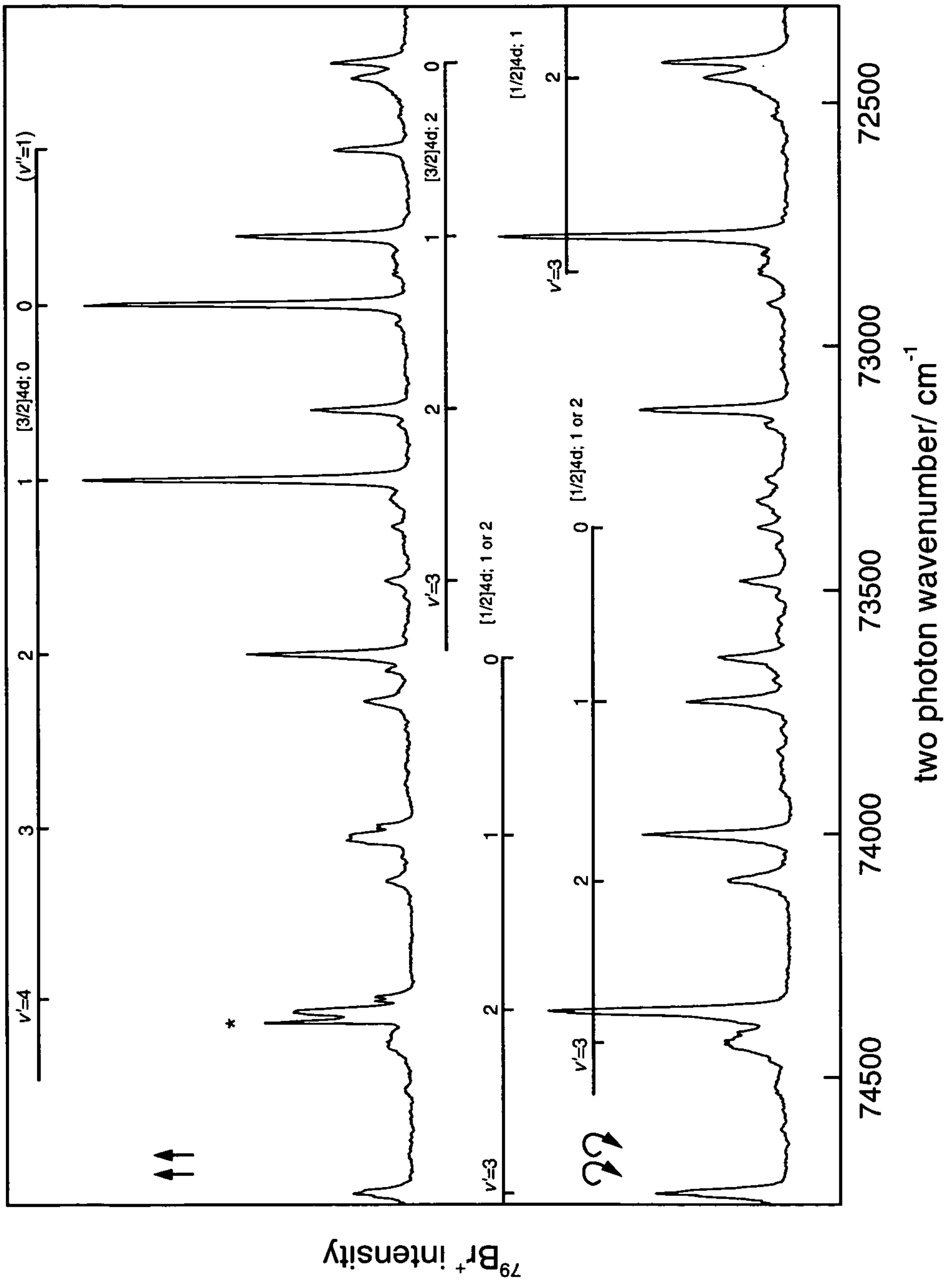

Figure 3.6: [2+1] REMPI spectrum of Br_2 between 72 000 and 75 000 cm^{-1}. The upper trace was recorded using circularly polarized light and the lower trace recorded using linearly polarized light. Both spectra were recorded on the $^{79}Br^+$ mass channel. Atomic tranistions are marked with an asterisk.

are also *ca.* 0.1 higher than those of the atom.

The polarization behaviour of states in the remainder of the spectrum between 77 00 and 85 000 cm^{-1} has been investigated and it is observed that states previously assigned as $[3/2]ns$; 1 show a decrease in intensity, characteristic of Ω=0 states, under circular polarization conditions. Hence higher members of the ns series with Ω=1 are now reassigned as (n-2)d; 0 states.

With this reassignment, it is proposed that the spectrum is dominated by higher members of the nd Rydberg series and that transitions to the ns series are weak relative to these. Furthermore, for a complete assignment of all Rydberg states in the spectrum, a method for determining the overall angular momentum, Ω is required. This was provided by obtaining rotational band contours experimentally, which, in conjunction with simulated rotational band contours allowed the Ω value of a vibronic band to be determined.

3.3.4 Rotational band contours: experimental and simulated

Ω=1 states

The (0,0), (1,0) and (2,0) bands of the two [3/2]4d; 1 states with origins at 68 827 and 70 571 cm^{-1} have been determined by Xu *et al.*[10] to be Ω=1 states by full rotational analysis of a sample of Br_2 at room temperature. The upper trace of figure 3.7(a) shows a slow scan of the origin of the first of these two states, obtained from a rotationally cooled sample of bromine with the ion signal collected on the $^{79}Br_2{}^+$ mass channel. This signal was therefore isotopically pure which allowed a computer simulation of the rotational contour to be generated, shown on the lower trace of figure 3.7(a). A dedicated program was used which operates on an input of upper and ground state rotational constants, an estimated rotational temperature and an estimated scanning source bandwidth. The linestrength expressions derived by Bray and Hochstrasser were then calculated using this data and the resultant rotational band contour is generated and output graphically. Accurately known rotational constants[10,11] $B_{v''}$=0.081 947 cm^{-1} and $B_{v'}$=0.088 93 cm^{-1} and an estimated rotational temperature of 20 K with a laser bandwidth of 0.8 cm^{-1} reproduced the experimentally obtained rotational contour and confirmed the assignment of Ω=1. The [1/2]4d; 1 states were assigned by considering their separation from the [3/2]4d; 1 states. The [3/2]5s; 1 state was observed at 56 544 cm^{-1} and confirmed by rotational analysis. The

[1/2]5s; 1 band was assigned based on the splitting energy between different cores.

Ω=2 states

A slow scan of the origin band at 72 416 cm^{-1} recorded on the $^{79}Br_2^+$ mass channel using linearly polarized light is shown in the upper trace of figure 3.7(b). The shape of the contour is evidently different from that of the Ω=1 band shown in figure 3.7(a). However, it is accurately reproduced by a simulation of Ω=2 linestrengths using the same rotational constants, temperature and bandwidth as for the rotational contour analysis of the Ω=1 band and is therefore assigned accordingly. This state was previously assigned[5,9] as an Ω=2 state but with the Rydberg electron in a 6s orbital, associated with the [3/2] core. On the basis of the polarization behaviour of the Ω=0 states throughout the entire spectrum and given that two Ω components of each Rydberg state, on each core, are observed then states previously assigned [3/2]*n*s; 2 are now reassigned with configuration [3/2](*n*-2)d; 2.

Ω=0 states

A slow scan of the [3/2]4d; 0 state vibronic origin at 72 916 cm−1 recorded on the $^{79}Br_2^+$ mass channel using linearly polarized light is shown on the upper trace of figure 3.7(c). The lower trace of figure 3.7(c) shows a simulation of $\Delta\Omega$=0 rotational linestrengths using the same constants and rotational temperature as the previous simulation and further confirms the Ω=0 assignment. The contour shows a dominant Q branch at least one order of magnitude of intensity greater than the O and S branches, the P and R branches being forbidden.

The [1/2]5s; 0 state

The [2+1] REMPI spectrum of jet-cooled $^{79}Br_2$ between 57 500 and 59 700 cm^{-1}, collected on the $^{79}Br^+$ mass channel using circularly polarized light (upper trace) and linearly polarized light (lower trace) is shown in figure 3.8. The vibronic bands of three states have been identified in this region, *viz.* [3/2]5s; 1, [1/2]5s; 0 and [1/2]5s; 1 as shown on the spectrum. Contrary to the general reassignment of the spectrum to higher energy, these states remain assigned as *n*s states in order to be consistent with quantum defect values[12].

An anomalous result is presented in these spectra: the [1/2]5s; 0 progression shows no observable decrease in intensity with circularly polarized light. A slow scan of the band origin using linearly polarized light is shown in the upper trace of figure 3.7(d). It can be seen that the contour is very different to that of the [3/2]4d; 0 band origin shown in figure 3.7(c) where a very strong Q branch dominates the band contour. Furthermore, the contour appears the same with both linearly and circularly polarized light. The contour of the [1/2]5s; 0 band was

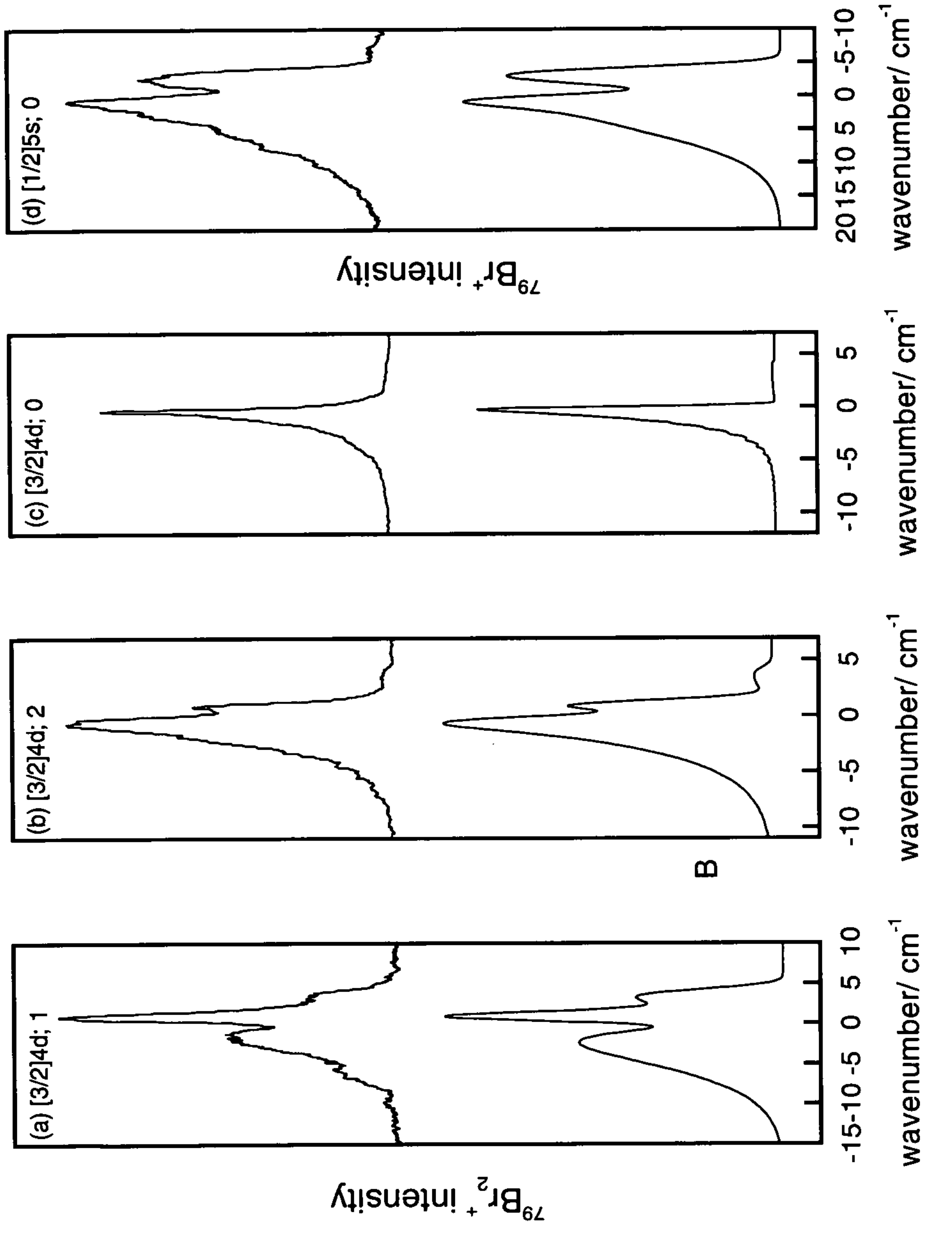

Figure 3.7: Observed (upper trace) and simulated (lower trace) rotational contours of the (a) [3/2]4d; 1, (b) [3/2]4d; 2, (c) [3/2]4d; 0 and (d) [1/2]5s; 0 Rydberg state origins.

simulated accurately by varying the ratio of the transition dipole factors μ_I^2/μ_S^2 (see p.115 for a full description of these terms) which are dependent upon the individual one-photon transition moments in the two-photon excitation pathway, under conditions of linearly and circularly polarized light. Further explanation of this observation in terms of the polarization behaviour and mechanism of the two-photon transition will be given in the discussion section (3.4.3).

3.3.5 Rydberg/ion-pair interactions

Coherent excitation *via* the numerous Rydberg systems observed in the spectral range covered appears to be very efficient. However, account must be taken of interactions, at the two-photon level, of Rydberg states with other states in the same region. There is evidence of two bands in the spectrum interacting with a close-lying, bound ion-pair state, by vibronic coupling. In the spectrum recorded on the atomic mass channel, the (3,0) band of the lowest [3/2]4d; 1 state (at 69 902 cm^{-1}) and the (2,0) band of the lowest energy [1/2]4d; 1 state at (72 449 cm^{-1}) are broadened to both the blue and red (also observed in I_2 [13]).

Red degradation of the rotational contours of bands arises whenever $B_{v'}<B_{v''}$, i.e. rotational constants for vibrational levels in the upper state are smaller than in the lower (ground) state. The upper (Rydberg) state adopts properties of

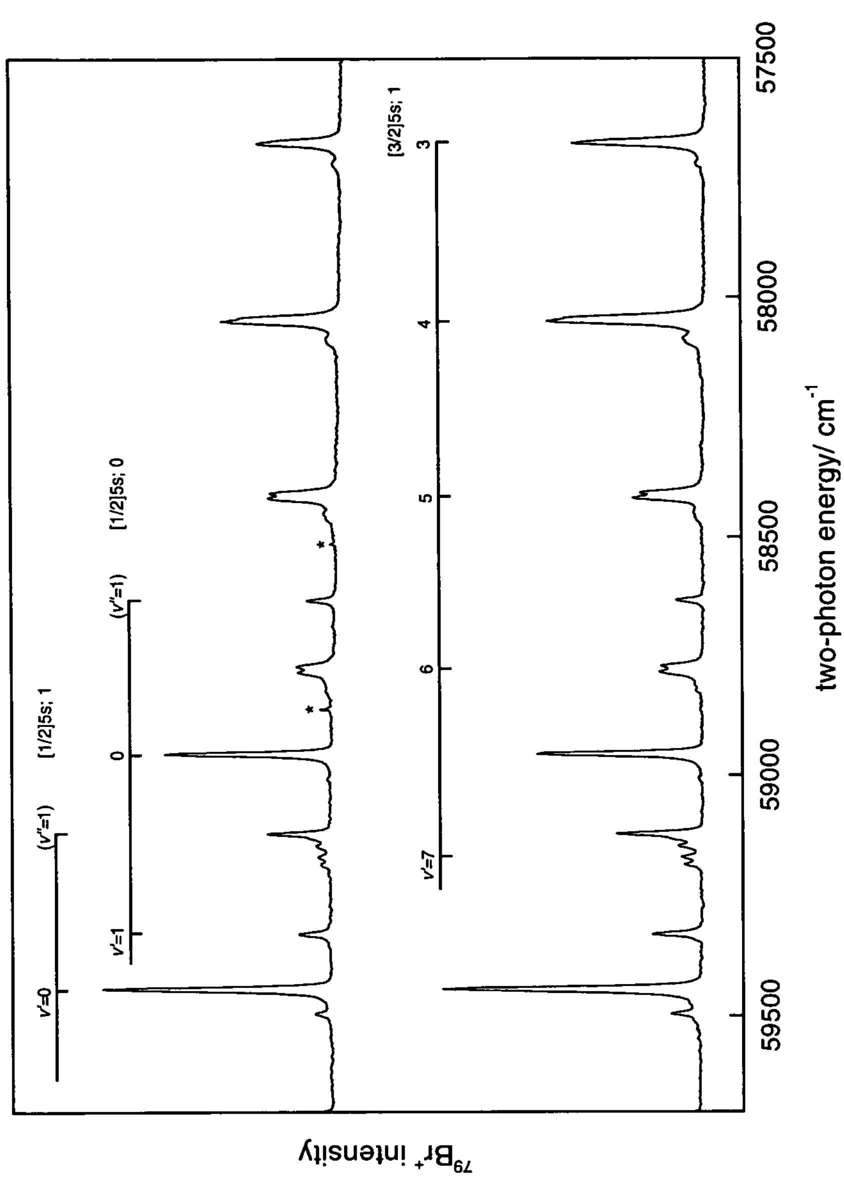

Figure 3.8: [2+1] REMPI spectrum of Br_2 between 57 000 and 60 000 cm^{-1}. The upper trace was recorded using circularly polarized light and the lower trace recorded using linearly polarized light. Both spectra were recorded on the $^{79}Br^+$ mass channel. Atomic lines are marked with an asterisk (*).

the interacting (ion-pair) state, which has inherently low rotational constants by virtue of the bond extension, through vibronic coupling and hence the rotational manifolds of each state mix. The Rydberg state has a greater rotational constant than the ground state and so bands, which are not subject to vibronic coupling to neighbouring ion-pair states, have rotational contours which are broadened to the blue.

3.4 Discussion

With the reassignment of the Rydberg series in the [2+1] REMPI spectrum of bromine of ns states with nd states, it is surprising that only two Ω components, with a few exceptions, of the d-series dominate when many more components are available than in the ns counterpart. This can be explained by careful consideration of the electronic structure of the different Ω components of the d-series, given below. To summarise briefly, a propensity for transitions to states with only a large singlet component exists and only two strongly allowed two-photon transitions for each $[\Omega_c]n$d, together with two weaker ones, are therefore predicted. This provides a sound theoretical reasoning, in complement to the experimental evidence, for invoking a d-series rather than an s-series which should only exhibit one strongly allowed transition for each component of an $[\Omega_c]n$s state.

Ω_c	Ω	$^{2S+1}\Lambda$	micronfiguration $[\pi_g^3]_c(\lambda m_s)_R y$
3/2	2	$^{1,3}\Delta$	$[1^+1^-\underline{1}^+]_c1^-$
...	1	$^{1,3}\Pi$	$[1^+1^-\underline{1}^+]_c0^-$
...	1	$^{1,3}\Pi$	$[1^-\underline{1}^+\underline{1}^-]_c2^+$
...	$0^\pm$	$^{1,3}\Sigma^\pm$	$2^{-1/2}([1^+1^-\underline{1}^+]_c\underline{1}^-\pm [\underline{1}^-\underline{1}^+1^-]_c1^+)$
...	2	$^3\Pi$	$[1^+1^-\underline{1}^+]_c0^+$
...	1	$^3\Sigma$	$[1^+1^-\underline{1}^+]_c\underline{1}^+$
...	$0^\pm$	$^3\Pi$	$2^{-1/2}([1^+1^-\underline{1}^+]_c\underline{2}^+\pm [\underline{1}^-\underline{1}^+1^-]_c2^-)$
1/2	2	$^{1,3}\Delta$	$[1^+1^-\underline{1}^-]_c1^+$
...	1	$^{1,3}\Pi$	$[1^+1^-\underline{1}^-]_c0^+$
...	1	$^{1,3}\Pi$	$[1^-\underline{1}^+\underline{1}^-]_c2^-$
...	$0^\pm$	$^{1,3}\Sigma^\pm$	$2^{-1/2}([1^+1^-\underline{1}^-]_c\underline{1}^+\pm [\underline{1}^-\underline{1}^+1^+]_c1^-)$
...	2	$^3\Phi$	$[1^+1^-\underline{1}^-]_c2^-$
...	2	$^3\Pi$	$[1^+\underline{1}^+\underline{1}^-]_c2^+$
...	1	$^3\Delta$	$[1^+1^-\underline{1}^-]_c1^-$
...	1	$^3\Sigma$	$[1^+\underline{1}^+\underline{1}^-]_c1^+$
...	$0^\pm$	$^3\Pi$	$2^{-1/2}([1^+1^-\underline{1}^-]_c0^-\pm [\underline{1}^-\underline{1}^+1^+]_c0^+)$

Table 3.4: The configurations in the $\Omega_c\lambda m_s$ coupling scheme of all the states of an nd cluster of Rydberg states in a homonuclear diatomic halogen molecule, for $\Omega \leq 2$.

3.4.1 Electronic structure of the Ω components of the d-series

As mentioned above, several sub-levels of each $[\Omega_c]n$d Rydberg state are accessible in coherent two-photon excitation, in the limit of the Hund's case (c) coupling scheme, i.e. those with $\Omega \leq 2$. Table 3.4 lists all of those states which are, in principle, accessible by two-photon excitation[14]. The rightmost column in the table shows the microconfigurations of the d-states, using the convention that the digits indicate the m_l value of the orbital occupied by an electron, underlined digits represent a negative m_l value and the superscripts represent the spin of the electron; $+\equiv \alpha$ (up) and $-\equiv \beta$ (down). The microconfiguration of the ionic core,

Ω_c=3/2 or 1/2, is enclosed in square brackets and that of the Rydberg electron given outside the brackets. From the table, a total of seven sub-levels of each [3/2]nd state and nine of [1/2]nd meet the condition for $\Omega \leq 2$. However, only four Ω states on each core have some singlet character, with the remainder being purely triplet, in agreement with the assignments made in this work, where two components are seen strongly for $n \geq 4$ and two weakly for n=4, on each core.

3.4.2 Two-photon Honl-London factors for rotational transitions

The rotational linestrengths for the Q-branch of a two-photon Ω=0→0 transition, under circularly and linearly polarized conditions, are given by equations (3.1) and (3.2).

Circular polarization:

$$\frac{(2J+1)[J(J+1)]}{30(2J+3)(2J-1)}\mu_S^2 \tag{3.1}$$

Linear polarization:

$$\frac{(2J+1)}{9}\mu_I^2 + \frac{(2J+1)[J(J+1)]}{45(2J+3)(2J-1)}\mu_S^2 \tag{3.2}$$

where

$$\mu_S^2 = \mid 2\mu_{\parallel}\mu_{\parallel}^{'} - \mu_{+}\mu_{-}^{'} \mid^2; \qquad \mu_I^2 = \mid \mu_{\parallel}\mu_{\parallel}^{'} + \mu_{+}\mu_{-}^{'} \mid^2 \tag{3.3}$$

Equation (3.3) describes the transition dipole factors, μ_S^2 and μ_I^2, in terms of one-photon transition moments $\mu_{\|}$ and $\mu_{\pm}$, corresponding to parallel and perpendicular transitions, from an Ω=0 ground electronic state, respectively.

It is clear, from the linestrength expressions given in equations (3.1) and (3.2), that the Q-branch intensities for Ω=0→0 transitions can decrease by a variable amount under circular polarization conditions, depending on the ratio of μ_I^2:μ_S^2. Since these terms depend on the individual one-photon transition moments in the two-photon pathway, the nature of the relevant intermediate states can be probed.

The polarization ratio (σ_{ll}/σ_{cc}) can be expressed in terms of the ratio of transition dipole factors (μ_I^2/μ_S^2). Two limiting cases of the polarization ratio exist if the intermediate state which dominates is a single virtual (or resonant continuum) state; either the excitation is *via* two parallel transitions ($\mu_{\|}$) or two perpendicular transitions ($\mu_{\pm}$). In the former case, the limiting value of the polarization ratio in the limit of high J is 1/4. For two purely perpendicular transitions, the polarization ratio tends to a value of 1/14.

The rotational band contour simulations for the [3/2]4dπ; 0 and [1/2]5s; 0 states are shown on figures 3.7(c) and 3.7(d) respectively. It is seen that the two contours differ markedly with the former exhibiting a dominant Q-branch, at least one order of magnitude greater than the O- and S-branches and the latter with negligible Q-branch intensity but with distinct O- and S-branches. Evidently, a different excitation mechanism is operating in each case which is determined by the nature of the virtual intermediate at the one-photon level of the overall $\Omega=0\rightarrow0$ transition.

3.4.3 Virtual intermediate states in $\Omega=0\rightarrow0$ transitions

Two distinct cases are presented from the polarization studies, which infer two separate excitation pathways *via* distinct intermediate states. Possible routes to the [3/2]4dπ; 0 and [1/2]5s; 0 Rydberg states are discussed below.

The [3/2]4dπ; 0 Rydberg state

Two-photon transitions to the [3/2]4dπ; 0 Rydberg state can occur *via* two competing pathways at the one-photon level. One intermediate state may be partially resonant, lying just in the wings of the C←X absorption band, although this would involve two perpendicular transitions to the Rydberg state. The C 1_u valence state is designated a singlet state which may assist in transitions to the singlet d Rydberg states, however a change in total angular momentum is required in accessing this state from the ground state X($\Omega=0$) and subsequent excitation to the $[\Omega_c]$d$\pi(\Omega=0)$ Rydberg states. An alternative route, involving parallel transitions, may be found in invoking a virtual Rydberg state as a suitable intermediate, represented by $[\sigma_g^2\pi_u^3\pi_g^4]d\pi$ $^1\Sigma_{0u}^+$, i.e. a d-Rydberg state coupled to an *ungerade* core. This implies a very nonresonant step which is compensated to some extent by the strong nature of two parallel transitions.

The absence of the Q-branch of Ω=0 d-Rydberg states under circular polarization conditions may be explained by making μ_S very small (such that $\mu_S^2/\mu_I^2<0.01$) which indicates that in each of the two-photon transition steps outlined above, the transition moments have similar amplitudes and destructively interfere in the μ_S term in equation (3.3).

The [1/2]5s; 0 Rydberg state

The rotational band contour of the [1/2]5s; 0 Rydberg state origin at 58 940 cm^{-1}, using linearly polarized light, seen on figure 3.7(d) is very different from that of the [1/2]4d; 0 state (figure 3.7(c)). This indicates a very different excitation route for the s-states whereby either the two-photon transition dipole moments are differently phased from those used to reach the Ω=0 d-states or the pathway is *via* a different virtual state.

It has been experimentally observed that the polarization ratio, σ_{cc}/σ_{ll} (i.e. ratio of Q-branch intensities under circular and linear polarization), is around 3/2 which indicates that μ_I^2 is negligible relative to μ_S^2, according to equations (3.2) and (3.3). This accounts for the similar appearance of the band contours under both circular and linear polarization and the absence of a strong Q-branch in each case.

The [1/2]5s; 0 state has been assigned a triplet configuration which suggests that the $B(^3\Pi_0^+)\leftarrow X$ transition is important in the two-photon excitation pathway at the one-photon level if parallel transitions between states of same multiplicity are favoured.

3.4.4 [2+1] REMPI spectra of I_2 and Cl_2

In light of the reassignment of the *gerade* Rydberg states of Br_2 presented here, a similar treatment should be applied to the other homonuclear halogens, I_2 and Cl_2, given the similarities in the electronic structure and in the REMPI spectra. It has been shown that the same overall pattern of Rydberg states exists for these molecules, i.e. two Ω components of each Rydberg state on each spin-orbit component of the ionic core are seen strongly. Those states previously assigned as ns-states, with the exception of the lowest-lying members of the s-series in each molecule (6s and 4s in I_2 and Cl_2 respectively), should now be reassigned as (n-2)d-states. Band contour analysis of the 7s/5d states of iodine by Kvaran lends further support to this reassignment[15].

3.5 Conclusions

The [2+1] REMPI spectrum of jet-cooled Br_2 in the region 56 000-86 000 cm^{-1} has been recorded and significantly reassigned to series of Rydberg d-states, as a consequence of polarization studies and rotational band contour analysis. Despite several Ω components available for d-states on either ionic core ([3/2] or [1/2]), only a restricted number are accessible with the $\Omega=2$ and $\Omega=0$ observed most strongly. It was proposed that only four states that have partial singlet character are accessed at the two-photon level. The two $\Omega=1\leftarrow X$ components on each core state are seen weakly only for $n=4$ and this is attributed in part to selective mixing with neighbouring ion-pair states and possibly predissociation. Rotational band contour analysis and simulation was used to determine the Ω value of the $\Omega=0$, 1 and 2 components of the 4d Rydberg state.

The $\Omega=0$ states were further assigned as such by their almost complete disappearance under circular polarization conditions. This behaviour was rationalised in terms of competing processes in the two-photon transition pathway and the nature of the intermediate states at the one-photon level. At lower energy, the [1/2]5s Rydberg states were not reassigned, to remain consistent with quantum defects values.

With the aid of polarization studies, jet-cooling and rotational band contour analyses and simulations, this significant reassignment of the two-photon spectrum of Br$_2$ has also prompted the same in I$_2$ and Cl$_2$, given the similarities in electronic structure and the appearance of the REMPI spectrum.

3.6 References

[1] P. Venkateswarlu, *Can. J. Phys.* **47** (1969) 2525

[2] A.J. Yencha, D.K. Kela, R.J. Donovan, A. Hopkirk and A. Kvaran, *Chem. Phys. Lett.* **165** (1990) 283

[3] J.B. Nee, *J. Chem. Phys.* **97** (1992) 2982

[4] D.I. Austin, R.J. Donovan, A. Hopkirk, K.P. Lawley, D. Shaw and A.J. Yencha, *Chem. Phys.* **118** (1987) 91

[5] T. Ridley, K.P. Lawley, R.J. Donovan and A.J. Yencha, *Chem. Phys.* **148** (1990) 315

[6] J.L. Tech, *J. Res. Nat. Bur. Stand.-A* **67A** (1963) 505

[7] D.A. Beattie, M.C.R. Cockett, K.P. Lawley and R.J. Donovan, *accepted for J. Chem. Soc. Farad. Trans.* (1997)

[8] R.G. Bray and R.M. Hochstrasser, *Mol. Phys.* **31** (1976) 1199

[9] B.G. Koenders, G.J. Kuik, K.E. Drabe and C.A. DeLange, *Chem. Phys. Lett.* **147** (1988) 310

[10] L. Xu, Y. Wang, P. Wang and F. Li, *J. Chem. Phys.* **101** (1994) 3542

[11] R.F. Barrow, T.C. Clark, J.A. Coxon and K.K. Yee, *J. Mol. Spec.* **51** (1974) 428

[12] K.P. Lawley, R.J. Donovan, T. Ridley, A.J. Yencha and T. Ichimura, *Chem. Phys. Lett.* **168** (1990) 168

[13] K.P. Lawley, T. Ridley, Z. Min, P.J. Wilson, M.S.N. Al-Kahali and R.J. Donovan, *Chem. Phys.* **197** (1995) 37

[14] R.J. Donovan, A.C. Flexen, K.P. Lawley and T. Ridley, *Chem. Phys.* **226** (1998) 217

[15] A. Kvaran, *private communication*

Chapter 4

Ion-Pair Formation from I_2 Using VUV Laser Radiation

4.1 Introduction

This chapter describes ion-pair formation from I_2, in the range 71 000-75 000 cm^{-1}, observed for the first time using a VUV laser source. Ion-pair formation was deduced by comparing spectra recorded as a function of I^+ and I^- ion signals, which were found to be equivalent over the entire range. The free ion formation spectrum reproduced the high resolution absorption spectrum[1] which had previously been assigned to several series of Rydberg states. Hence, ion-pair formation is described here in terms of predissociating Rydberg states lying above the first ion-pair threshold. Ion-pair formation from I_2 has also been observed under low resolution conditions, using a synchrotron source[2]. This spectrum is surprisingly simple in structure compared to the present spectrum and the results from each study are compared here. The low resolution, synchrotron study describes a selective predissociation mechanism involving just three members of the $[3/2]_c n\text{p}\pi$ Rydberg series and the $D0_u^+$ ion-pair state. It will be shown in this chapter that all Rydberg states accessed by one-photon excitation in the region covered undergo predissociation. The mechansim is interpreted in terms of two-electron exchange connecting the configurations of the Rydberg and relevant ion-pair states. The one-photon absorption spectrum is largely reassigned here by taking into account the propensity rules derived from the reassignment of the two-photon spectrum of Br_2 and using accurate data, obtained from a ZEKE experiment for the lowest IP of I_2.

4.1.1 Background to the spectroscopy of I_2

Diatomic iodine, I_2, has been one of the molecules most extensively studied by spectroscopic techniques. Mulliken[3] formulated the basis for interpretation of halogen molecular spectra in 1934. This was followed by a number of re-evaluations by Mulliken[4] himself and others including Wieland[5] and Venkateswarlu[6]. However, according to Mathieson and Rees' 1956 paper on the electronic states and potential energy diagram of the iodine molecule[7], further reinterpretation was required, given the contradictory statements made by Venkateswarlu previously. This work was successful to a certain extent, accurately predicting the lower *ungerade* valence states (e.g. A, B and C) but failed to correctly assign the configurations of the *ungerade* ion-pair states (i.e. D, F, G and H). This reflected the emphasis of experimental work on I_2 to that date being concentrated towards the visible and ultraviolet regions of the spectrum (e.g. Mulliken[4] (1940)), with somewhat less reported on one-photon excitation into the VUV regions of the molecule (e.g. Cordes[8] (1935)).

With the publication of Mulliken's "Iodine Revisited"[9] in 1971, essentially summarising experimental results from several sources, a more complete and consistent model of the configurations of the valence states (including the ion-pair states) of iodine was formulated. In particular, the D←X band system, which constitutes a vertical transition in the far-UV or VUV wavelength range to bound levels of one of the lowest lying ion-pair states D(0_u^+) had been studied in some detail, both in absorption and emission. Several vibrational levels are accessible by direct transition from the ground state, being within the Franck-Condon window bounded by the vibrational amplitude of the v''=0 level of the ground state.

With the ability to experimentally observe regions of the molecule lying in the VUV frequency range by fluorescence emission using electrical discharge or excited line sources, or absorption using continuum sources, attempts were made to study the Rydberg states by these techniques. One of the most extensive treatments of the Rydberg systems of the molecule, between *ca.* 56 000 cm^{-1} and the first ionization limit at around 75 000 cm^{-1} has been given by Venkateswarlu[1]. He used a Lyman flash lamp as a continuum source of VUV, with a 10.7 m spectrometer to record the absorption spectrum at high resolution (±0.5 cm^{-1} for sharp heads to ±2 cm^{-1} for diffuse bands). Using a photographed spectrum, he was able to identify and assign several overall *ungerade* Rydberg series of states with associated vibrational structure but without rotational resolution. Significantly, no analysis of the ion-pair systems present or Rydberg/ion-pair interactions occurring in this region of the spectrum was made, presumably because the spectrum was too congested to do so.

However, due to the recorded spectrum being very congested around the ionization limit (I_2^+, $^2\Pi_{3/2g}$), an ionization potential (I.P.) was determined which was 745 cm^{-1} higher than the currently accepted value of the $[3/2]_g$ ionic state of iodine, determined accurately by ZEKE spectroscopy[10] to be 75 069 cm^{-1}. Hence, after application of the Rydberg equation to Rydberg state term values, especially those with energies approaching the I.P. of the molecule, quantum defect values for the Rydberg states assigned by Venkateswarlu are quite inconsistent with quantum defect values derived for Rydberg states assigned in the work presented in this chapter. The results will be discussed and compared with those of Venkateswarlu in a later section.

Many of the Rydberg states in iodine are found to lie above the thermochemical threshold for ion-pair formation. This opens a pathway for predissociation of bound states (predominantly Rydberg) into the ion-pair continuum to produce oppositely charged ionic fragments I^+ and I^-. Single photon ion-pair formation from I_2 has previously been studied at low resolution by Morrison *et al.*[11] with only an excitation function for I^+. Myer and Samson[12] recorded the one-photon absorption spectrum between 1050 and 2200 Å by conventional photoelectron spectroscopy, with the intrinsic low-resolution associated with that. No detailed discussion was given to the Rydberg systems observed. Akopyan et al.[13] observed both I^+ and I^- formation in the region 1000-1400 Å again at low-resolution with no vibrational structure observed.

In 1985, Donovan *et al.*[14] repeated Venkateswarlu's VUV absorption experiment using a synchrotron source. As an extension to previous work the fluorescence excitation spectrum, detecting fluorescence wavelengths >1800 Å, was also recorded. Fluorescence from the ion-pair states of I_2 was readily detected.

In the most recent study, Kvaran et al.[2] used a synchrotron source at VUV wavelengths in the region 120-140 nm to study ion pair formation, also at low resolution ($\delta\nu \approx 50$ cm^{-1}), with time-of-flight mass spectroscopy, collecting positively and negatively charged atomic iodine ion fragments. They reported a surprisingly simple spectrum, given the high density of states expected in this region, involving just three Rydberg states with associated vibrational structure. The proposed mechanism for ion pair formation was described in terms of predissociation of these Rydberg states by the repulsive limb of the $D(0_u^+)$ ion-pair state. This was the same mechanism as suggested for ion-pair formation from Br_2, studied using the same experimental method[15]. Inclusion of the $D(0_u^+)$ state in the analysis was deemed the most suitable ion-pair state for interaction with $np\pi$ Rydberg states, observed in both I_2 and Br_2, in terms of the radiative and nonradiative transitions involved. This will be discussed later.

With the development of moderate power lasers, multiphoton ionization spectroscopy has become a useful technique for accessing high-lying states with two or more UV/visible photons. One of the first applications of [2+1] REMPI spectroscopy was to probe the *gerade* Rydberg states of molecular iodine carried out by Dalby et al.[16a] followed by Lehmann et al.[16b]. The high symmetry of iodine precludes the study of *ungerade* Rydberg states by [2+1] REMPI techniques, although [3+1] resonant ionization, as a route to *ungerade* Rydberg states, has been performed[17] using laser-based apparatus.

With the progress in [2+1] REMPI work on iodine, studied extensively in this group, together with the advantages afforded by the use of lasers, much has been learned not only about the *gerade* Rydberg systems in the molecule but the way in which they interact with neighbouring electronic states[18], in particular the ion-pair states. Now, with the development of a laser system which may access the *ungerade* Rydberg states of the molecule with a single VUV photon, a valuable complement to the previous work has been established, with the aim of determining the various electronic processes occuring at the one-photon level.

4.2 Experimental

VUV laser radiation was generated using RDFM in krypton gas, as described in chapter 2, section 2.3. VUV frequencies in the wavenumber range 71 000-75 000 cm^{-1} were generated using the two-photon resonant states $5p[\frac{1}{2}]_0$ and $5p[\frac{3}{2}]_2$, in krypton, at 94 094 and 93 123 cm^{-1} respectively and the fundamental output of the dyes Coumarin 307 and Coumarin 2.

A heated pulsed valve (General Valve) was used in this experiment to deliver pulses of jet-cooled I_2, seeded in He carrier gas at *ca.* 0.5 atm, to the VUV laser focus. The iodine sample was deposited in the gas delivery line by continual heating of the sample cell followed by heating in stages along the gas line close to the nozzle. In this way iodine was successively sublimed and condensed throughout the line and valve assembly. During experiments, the pulsed valve was heated to between 50 and 90 ^oC to ensure a high vapour pressure of iodine seeded into the He carrier gas.

4.3 Results

4.3.1 General features

The one-photon excitation spectrum of I_2 has been recorded between the first ion pair threshold (corresponding to dissociation products; $I^+(^3P_2)$ + $I^-(^1S_0)$) and the first ionization limit (I_2^+, $^2\Pi_{3/2}$), covering the wavenumber range 71 000-75 000 cm^{-1}. Using time-of-flight mass-spectrometry, spectra of ion signals due to I^+ and I^- were obtained. The spectrum shown in the upper trace of figure 4.1 was recorded by collecting I^+ ions and the lower trace collecting I^- ions. Comparison of the two excitation functions showed that each band observed in the I^- spectrum was seen at the equivalent wavenumber position in the I^+ spectrum and hence must be produced by the same mechanism. Furthermore, all structure in the ion excitation functions only appears above a certain frequency. It is concluded that Rydberg states in this region are being efficiently predissociated by suitable ion-pair states into separated ion pair fragments and that only Rydberg states lying above the (first) ion-pair threshold, within the ion-pair continuum are observed. The thermochemical ion-pair threshold has been determined accurately using the relevant thermodynamic properties reported in the literature: ionization potential[19] I.P.(I)=84 295.1±0.5 cm^{-1}, electron affinity[20], E.A.(I)=24

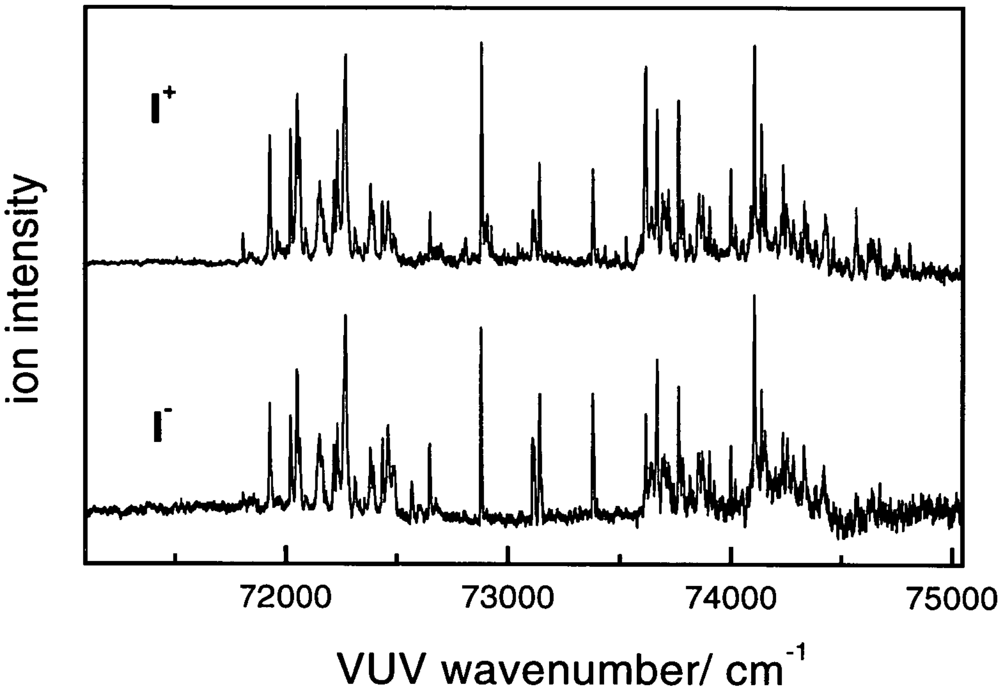

Figure 4.1: VUV free ion-pair formation spectrum of I_2 between 71 000 and 75 000 cm^{-1}, recorded on the I^+ mass channel (upper trace) and the I^- mass channel (lower trace).

673.0±0.5 cm^{-1} and ground state dissociation energy[21], $D_0(I_2)$=12 440.2±1.0 cm^{-1} to give a transition frequency from $v''=0$ to the threshold of 72 062.3±2.0 cm^{-1}.

Ion-pair formation from I_2 has previously been studied at low resolution by Kvaran *et al*[2], using synchrotron radiation. In that study, equivalent excitation functions for I^+ and I^- were observed indicating ion-pair formation. The recorded spectra were very simple in structure compared to the present spectrum, which effectively reproduces the high-resolution one-photon absorption spectrum. The results from the synchrotron experiment were interpreted in terms of a selective predissociation mechanism involving only three Rydberg states with associated vibrational structure belonging to the same series; $[3/2]_g n\mathrm{p}\pi$, n=9, 10 and 11 interacting with the $\mathrm{D}0_u^+$ ion-pair state above the first ion-pair threshold to produce unbound ion-pairs. The mechanism was discussed in terms of a homogeneous coupling between the ion-pair and Rydberg states, involving two parallel electron transitions ($\sigma \rightarrow \sigma^*$) and ($\pi \rightarrow \pi^*$) connecting the configurations D[1441] and [2430]π.

Hence, it has been shown that the present method of detecting ion-pair formation from I_2, using a high-resolution VUV laser source, reveals far more structure than previously obtained at low-resolution. It is clear that the predissociation mechanism previously suggested must be modified to include all accessible Rydberg states since ion-pair formation is observed from all states seen in the absorption spectrum. This is discussed in detail in section 4.4.4 of this chapter.

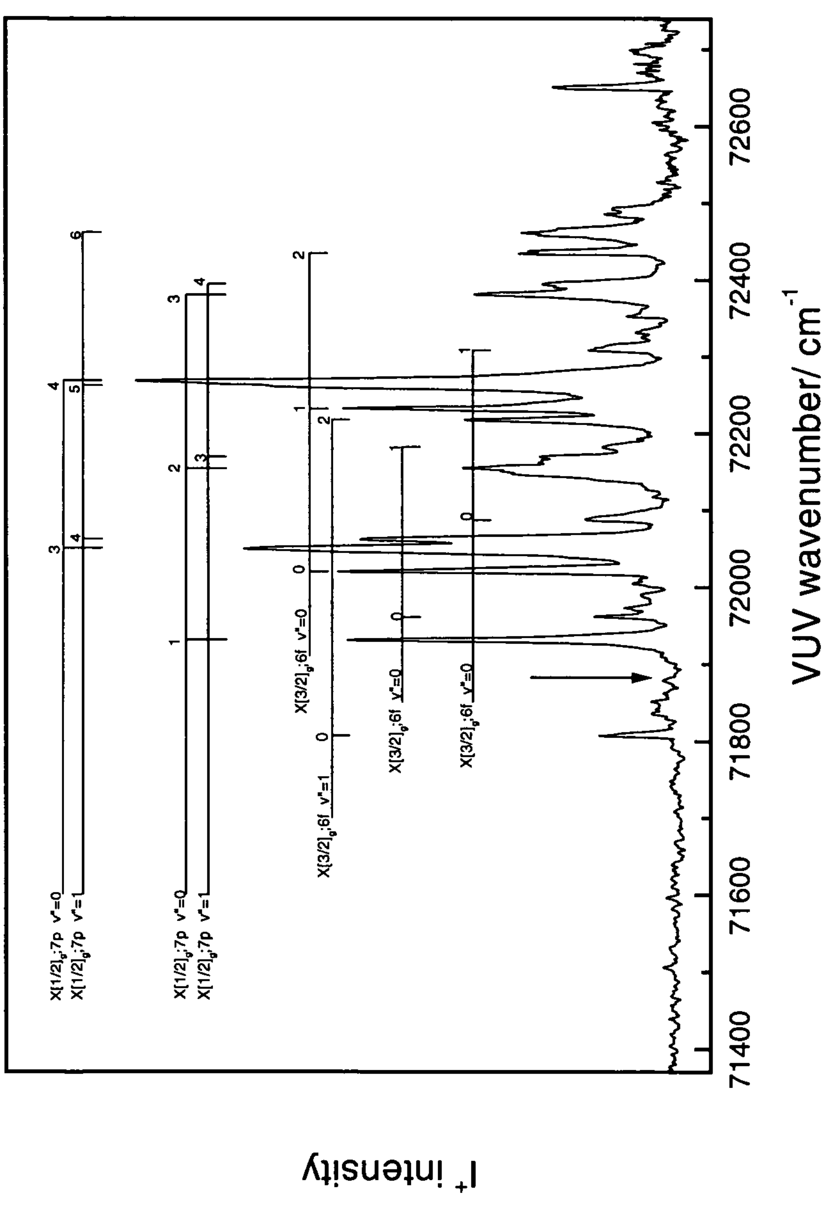

Figure 4.2: VUV free ion-pair formation spectrum of I_2 between 71 400 and 72 700 cm^{-1}. The arrow indicates the field-lowered ion-pair threshold corresponding to dissociation products $I^+(^3P_2)$+ $I^-(^1S_0)$, lying at 71 869 cm^{-1}.

Figures 4.2-4.4 show the spectrum recorded by collecting I^+ ions with assignments for nine Rydberg states and associated vibronic structure labelled on the figures. The main features of the spectrum are several strong, sharp Rydberg transitions, to np and nf states exhibiting fairly extensive vibronic structure with up to six vibrational quanta in a progression. Wavenumber positions of all Rydberg state origins and cold band vibronic transitions assigned are presented in table 4.1, with the hot band vibronic transitions in table 4.2. Extensive hot band structure, observed in the spectra, was attributed to heating the sample in order to improve the ion signal in the experiment. Wavenumber separations between vibrational progression members lie in the range 193-243 cm^{-1}, consistent with Rydberg states of I_2. Justification for the assignments, from the available experimental data, is presented in the following section.

The spectra shown in figures 4.2, 4.3 and 4.4 are composed of several shorter scans, where the VUV frequency range is generated from a combination of the two-photon resonance frequency in krypton and the frequency range of the particular dye used in the visible laser. Hence, variations in the VUV output power over the whole spectral range covered made obtaining reliable intensity information impracticable. Furthermore, owing to nonlinearity and saturation in the response of the photomultplier tube used to detect VUV throughput, it was not possible to produce power normalised spectra.

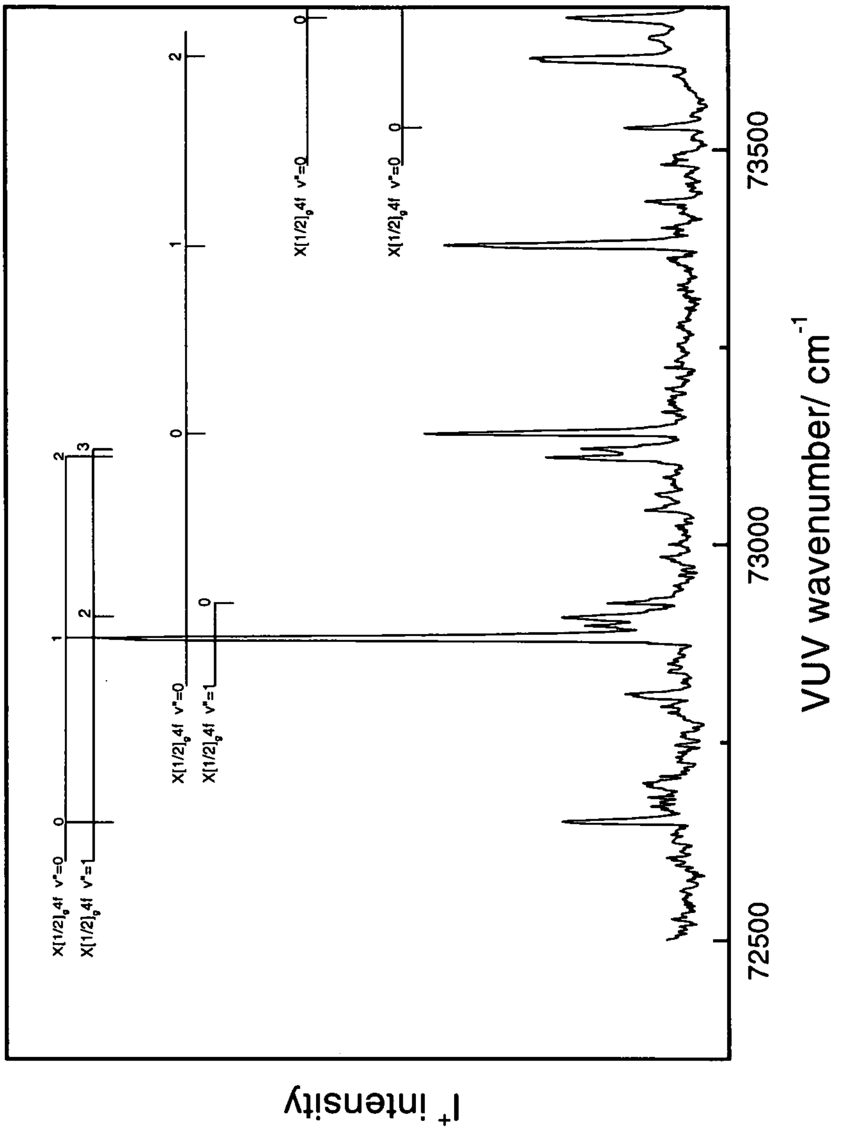

Figure 4.3: VUV free ion-pair formation spectrum of I_2 between 72 500 and 73 600 cm^{-1}.

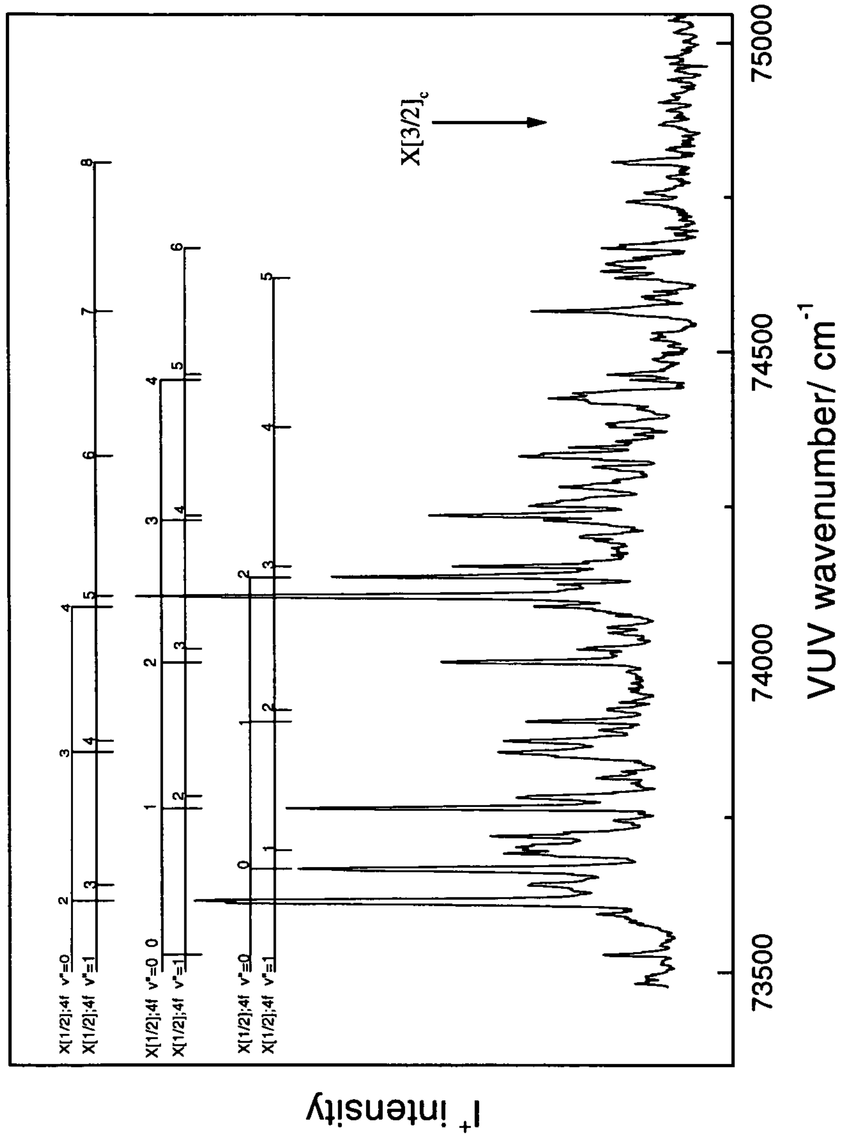

Figure 4.4: VUV free ion-pair formation spectrum of I_2 between 73 500 and 75 000 cm^{-1}. The arrow indicates the field-lowered ionization potential, lying at 74 870 cm^{-1}.

The ion-pair formation process appears to be very efficient given the extent of predissociation. This may account for the fact that fluorescence quantum yields in this region of the spectrum are very low [14]. Furthermore, the process must be occuring over a relatively large timescale, given the sharpness of the bands observed in the spectrum. Linewidths measured are of the order 3-10 cm^{-1}, which suggests that predissociation is occuring on a timescale of *ca.* 1-4 ps, significantly greater than a single vibrational period (*ca.* 20 fs).

Rydberg state	ν_{00}/ cm^{-1}	(1,0)	(2,0)	(3,0)	(4,0)
[1/2]7p; 0	(71 350)			72 052	72 276 *224*
[1/2]7p; 1	(71 705)	71 930	72 157 *227*	72 380 *223*	
[3/2]6f	71 955	72 180 *255*			
[3/2]6f	72 018	72 233 *215*	72 434 *201*		
[3/2]6f	72 086	72 310 *224*			
[1/2]4f	72 647	72 877 *230*	73 106 *233*		
[1/2]4f	73 138	73 374 *236*	73 609 *235*	73 853 *244*	74 081 *228*
[1/2]4f	73 513	73 763 *250*	73 999 *236*	74 234 *225*	74 465 *231*
[1/2]4f	73 658	73 904 *246*	74 137 *233*	74 367 *230*	

Table 4.1: Wavenumber positions of Rydberg state origins and vibrational progression members for the one-photon VUV laser excitation spectrum of jet-cooled I_2 between 71 000 and 75 000 cm^{-1} collecting I^+ ions using TOF-MS. The five columns on the right of the table contain wavenumber positions for vibronic transitions (v', v''). The entries given in italics correspond to the separation, in cm^{-1}, from the preceding vibrational level. The ν_{00} values in brackets are not observed on the spectrum (figure 4.2) and have been deduced to lie at positions corresponding to strong features in the absorption spectrum[8] which are likely to represent the origins of the progression members identified on the spectrum (see text for further details).

Rydberg state	ν_{00}/ cm^{-1}	(0,1)	(1,1)	(2,1)	(3,1)	(4,1)	(5,1)	(6,1)	(7,1)	(8,1)
[1/2]7p	(71 350)					72 067	72 262 *195*	72 466 *204*		
[1/2]7p	(71 705)				72 168	72 389 *221*				
[3/2]6f	72 018	71 806 *212*		72 222						
[1/2]4f	72 647			72 909	73 120 *211*					
[1/2]4f	73 138	72 924 *214*			73 639	73 875 *236*	74 106 *231*	74 332 *226*	74 572 *240*	74 807 *235*
[1/2]4f	73 513			73 783	74 022 *239*	74 234 *212*	74 465 *231*	74 672 *207*		
[1/2]4f	73 658		73 691	73 912 *221*	74 157 *245*	74 376 *219*	74 622 *246*			

Table 4.2: Wavenumber positions of Rydberg state origins and vibrational progression members of hot-bands for the one-photon VUV laser excitation spectrum of jet-cooled I_2 between 71 000 and 75 000 cm^{-1} collecting I^+ ions using TOF-MS. The seven columns on the right of the table contain wavenumber positions for vibronic transitions (v', v''). The entries given in italics correspond to the separation, in cm^{-1}, from the preceding vibrational level.

4.3.2 Assignment of Rydberg states

Rydberg states were principally assigned according to the quantum defects derived from the Rydberg equation (1.9). The ionization potentials of the $[3/2]_g$ and $[1/2]_g$ ionic states of I_2^+ were determined accurately, by ZEKE photoelectron studies[9], to be 75 069 and 80 266 cm^{-1}, respectively. Quantum defect values calculated using equation 1.9 for each Rydberg state converging on both ionic cores are given in table 4.3. These values follow closely those determined for np and nf states of the iodine atom.

The precise reproduction of part of the one-photon absorption spectrum obtained in this work as a free ion-pair formation function suggested the need for an overall reassessment of the Rydberg states accessed in one-photon transitions in terms of propensity rules and interaction with neighbouring ion-pair states. With the improvement in quality of the spectrum in the range covered, coupled with accurate values for the ionization potentials of each ionic state, a more consistent model describing the propensities for one-photon transitions was constructed, to form a broad, overall reevaluation of the Rydberg states of the halogen molecules, including Br_2 and ICl which are both discussed in this thesis. A pattern of Rydberg states, from the lowest quantum number, n, has been derived from analysis of the one-photon absorption, free ion formation and [2+1] REMPI spectra of ICl, Br_2 and I_2, in terms of the effective quantum numbers of the Ω components of those Rydberg states.

It is found that, in general, only transitions to states which have some singlet character, determined by their microconfiguration, are observed. The number of states with appreciable singlet character in any nl series varies and, for states with overall angular momentum Ω=0,1 which are accessible in one-photon transitions, there are two np and three nf states on each ionic core in a homonuclear diatomic. For low values of $n(\leq 10)$, all of these states are observed. As an exception, triplet states may also be observed for the lowest value of n in an nl series, i.e. the 6p and 4f states in I_2.

Table 4.4 shows a comparison of the range of quantum defects, for the np

ν_{00} cm^{-1}	assignment $[\Omega_c]nl$	(n-δ) with $[3/2]_g$ core	δ	(n-δ) with $[1/2]_g$ core	δ
(71 350)	[1/2]7p	5.43	-	3.51	3.49
(71 705)	[1/2]7p	5.71	-	3.58	3.42
71 968	[3/2]6f	5.94	0.06	3.63	-
72 018	[3/2]6f	6.00	0.00	3.65	-
72 086	[3/2]6f	6.05	-0.05	3.66	-
72 647	[1/2]4f	6.73	-	3.80	0.20
73 138	[1/2]4f	7.54	-	3.92	0.08
73 526	[1/2]4f	8.43	-	4.035	-0.035
73 658	[1/2]4f	8.85	-	4.08	-0.08

Table 4.3: Quantum defects and effective quantum numbers of Rydberg states assigned in the VUV spectrum of I_2. Effective quantum numbers have been calculated for each ionic core.

and *n*f Rydberg orbitals of molecular and atomic[22] iodine. Pratt investigated p and f Rydberg states in atomic iodine by two-photon excitation ([2+1] REMPI), measured with high accuracy ($\delta\nu$=0.5 cm^{-1}). Iodine atoms in the $^2P_{3/2}$ and $^2P_{1/2}$ states were formed by photodissociation of CH_3I. Atomic Rydberg states were observed and assigned to series converging to the lowest ionic state, $^3P_2$. The I.P. of the $^3P_2$ ionic state is 84 295.1 cm^{-1}. The results show that quantum defects in both molecular and atomic iodine for *n*p and *n*f Rydberg orbitals are similar in magnitude and cover a similar range. In proof of this, it has been shown that atomic quantum defects are very similar to quantum defects in molecules where the electron is removed from either a lone pair orbital or a weakly bonding/antibonding orbital with a single type of atomic parentage.

Term values of the [1/2]7p Rydberg states, which have origins lying below the effective ion-pair threshold and hence are not observed in this experiment,

Rydberg orbital	This work δ	Pratt[22] δ
*n*p	3.42-3.52	3.377-3.534
*n*f	-0.08-0.20	-0.065-0.078

Table 4.4: Comparison of quantum defects in molecular (this work) and atomic iodine.

were determined by considering the wavenumber separations of the assigned vibrational progression members of these states. This provided an estimate of the positions of the Rydberg state origins which were confirmed by comparison with the one-photon absorption spectrum in the same region[8] in which all origin bands seen in the VUV laser spectrum are observed at the same transition frequency as in the absorption spectrum.

Field-induced ion pair formation in I_2

Structure below the accurately determined thermochemical ion pair threshold ($E_{threshold}$= 72 062 cm^{-1}) in both I^+ and I^- excitation functions is observed as a consequence of the lowering of the threshold by the strong electric field, F between the repeller plates of the TOF-MS, where $F \approx 1$ kV cm^{-1}. This effect has been studied previously by Pratt et al.[23] on ion pair formation in molecular hydrogen whereby Rydberg states lying below the calculated thermochemical threshold were observed as a consequence of a field-induced reduction of the classical threshold.

The effect was studied in iodine, in this experiment, by systematically lowering the extraction voltage, adjusting the voltage across the ion optics (Einzel lens) and recording a small region of the spectrum from 71 870-72 210 cm^{-1} above and below the calculated threshold.

Under normal experimental conditions, spectra are recorded with a repeller voltage of *ca.* 2.1 kV, between two conical electrodes 1.6 cm apart, creating an electric field strength of around 1 312 V cm^{-1}. Four spectra were obtained in the wavenumber range noted above and are shown in figures 4.5(a)-(d). The effect of lowering the strength of the field used to extract ionic species, on the appearance of the spectrum was investigated by recording with repeller voltages of 860 V, 830 V, 800 V and 700 V respectively.

As the voltage and hence the field was lowered, the total ion signal became weaker, due to less energetic ion fluxes at the MCP. However, the band at 71 931 cm^{-1}, assigned as the (1,0) vibrational member of the highest lying [1/2]7p Rydberg state at 71 705 cm^{-1}, became progressively less intense relative to the other vibronic bands observed in the region as the voltage was reduced. The peak was no longer observed when the repeller voltage was set to 700 V. The effect of field-induced ion-pair formation, observed in spectra as a reduction of the thermochemical threshold by a strong electric field can be described quantitatively[22,23] by equation 4.2

$$\Delta\nu = a\sqrt{F} \tag{4.1}$$

where $\Delta\nu$ is the shift (in cm^{-1}), a is a constant (in units: $\text{cm}^{-1}\sqrt{V/cm}$) with typical measured values in the range -3.9 to -6.11 $\text{cm}^{-1}\sqrt{V/cm}$ depending on deviations from the pure Coulombic potential produced by the molecular core[23] and F is the electric field strength in V cm^{-1}. This also applies to field-induced ionization around the I.P. of a molecule.

Typically, a value of *ca.* -6 $\text{cm}^{-1}\sqrt{V/cm}$ is chosen for a. Since the lowest wavenumber cold band (ν=71 931 cm^{-1}), corresponding to an ion signal produced by ion-pair formation, effectively disappears between applied voltages of 700 and 800 V, then a value for a can be determined using equation 4.2 given the thermochemical threshold (ν=72 062 cm^{-1}), the required shift ($\delta\nu$=131 cm^{-1}) and the electric field strengths in each case. This yields a value for a=-6.26 $\text{cm}^{-1}\sqrt{V/cm}$ which is similar to the typical measured value.

To illustrate this, table 4.5 shows the calculated reduction, in cm^{-1}, of the classical threshold for the field strength applied, using a value of a=-6.26 $\text{cm}^{-1}\sqrt{V/cm}$. The shift, in cm^{-1}, under normal experimental conditions, using a field strength of *ca.* 1 310 V cm^{-1}, calculated from equation 4.2 is therefore of the order 227 cm^{-1}. The ion-pair threshold labelled on the assigned spectrum in figure 4.2 has

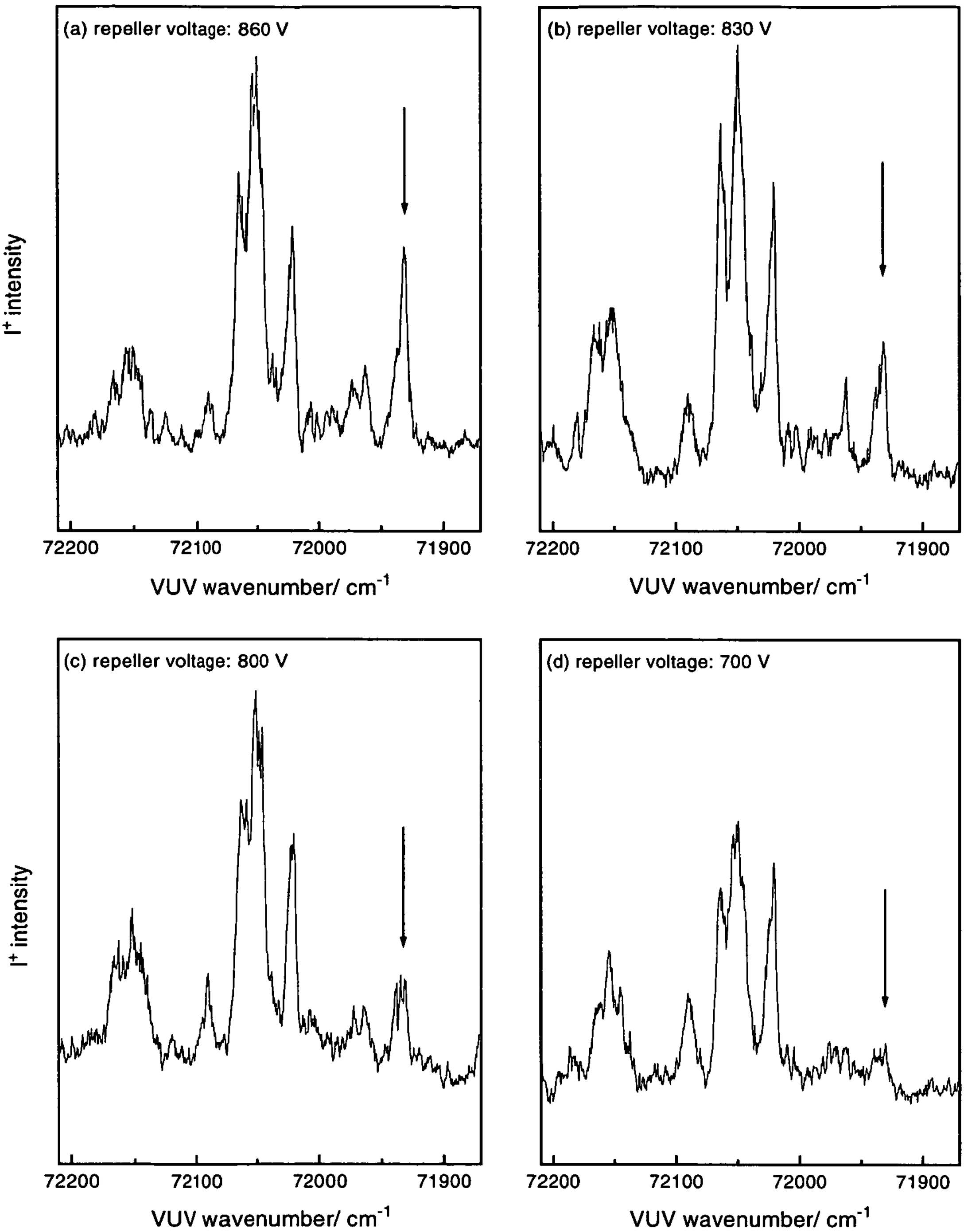

Figure 4.5: Effect on lowest observed cold band ([1/2]7p, v'=1 at 71 930 cm^{-1}) below the calculated ion pair threshold (72 062 cm^{-1}) with varying repeller voltages. The position of the band is indicated in each spectrum by an arrow.

Repeller Voltage/ V	Δ/ (cm^{-1})	Threshold/ (cm^{-1})
2100	227	71 835
860	145	71 917
830	142	71 919
800	140	71 922
700	131	71 931

Table 4.5: Field induced reduction of thermochemical ion-pair threshold of molecular iodine (72 062 cm^{-1}) with varying repeller voltage.

been positioned to indicate this shift.

4.4 Discussion

4.4.1 General observations from experimental results

The one-photon, VUV spectrum of I_2 has been recorded by collecting ion signals due to I^+ and I^- ionic fragments. From the experimental results, the spectrum, recorded at high resolution, appear to consist of very sharp bands in a highly structured ion excitation function. All ion signals due to I^+ and I^- ionic fragments are seen at frequencies corresponding to structure in the high-resolution absorption spectrum[8]. More bands are observed in the room temperature absorption spectrum, due to hot band transitions originating from up to v''=4 in the ground state, than in the ion excitation function obtained in this experiment which employed jet-cooling of the sample, thus producing a cleaner spectrum with narrower rotational contours and fewer vibrational hot-bands.

All bands in the I^- spectrum are seen at the same position, within experimental error, in the I^+ spectrum which indicates that ion-pair formation is occuring for every band seen in the absorption spectrum. The large amount of well-defined structure and the absence of any underlying continua indicates that the fragment ions are formed principally by predissociation of molecular Rydberg states rather than by direct dissociation by transition to the the ion-pair continuum.

The processes occuring on excitation may be described by

$$I_2 + h\nu_{VUV} \rightarrow I_2^* \rightsquigarrow I^+ + I^-$$

$$I_2^* + h\nu_{UV/vis} \rightarrow I_2^+/I + I^+$$

i.e. two channels leading to production of I^+ are available: ion-pair formation *via* predissociation of an excited state and multiphoton ionization-dissociation by a VUV photon and one of the fundamental (UV/vis.) beams. However, ion-pair formation would appear to be the major channel, since a good signal to noise ratio was observed when the detection apparatus was configured to collect I^- fragments and the focal points of the VUV beam relative to those of the UV and visible beams were very different. A better signal to noise ratio was presented in the I^+ spectra, which was expected for experimental reasons, related to the greater collection efficiency of positive ions relative to negative ions. Band positions were therefore measured only from scans collecting I^+ ions.

Intensities of bands are non-Franck-Condon and are a product of two terms; the Franck-Condon factors for Ryd←X and a vibrational overlap term which determines the efficiency of coupling between the Rydberg and ion-pair state. The competing process of multiphoton ionization must also be taken into account but, given that only a weak molecular ion signal was observed above the IP, is unlikely to be a major channel unless dissociation of the ionic state to produce $I+I^+$ is efficient.

From the measured band positions in the spectra, assignments were made by calculating the effective quantum number, and hence the quantum defect, of each state. A clear pattern of low n Rydberg states, with extensive vibronic structure, with several Ω components of the 7p and 4f states, based on the Ω_c=1/2 ionic core were assigned. Three components of the [3/2]6f Rydberg states, with compatible quantum defects were also assigned. Effective quantum numbers for each Rydberg state on the alternative spin-orbit states of the ion yielded inconsistent quantum defects for assignment to np or nf Rydberg states. It is noted that most of the states assigned here are convergent on the higher energy spin-orbit component of the ionic core, conferring a lower principal quantum number, n, on each series than would be observed in series converging to the lower energy spin-orbit component (Ω_c=3/2). This is expected given the $1/n^3$ relationship for the oscillator strength of Rydberg←X transitions, with principal quantum number, n. Hence, Rydberg states with higher n in the same region, convergent on the Ω_c=3/2 ionic core, are expected to have a much lower transition probability. Only the *ungerade* np and nf Rydberg states, coupled to the *gerade* $[3/2]_g$ and $[1/2]_g$ cores, were assigned here in order to conserve the overall *ungerade* symmetry of the ground (*gerade*) state to Rydberg state transition. Rydberg electrons in either ns or nd orbitals coupled to the $[3/2]_g$ or $[1/2]_g$ ionic cores form overall *gerade* Rydberg states which are generally only observed in two-photon excitation, following the g→g selection rule.

4.4.2 Comparison with the one-photon absorption spectrum

Table 4.6 shows the wavenumber positions and calculated quantum defects of the Rydberg states assigned in this work (ion pair excitation function of I_2 using a VUV laser) and the corresponding wavenumber positions and quantum defects from Venkateswarlu[8] of the same Rydberg state origins. The quantum defects for the assignments by Venkateswarlu have been calculated using the reported values for the ionization potentials for the two ionic cores.

From the table, it is noted that the quantum defects of the various *n*p series assigned by Venkateswarlu (labelled *f, j*) are consistent with those derived in this work. However, the band positions of the origins of these series differ markedly from the present results. The quantum defect values used to fit the *n*f Rydberg states, on each ionic core, to each series are rather high (δ ~0.7-1.1) compared to the currently accepted range of values (δ ~-0.08-0.20) based on atomic I quantum defects. For these states (*g, k, l, q, r* and *s'*), again, the band positions differ largely from those in the present work.

This discrepancy can be attributed to the inaccurate ionization potentials Venkateswarlu used for each ionic core: $IP(^2\Pi_{3/2g})$=75 815 cm^{-1} and $IP(^2\Pi_{1/2g})$= 80 895 cm^{-1}. These values were derived by identifying several Rydberg series of states and, by extrapolation, determining a common limit corresponding to the I.P. of an ionic core. The spectral region around the ionization limit in the absorption spectrum was very congested making a precise determination of the I.P. impracticable. With the benefit of a ZEKE study on the molecule, the vertical ionization energy was determined with high accuracy and the adiabatic IP deduced (75 069 cm^{-1}). Hence, a different limit on the Rydberg equation, substituted with the same value of δ (and n) yields different values of ν_{00}.

The Rydberg series derived by Venkateswarlu have been classified carefully, in terms of the Hund's case (c) configuration and in terms of the bonding nature of the Rydberg orbital (i.e. λ_i specified). For example, the series labelled f notates a series of $np\sigma_u$ states converging on the $[1/2_g]$ ionic core with overall $\Pi_{0_u^+}$ symmetry. An attempt was made by Venkateswarlu to relate the intensities of the Rydberg series to the electronic configurations through a variety of propensity rules governing the transitions. For example, the o' series $[^2\Pi_{1/2g}]\mathrm{f}\sigma_u$; $\Pi_{0_u^+}$ was considered stronger than the o series $[^2\Pi_{1/2g}]\mathrm{f}\sigma_u$; Π_{1u}, indicating a propensity for $\Delta\Omega$=0 for Ryd←X0_g^+ transitions.

However, since none of the assignments made in the present work in terms of the band positions, concur with those reported in the one-photon absorption work, then an alternative methodology to classify the observed Rydberg states was developed.

4.4.3 Classification of Rydberg states

Two components of the $[1/2]_g$7p, three of the $[3/2]_g$6f and four of the $[1/2]_g$4f Rydberg states are assigned. Excited states of iodine are generally classified by the overall angular momentum, Ω, according to Hund's case (c) coupling scheme. Under this scheme, Ω is the only 'good' quantum number which can be used to classify an excited electronic state. Ω is the component along the internuclear axis of the total angular momentum J, derived from the vector sum of the spin

present work ν_{00}/ cm^{-1}	assignment $[\Omega_c]nl$	δ	Venkateswarlu[8] ν_{00}/ cm^{-1}	series	δ
(71 350)	[1/2]7p	3.49	71 705	f	3.55
(71 705)	[1/2]7p	3.42	72 283	j	3.43
71 968	[3/2]6f	0.06	71 350	g	1.04
72 018	[3/2]6f	0.00	71 570	k	0.92
72 086	[3/2]6f	-0.05	71 697	l	0.84
72 647	[1/2]4f	0.20	67 930	q	1.09
73 138	[1/2]4f	0.08	69 410	r	0.91
73 526	[1/2]4f	-0.04	70 064	s'	0.82
73 658	[1/2]4f	-0.08	70 388	s'	0.77

Table 4.6: Assignments, band positions and quantum defects of electronic origins of the observed Rydberg states in this work (ion-pair excitation function using a VUV laser) and the band positions of the same origins assigned by Venkateswarlu from his high resolution, one-photon absorption spectrum. The column labelled "series" indicates the notation used by Venkateswarlu to identify a Rydberg series (see ref.[8]).

and orbital angular momenta on each atom centre, S and L, respectively, which couple together more strongly than with the field around the internuclear axis.

$$J = |L \pm S|$$

However, the overall angular momentum of the Rydberg state is obtained from the coupling of the overall angular momentum of the Rydberg electron, ω_{Ryd} and the overall angular momentum of the ionic core with which it is associated, Ω_c, by

$$\Omega = |\Omega_c \pm \omega_{Ryd}|$$

The Rydberg states assigned in this work are convergent on both the lower and higher spin-orbit components of the molecular ionic state; $^2\Pi_{3/2g}$ and $^2\Pi_{1/2g}$.

Hence, the total angular momentum of the ionic core, Ω_c, with respect to the internuclear axis is 3/2 or 1/2, respectively. The total angular momentum of the np or nf Rydberg electron can take a range of values or components. These can be calculated by considering the spin of the electron and the nature of bonding of the electron to the ionic core, i.e. depending on the type of orbital which the Rydberg electron occupies.

A detailed discussion of the assignments presented here follows, including further classification of each component of the Rydberg states observed and the role of interacting ion-pair states in the detection of these bands as unbound ion pairs. Each set of Rydberg states, np and nf, are treated separately.

The [1/2]7p Rydberg states

Any Rydberg state associated with a particular ionic core has a number of non-degenerate components depending on the symmetry of the orbital which the Rydberg electron occupies. In the atomic case, the orbital angular momentum, l, is split into $2l$+1 components denoted m_L, where m_L=l, l-1, ..., -l. In the molecular case, the symbol λ is used where λ=$|m_\lambda|$. The symmetry type of the Rydberg orbital is denoted σ, π, δ, φ, ... for λ=0, 1, 2, 3, ..., where λ takes positive values only.

Rydberg state $[1/2]n\mathrm{p}\lambda$	λ_i	Configuration
$[1/2]n\mathrm{p}\sigma$	0	$0_u{}^+$, 1_u
$[1/2]n\mathrm{p}\pi$	1	$0_u{}^+$, $1_u(1)$, $1_u(2)$ and 2_u

Table 4.7: Hund's case (c) configurations of Rydberg series of states of $n\mathrm{p}\sigma$ and $n\mathrm{p}\pi$ Rydberg electrons coupled to the $^2\Pi_{1/2}$ core under Ω_c-ω_{Ryd} coupling. The λ_i value indicates the orientation of the Rydberg orbital with respect to the internuclear axis.

For example, a single np electron in a Rydberg orbital has a total spin angular momentum of 1/2 and can occupy a molecular orbital with σ- or π-type symmetry, since l=1 and λ=0, 1. Ω values calculated using Ω_c-ω_{Ryd} coupling for $[1/2]n$p Rydberg states are presented in table 4.7.

The overall spin multiplicity of the Rydberg state can be determined from correlating the microconfiguration of the Rydberg state to the Hund's case (a) configuration. Table 4.8 shows the microconfigurations of the Ω components of an np Rydberg state with both partial singlet and purely triplet character in the $[\Omega_c](\lambda m_S)_{Ry}$ coupling scheme. The rightmost column indicates the orbital occupancy of the core π_g^* orbitals and the symmetry type of the Rydberg orbital using the notation 0≡pσ and 1≡pπ.

Using the selection rules for one-photon transitions ($\Delta\Omega$=0, 1), only states with configurations $0_u{}^+$ and 1_u can be accessed. Under Hund's case (c) coupling scheme, therefore, the $n\mathrm{p}\sigma$ or the $n\mathrm{p}\pi$ Rydberg series of states may be involved,

Ω_c	Ω	$^{2S+1}\Lambda$	microconfiguration $[...]_c(\lambda m_S)_{Ry}$
3/2	2	$^{1,3}\Delta$	$[1^+1^-\underline{1}^+]_c1^-$
	1	$^{1,3}\Pi$	$[1^+1^-\underline{1}^+]_c0^-$
	$0^\pm$	$^{1,3}\Sigma^\pm$	$1/\sqrt{2}([1^+1^-\underline{1}^+]_c\underline{1}^-\pm [\underline{1}^-\underline{1}^+1^-]_c1^+])$
	3	$^3\Delta$	$[1^+1^-\underline{1}^+]_c1^+$
	2	$^3\Pi$	$[1^+1^-\underline{1}^+]_c0^+$
	1	$^3\Sigma^\pm$	$[1^+1^-\underline{1}^+]_c\underline{1}^+$
1/2	2	$^{1,3}\Delta$	$[1^+1^-\underline{1}^-]_c1^+$
	1	$^{1,3}\Pi$	$[1^+1^-\underline{1}^-]_c0^+$
	$0^\pm$	$^{1,3}\Sigma^\pm$	$1/\sqrt{2}([1^+1^-\underline{1}^-]_c\underline{1}^+\pm [\underline{1}^-\underline{1}^+1^+]_c1^-])$
	1	$^3\Delta$	$[1^+1^-\underline{1}^-]_c1^-$
	1	$^3\Sigma^-$	$[1^+\underline{1}^+\underline{1}^-]_c1^+$
	$0^\pm$	$^3\Pi$	$1/\sqrt{2}([1^+1^-\underline{1}^-]_c0^-\pm [\underline{1}^-\underline{1}^+1^+]_c0^+])$

Table 4.8: The microconfigurations of the Ω components of the np Rydberg states on each ionic core. The table indicates the electron arrangement in the core π_g orbitals, the symmetry type of the Rydberg orbital and the Hund's case (a) and case (c) configurations of each component.

since both have components with the appropriate configuration. Following the propensity rules for transitions to np Rydberg states on both ionic cores, two states with singlet character and Ω=0, 1 are expected to be observed, according to the data in table 4.8.

The nf Rydberg states

An equivalent argument for the classification of the nf Rydberg states can be applied. Here, λ_i, the orbital angular momentum component of the f Rydberg electron, can take values 0, 1, 2 and 3, producing fσ, fπ, fδ and fφ states. The microconfigurations for the nf Rydberg states on each core is shown on table 4.9,

Ω_c	Ω	$^{2S+1}\Lambda$	microconfiguration $[...]_c(\lambda m_S)_{Ry}$
3/2	1	$^{1,3}\Pi$	$[1^-\underline{1}^+\underline{1}^+]_c2^+$
	1	$^{1,3}\Pi$	$[1^+1^-\underline{1}^+]_c0^-$
	$0^\pm$	$^{1,3}\Sigma^\pm$	$1/\sqrt{2}([1^+1^-\underline{1}^+]_c\underline{1}^-\pm [\underline{1}^-\underline{1}^+1^-]_c1^+])$
	1	$^3\Sigma$	$[1^+1^-\underline{1}^+]_c\underline{1}^+$
	$0^\pm$	$^3\Sigma^\pm$	$1/\sqrt{2}([1^+1^-\underline{1}^+]_c\underline{2}^+\pm [\underline{1}^-\underline{1}^+1^-]_c2^-])$
1/2	1	$^{1,3}\Pi$	$[1^+\underline{1}^+\underline{1}^-]_c2^-$
	1	$^{1,3}\Pi$	$[1^+1^-\underline{1}^-]_c0^+$
	$0^\pm$	$^{1,3}\Sigma^\pm$	$1/\sqrt{2}([1^+1^-\underline{1}^-]_c\underline{1}^+\pm [\underline{1}^-\underline{1}^+1^+]_c1^-])$
	1	$^3\Delta$	$[1^+1^-\underline{1}^-]_c1^-$
	1	$^3\Sigma^-$	$[1^+\underline{1}^+\underline{1}^-]_c1^+$
	$0^\pm$	$^3\Pi$	$1/\sqrt{2}([1^+1^-\underline{1}^-]_c0^-\pm [\underline{1}^-\underline{1}^+1^+]_c0^+])$

Table 4.9: The microconfigurations of the Ω components of the nf Rydberg states on each ionic core. The table indicates the electron arrangement in the core π_g orbitals, the symmetry type of the Rydberg orbital and the Hund's case (a) and case (c) configurations of each component.

indicating the accessible Ω states with partial singlet character.

Following the propensity rules described above and the general observations from the reassignment of the spectrum, three [3/2]6f and four [1/2]4f states are assigned. Three of these 4f states are assigned as partially singlet in character, with a fourth, triplet state also observable.

4.4.4 Predissociation mechanism for ion-pair formation

As mentioned above, the free ion-pair formation spectrum is a precise reproduction of the absorption spectrum in the wavelength range covered, hence, ion-pair

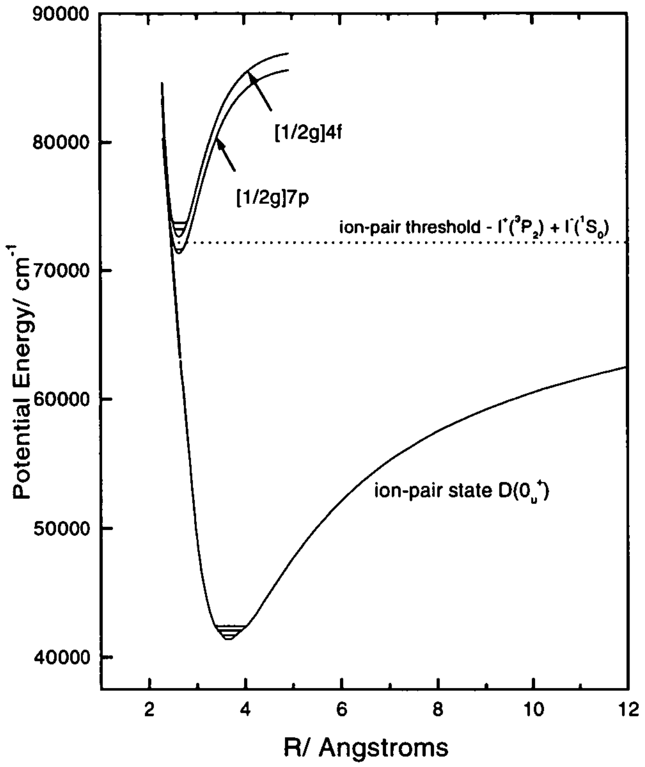

Figure 4.6: Schematic diagram of predissociation of a [1/2]7pπ Rydberg state by the repulsive limb of the $D(0_u^+)$ ion-pair state to form ion pairs.

formation is occuring from all states accessed and observed at the one-photon level. The overall mechanism from initial excitation to ion-pair formation is discussed here.

Figure 4.6 shows a schematic diagram of the potential energy curves of some of the relevant states involved in the ion-pair formation process, including the $D(0_u^+)$ ion-pair state and the $[1/2]_g7p$ and $[1/2]_g4f$ Rydberg states. The ion-pair state curve has been drawn from knot points used to generate a simulation of the E ion-pair state[24] potential curve. These values were used since it is known that the E ion-pair state potential possesses a similar form and occupies a similar region of $R-E$ space to the D state, which has been observed as an extensive progression by direct i.p.←X single-photon transition and modelled using Dunham coefficients[25]. It was, however, more convenient to use the RKR data reported for the E state to represent the schematic in figure 4.6. The Rydberg state curve was generated using a simple program for plotting a Morse potential using input data for ω_e=243.9 cm^{-1}, r_e=2.63 Å and D_e=14 610 cm^{-1} from ref. [18]. Excitation by one VUV photon to a vibronic level in a Rydberg state is followed by predissociation *via* the repulsive limb of an ion-pair state. Effectively, coupling between the bound Rydberg state vibronic level and the ion-pair continuum occurs and unbound pairs of ions are formed over a certain timescale, which may be greater than or approximately equal to one vibrational period. Given the narrow bandwidths of the resonances in the spectrum (of the order 3-10 cm^{-1} fwhm) it would appear that predissociation is occuring on a timescale significantly greater than one vibrational period (*ca.* 20 fs).

Two *ungerade* ion-pair states lying in the lowest tier are available for homogeneous interaction with Rydberg states accessible by a one-photon transition: the $D(0_u^+)$ and $\gamma(1_u)$ ion-pair states which have Ω values of 0 and 1, respectively. Both of these states correlate with dissociation products $I^+(^3P_2)+I^-(^1S_0)$. The D state has a [1441] configuration (in $[ijkl]$ notation) and the γ state has a [2332] configuration. It is thought that the repulsive limb extends above the dissociation threshold such that Rydberg states in this region are nested within the ion-pair curve in the continuum, as shown on figure 4.6. The $\gamma(1_u)$ state is also thought to occupy a similar region of $R - E$ space, given that all six ion-pair states in the lowest energy tier are clustered closely together, although it is not directly observable by a one-photon transition since the electronic configuration is a product of the movement of two electrons. Hence, a good overlap term exists between the wavefunctions on the repulsive limbs of the ion-pair and Rydberg states.

One further important factor in the predissociation mechanism is the strength of interaction between the two states in terms of the nature of the two-electron exchange which connects the configurations of the Rydberg and ion-pair states. The strongest interactions occur for two parallel transitions (i.e. $\sigma \rightarrow \sigma$ or $\pi \rightarrow \pi$) and the weakest for two perpendicular transitions (i.e. $\sigma \nleftrightarrow \pi$). Two [1/2]7p Rydberg states with singlet character and Ω=0 or 1 are accessed by one-photon transition. Using the information in table 4.8, these can be represented as $[1/2]_g 7\mathrm{p}\pi_u$; 0 ($^{1,3}\Sigma^{\pm}$) and $[1/2]_g 7\mathrm{p}\sigma_u$; 1 ($^{1,3}\Pi$). These configurations connect *via* two-electron exchange with the $\mathrm{D}0_u^+[1441]$ and $\gamma 1_u[2332]$ ion-pair state configurations, respectively. The Ω=1 components of the [1/2]7p Rydberg state, with configuration 1_u may interact with the $\mathrm{D}(0_u^+)$ ion-pair state by heterogeneous predissociation. This is less probable since any perturbations of a heterogeneous nature arise only through interaction of rotational and electronic motion, where the transition probability is proportional to the rotational energy (or J^2) of the state being predissociated and is zero for $J=0$. An alternative explanation is therefore found in invoking the $\gamma(1_u)$ state.

The nature of the electron transitions in each of these interactions is summarised in table 4.10. The band position of each of these Rydberg states in the spectrum is included, by relating the strengths of the observed vibronic bands of each state to the strength of the predicted interaction. For example, the state with an origin at 71 350 cm^{-1} has the most intense progression members and so is assigned $[1/2]_g 7\mathrm{p}\pi_u$; 0 since this is predicted to connect with the D state *via* two parallel transitions.

The two-electron exchange between the $[1/2]7\mathrm{p}\sigma$; 1 Rydberg state, with singlet character and the γ ion-pair state would appear to be at variance with the Laporte selection rule since

$$[2430]\sigma_u \leftrightarrow [2332]$$

involves $\mathrm{p}\sigma_u \rightarrow \mathrm{p}\sigma_u^*$ and $\mathrm{p}\pi_u \rightarrow \mathrm{p}\sigma_u^*$ electronic transitions which are both electric dipole-forbidden. However, it has been shown[26] that these two configurations can mix weakly at energies corresponding to bound levels of the ion-pair state. It is

Rydberg state	ν_{00}/ cm^{-1}	$n-\delta$	ion-pair state	nature of transition strength
$[1/2]_g 7\mathrm{p}\pi_u$; 0 ($^{1,3}\Sigma^{\pm}$)	71 350	3.51	D	2 x $\|$(s)
$[1/2]_g 7\mathrm{p}\sigma_u$; 1 ($^{1,3}\Pi$)	71 705	3.58	γ	2 x $\perp$(w)

Table 4.10: Type of two-electron exchange and relative strength of the interaction between the [1/2]7p Rydberg states and D or γ ion-pair states. The band positions and effective quantum numbers of each Rydberg state in the VUV free ion-pair spectrum are included.

also assumed that a homogeneous interaction (Ω_{Ryd}=$\Omega_{i.p.}$) is the most favourable.

The predissociation mechanism, from initial excitation from the ground state to production of unbound ion-pairs can be regarded as essentially a three-stage process. For example, the strongest predicted transition presented in table 4.10 can be represented as an initial parallel transition ($\pi \rightarrow \pi$) from the ground state, X(0_g^+), to the singlet component of the [1/2]7pπ Rydberg state (4.2) followed by two-electron exchange (4.3) connecting the configurations of the Rydberg state and the ion-pair state (D(0_u^+)), representing two parallel transitions ($\pi \rightarrow \pi^*$ and $\sigma \rightarrow \sigma^*$).

$$[(\sigma_g)^2(\pi_u)^4(\pi_g)^4(\sigma_u)^0] \rightarrow [(\sigma_g)^2(\pi_u)^4(\pi_g)^3(\sigma_u)^0]7p\pi \tag{4.2}$$

$$[(\sigma_g)^2(\pi_u)^4(\pi_g)^3(\sigma_u)^0]7p\pi \leftrightarrow [(\sigma_g)^1(\pi_u)^4(\pi_g)^4(\sigma_u)^1] \tag{4.3}$$

As this exchange takes place, the Rydberg state effectively forms the inner repulsive limb of the ion-pair state at an energy above the ion-pair threshold and at small internuclear separation. As the atoms move apart, the bonding characteristics of the Rydberg state have been removed and the atoms correlate with ionic dissociation products $I^+(^3P_2)$ and $Cl^-(^1S_0)$.

The precise nature of the predissociation mechanism is uncertain. A great deal of information can be inferred on whether a homogeneous or heterogeneous interaction is occuring by analysis of the rotational band contour of the predissociating state. However, no reproducible band contours were obtained for slow scans over certain origin bands in the spectrum. For this work, therefore, a purely homogeneous predissociation mechanism is assumed.

4.5 Conclusions

Ion-pair formation from jet-cooled molecular iodine has been observed for the first time at high resolution using a purpose-built VUV laser system. Using time-of-flight mass spectrometry, ion excitation functions for both I^+ and I^- charged species were recorded in the wavenumber range 71 000-75 000 cm^{-1}. Assignments were made to two components of the [1/2]7p Rydberg state, three components of the [3/2]6f Rydberg state and four components of the [1/2]4f Rydberg state, derived from quantum defect analysis.

All structure in the spectrum was found to correspond within experimental error to structure in the high-resolution one-photon absorption spectrum, reported by Venkateswarlu using a photographic technique, in the wavenumber range covered. Comparison of the assignments to Rydberg states in each work showed no correlation. This was attributed to largely different values for the ionization potentials derived by Venkateswarlu as limits for several identified series, compared with the accurately determined ionization potential data used in this work, obtained from a ZEKE experiment. Ion pair formation was verified by comparing spectra recorded collecting both positive and negative atomic iodine ions separately. The two were entirely equivalent within experimental error and it was concluded that oppositely charged pairs of ions are being produced by the same mechanism. Ion-pair formation below the calculated thermochemical threshold was observed as a consequence of a field-lowering effect induced by the strong electric field present in the ionization region of the TOF-MS.

Comparison of the spectra obtained in this work with a similar experiment performed using a synchrotron VUV source, also with time-of-flight mass spectrometry to collect I^+ and I^- ions, showed that each broad feature in the synchrotron spectrum actually consisted of several vibronic levels in the VUV laser spectrum and was much more complicated and detailed than originally believed. However, note was made of the proposed mechanism involved in the ion pair formation process reported in the synchrotron work, whereby a homogeneous interaction by the $D(0_u^+)$ ion-pair state led to selective predissociation of $np\pi$ Rydberg states with configuration, 0_u^+.

This mechanism was modified and extended to account for the presence of several Ω components of the $[1/2]_g7$p, $[3/2]_g6$f and $[1/2]_g4$f Rydberg states observed in the high-resolution work presented here. Both the $D0_u^+$ and $\gamma(1_u)$ ion-pair states were invoked in the predissociation mechanism, assuming a homogeneous interaction with Ω=0 and Ω=1 Rydberg states, respectively. The most probable interactions were determined by considering the nature of the two-electron exchange mechanism between interacting ion-pair and Rydberg states.

4.6 References

[1] P. Venkateswarlu, *Can. J. Phys.* **48** (1970) 1055

[2] A. Kvaran, A.J. Yencha, D.K. Kela, R.J. Donovan and A. Hopkirk, *Chem. Phys. Lett.* **179** (1991) 253

[3] R.S. Mulliken, *Phys. Rev.* **46** (1934) 549

[4] R.S. Mulliken, *Phys. Rev.* **57** (1940) 500

[5] K. Wieland and J. Waser, *Nature* **160** (1947) 643

[6] P. Venkateswarlu, *Proc. Indian Acad. Sci.* **A24** (1946) 473

[7] L. Mathieson and A.L.G. Rees, *J. Chem. Phys.* **25** (1956) 753

[8] H. Cordes, *Z. Phys.* **97** (1935) 603

[9] R.S. Mulliken, *J. Chem. Phys.* **55** (1971) 288

[10] D.A. Beattie, *Private Communication* (1997)

[11] J.D. Morrison, H. Hurzeler, M.G. Inghram and H.E. Stanton, *J. Chem. Phys.* **33** (1960) 821

[12] J.A. Myer and J.A.R. Samson, *J. Chem. Phys.* **52** (1970) 716

[13] M.E. Akopyan, F.I. Vilesov and Y.L. Sergeev, *Opt. Spec.* **35** (1973) 472

[14] R.J. Donovan, B.V. O'Grady, K. Shobatake and A. Hiraya, *Phys. Lett.* **122** (1985) 612

[15] A.J. Yencha, D.K. Kela, R.J. Donovan, A. Hopkirk and A. Kvaran, *Chem. Phys. Lett.* **165** (1990) 283

[16(a)] F.W. Dalby, G. Petty-Sil, M.H.L. Pryce and C. Tai, *Can. J. Phys.* **55** (1977) 1033

[16(b)] K. Lehmann, J. Smolarek and L. Goodman, *J. Chem. Phys.* **69** (1978) 1569

[17] L. Zandee, R.B. Bernstein and D.A. Lichtin, *J. Chem. Phys.* **69** (1978) 3427

[18] K.P. Lawley, T. Ridley, Z. Min, P.J. Wilson, M.S.N. Al-Kahali and R.J. Donovan, *Chem. Phys.* **197** (1995) 37

[19] L. Minnhagen, *Ark. Fys.* **21** (1962) 415

[20] D. Hanstorp and M. Gustafsson, *J. Phys. B: At. Mol. Opt. Phys.* **24** (1992) 1773

[21] F. Martin, R. Bacis, S. Churassy and J. Verges, *J. Mol. Spec.* **116** (1986) 71

[22] S.T. Pratt, *Phys. Rev. A* **32** (1985) 928

[23] S.T. Pratt, E.F. McCormack, J.L. Dehmer and P.M. Dehmer, *Phys. Rev. Lett.* **68** (1992) 584

[24] E.D. Poliakoff, J.L. Dehmer, A.C. Parr and G.E. Leroi, *Chem. Phys. Lett.* **111** (1984) 128

[25] P.J. Wilson, T. Ridley, K.P. Lawley and R.J. Donovan, *Chem. Phys.* **182** (1994) 325

[25] A. Hiraya, K. Shobotake, R.J. Donovan and A. Hopkirk, *J. Chem. Phys.* **88** (1988) 52

[27] K.P. Lawley and R.J. Donovan, *J. Chem. Soc. Farad. Trans.* **89** (1993) 1885

Chapter 5

Ion-Pair Formation from ICl Using VUV Laser Radiation

5.1 Introduction

In the previous chapter the results of ion-pair formation from I_2 following one-photon excitation using a VUV laser source, were reported. Comparison was made with the high-resolution, one-photon absorption spectrum (chapter 4, ref. [1]) and previous work at low resolution, using a synchrotron source, on ion-pair formation (chapter 4, ref. [2]). A complete reassignment was made based on these comparisons and from the propensity rules for electronic transitions in the halogen diatomics derived from the re-examination of the two-photon spectrum of Br_2, discussed in chapter 3. Furthermore, the predissociation mechanism for ion-pair formation from I_2 was discussed in some detail in terms of two-electron exchange. The same approach will be made to ICl here with due reference to the discussion presented in the previous two chapters.

5.1.1 Background to the spectroscopy of ICl

The higher excited states of the diatomic halogens and interhalogens have been studied using both continuum sources[1-3] and synchrotron radiation[4-6]. While both methods have their own merits (high resolution and high brightness, respectively), an accurate description of the higher members of the various Rydberg systems as they converge on the ionization limit has so far remained elusive.

To elaborate on this, the VUV absorption spectrum of ICl between 52 500 and 82 000 cm^{-1}, photographed by Venkateswarlu[1] covers the entire range of Rydberg states to above the ionization limit, at high resolution. However, the assignments given in this work were made using inaccurate data for the ionization potentials of the two spin-orbit split ionic cores on which the various Rydberg series converge. Furthermore, no attempt to identify the many interactions with ion-pair systems in the same region was made. This was also the case for the halogens, I_2 and Br_2[2,3].

With the advent of synchrotron radiation as a source of VUV wavelengths, several studies have been made on the Rydberg and ion-pair states of the halogens and interhalogens, up to the ionization limit[4–8]. These studies have been carried out with the advantage of marrying techniques such as absorption spectroscopy, fluorescence excitation, dispersed fluorescence and time-of-flight mass spectrometry. While a great deal of information regarding Ryd/ion-pair interactions at the bound level has been achieved, the overall picture, certainly at energies above the ion-pair threshold where unbound ion-pairs are observed to be formed, is somewhat simplistic.

Vibrational analyses of ion-pair states have been carried out using the optical-optical double resonance (OODR) technique[9,10] and by fluorescence studies using coherent, monochromatic tunable VUV radiation generated by four-wave mixing in Mg vapour[11]; both are laser-based methods. Four-wave mixing in krypton in conjunction with TOF-MS has been employed to probe vibrational levels, with rotational analysis, of the $E0^+$ ion-pair state in $^{79}Br^{35}Cl$ [12]. A number of other studies on bound ion-pair levels in other interhalogens, BrCl and IBr, using VUV laser radiation, by Lipson[13,14] may be included but again, as with all the above, concentrate rather locally on any one given system.

In the work described in this chapter, an extensive survey of the Rydberg states above the first ion-pair threshold to the first ionization limit has been made. This has been achieved using a source of tunable VUV radiation generated by four-wave mixing in krypton, in conjunction with TOF-MS to allow mass resolution of product ions. Jet-cooling of the sample was also employed to maintain narrow rotational band contours and keep the spectrum clear of hot band structure.

Analysis of the spectra obtained has resulted in significant reassignments of several Rydberg series observed at the one-photon level. This has been prompted by the general, overall reassessment of the Rydberg states of the halogens and interhalogens in terms of propensity rules involving $\Delta\Omega$ transitions and spin characteristics[15].

5.2 Experimental

Full details of the experimental methods for generating VUV radiation by four-wave mixing in krypton and subsequent detection of ionic species by TOF-MS are given in chapter 2. In the present experiments, VUV frequencies were generated using the two-photon resonant states $5p[1/2]_0$, $5p[3/2]_2$ and $5p[5/2]_2$ in krypton at 94 094, 93 123 and 92 308 cm^{-1} respectively, with the fundamental output of dyes Coumarin 307, Coumarin 102, Rhodamine 6B and Rhodamine 700, providing the difference frequency. A sample of solid ICl_3, which dissociates to *ca.* 29 Torr of ICl and Cl_2 at 300 K, was stored in a bulb between a He line and the pulsed valve. The molecular beam of ICl was generated by seeding the gaseous mixture in *ca.* 300 Torr of He and passing through a pulsed nozzle as described in chapter 2.

5.3 Results & Discussion

5.3.1 General features & observations from experimental data

The one-photon excitation function spectrum of ICl has been recorded in the wavenumber region 72 500-81 000 cm^{-1}, between the first ion-pair threshold (corresponding to dissociation products $I^+(^3P_2)$ + $Cl^-(^1S_0)$) and the lowest spin orbit component of the ion (ICl^+, $^2\Pi_{3/2}$). Using TOF-MS, mass-resolved spectra due to I^+, $^{35}Cl^-$ and $^{37}Cl^-$ ion fragments were obtained.

The ion-pair threshold for states in the lowest tier of ion-pair states was determined accurately to be $E[I^+(^3P_2) + Cl^-(^1S_0)]$=72 522 cm^{-1}. This was derived from thermochemical and spectroscopic data using IE(I)=84 295.1 cm^{-1}[116], EA(Cl)=29 138.2 cm^{-1}[117] and D_o(I-Cl)=17 365 cm^{-1}[118]. The observed onset of Cl^- and I^+ ion-pair formation agrees well with this threshold.

Above the threshold, the spectrum appears to consist of several sharp, well-resolved bands in a highly structured ion excitation function. Similarily to the VUV spectrum of I_2 discussed in the previous chapter, the absence of any underlying continua further indicates that fragment ions are formed by predissociation of molecular Rydberg states rather than by direct dissociation. Spectra were recorded on the $I^{35}Cl^+$ molecular ion mass channel, but showed no structure below the first ionization limit, indicating that multiphoton ionization is not a major channel in the excitation scheme.

Spectra recorded on the I^+ mass channel were equivalent (allowing for structure due to $I^{37}Cl$ in the I^+ excitation function), which indicated that the two species are formed by the same process. Furthermore, all features in either excitation function are also present in the one-photon absorption spectrum[1], with the exception of some hot bands. It is concluded that Rydberg states in this region, seen in absorption are being efficiently predissociated by suitable ion-pair states into separate ion-pair fragments.

Intensities of bands are a product of Franck-Condon factors for Ryd←X transitions and a vibrational overlap term between Rydberg and ion-pair states. However, intensity data are unreliable given that the spectra in figure 5.1-5.3 were composed of a number of shorter scans in which various dyes and two-photon resonances in krypton were used. These are indicated on the spectra by sections labelled (i)-(iii) which represent a combination of the krypton resonances and dyes used to generate the wavenumber range shown. Details of each resonance/dye combination are provided on the appropriate figure caption.

The excitation functions for I^+ and Cl^- have been recorded above the $(^3P_2)$ ion-pair threshold using a synchrotron source[4]. In a similar experiment to that reported for I_2, the two excitation functions were measured to be equivalent to a first approximation and ion-pair formation from ICl was deduced. A very simple spectrum was observed, again at variance with the highly structured spectrum recorded in the present work. Assignments to Rydberg states and associated vibronic structure were made by comparison with the high-resolution one-photon absorption spectrum, allowing for a systematic error in the wavenumber positions of 350±50 cm^{-1}. Similar conclusions were drawn from the synchrotron excited free ion excitation spectrum on ion-pair formation from both I_2 and ICl, involving a selective predissociation mechanism for the Rydberg states in each molecule. In the case of ICl it was proposed that the $ns\sigma$ Rydberg states, on each ionic core, were most efficiently coupled to the ion-pair continuum. Comparing these conclusions to those in the present work, it is again found, as in the case of I_2, that under high-resolution conditions the entire spectrum, seen in absorption, is reproduced using the method of detecting ion-pair formation. The dominant features in this spectrum, and hence also the absorption spectrum, are transitions to the [3/2];4f and [1/2];4f Rydberg states.

5.3.2 Assignment of Rydberg states

The Rydberg state assignments made in this work follow the propensity rules derived from the overall reassessment of one- and two-photon transitions to Rydberg states in the halogens and interhalogens.

Before assigning Rydberg states observed in the wavenumber range covered in the present experiment, both the one-photon absorption and [2+1] REMPI spectra were examined again in order to establish a pattern of Rydberg state components in terms of their effective quantum numbers. Each component, for any value of n, has a reasonably well-defined quantum defect, δ, thus allowing a Rydberg series in nl; Ω to be identified in terms of the effective quantum numbers ($n^* = n - \delta$) of the components. This information was then used to extend the range of assignments up to the first ionization limit (ICl^+, $^2\Pi_{3/2}$). Effective quantum numbers were calculated using the Rydberg equation with IP's accurately determined by ZEKE-PFI photoelectron studies[19] to be 81 246 cm^{-1}. The spin-orbit splitting energy between this and the higher energy component of the ion (Ω_c=3/2) has been determined[20] by conventional photoelectron spectroscopy to be 4 678 cm^{-1}, making $IP([1/2]_c)$=85 924 cm^{-1}.

ionic core (Ω_c)	Rydberg state	$n-\delta$	ν_{00}/ cm^{-1}	v'=1
[3/2]	8s	4.15	74 860	75 269
	9s	5.12	77 045	
	10s	6.18	78 321	
	11s	7.20	79 056	
	12s	8.21	79 543	
[1/2]	8s	4.12	79 424	79 852

Table 5.1: Term values and effective quantum numbers for the *n*s Rydberg series convergent on the Ω_c=3/2 and 1/2 ionic cores.

Several Rydberg states have been assigned in the wavenumber range covered. For clarity, the assignments, band positions and effective quantum numbers of each Ω component of each state have been tabulated according to the l value of the Rydberg state, i.e. *n*s, *n*p, *n*d and *n*f states in separate tables. The data is presented in tables 5.1-5.4. The states have been ordered according to their quantum defect value and, for states with more than one Ω component which can be defined, i.e. the *n*p and *n*d states, the expected Ω value is assigned. These assignments are labelled on the spectra presented in figures 5.1 to 5.3.

ionic core (Ω_c)	Rydberg state	$n-\delta$	ν/ cm^{-1}
[3/2]	8p; 1	4.54	75 924
	8p; 0	4.61	76 090
	9p; 1	5.51	77 626
	10p; 1	6.47	78 622
	10p; 0	6.50	78 648
	11p;	7.51	79 300
	11p;	7.56	79 324
	12p; 1	8.54	79 740
	12p; 0	8.58	79 755
	13p;	9.51	80 032
[1/2]	7p; 1	3.51	77 070
	7p; 0	3.57	77 357

Table 5.2: Term values and effective quantum numbers for the np Rydberg series convergent on the Ω_c=3/2 and 1/2 ionic cores.

ionic core (Ω_c)	Rydberg state	$n-\delta$	ν/ cm^{-1}	v'=1	v'=2
[3/2]	6d; 1	3.73	73 321		
	6d; 1	3.89	73 944		
	6d; 0	4.00	74 366	74 802	
	7d; 1	4.76	76 407		
	7d; 0	4.96	76 783		
	8d; 1	5.70	77 872		
	8d; 0	5.99	78 190		
	9d; 1	6.72	78 813		
	9d; 0	6.97	78 989		
	10d; 1	7.65	79 369		
	10d; 0	7.89	79 483		
	11d; 1	8.69	79 794		
	11d; 0	8.96	79 878		
	12d; 1	9.64	80 065		
	12d; 0	9.96	80 140		
[1/2]	5d; 1	2.81	72 085	72 519	72 926
	5d; 0	2.93	73 105		
	6d; 1	3.71	77 925	78 357	
	6d; 0	3.97	78 938		

Table 5.3: Term values and effective quantum numbers for the nd Rydberg series convergent on the Ω_c=3/2 and 1/2 ionic cores.

ionic core (Ω_c)	Rydberg state	$n-\delta$	ν/ cm^{-1}	v'=1	v'=2	v'=3
[3/2]	4f;	3.78	73 558	73 987		
	4f;	3.91	74 062	74 474		
	4f;	4.03	74 485	74 905	75 312	
	5f;	4.83	76 533			
	5f;	4.96	76 647			
	5f;	5.04	76 931			
	6f;	5.81	77 996			
	6f;	5.95	78 144			
	6f;	6.01	78 211			
	7f;	6.78	78 857			
	7f;	6.92	78 955			
	7f;	7.04	79 031			
	8f;	7.88	79 478			
	8f;	8.01	79 537			
	9f;	8.87	79 852			
	9f;	9.06	79 909			
	10f;	9.85	80 115			
	10f;	10.07	80 164			
[1/2]	4f;†	3.80	78 375	78 794	79 201	79 603
	4f;	3.90	78 683	79 120	79 561	79 990
	4f;	4.06	79 243			
	4f;	4.08	79 294	79 720		

Table 5.4: Term values and effective quantum numbers for the nf Rydberg series convergent on the Ω_c=3/2 and 1/2 ionic cores. The † indicates an extra triplet component observed for states with the lowest n of the nf series, i.e. n=4.

5.3.3 Isotope shifts

As a further aid to assignment, the identity of certain bands as electronic origins was confirmed by comparing an isotopically mixed mass-resolved spectrum and one which was isotopically pure. Ion functions due to $I^{35}Cl$ and $I^{37}Cl$ were obtained from spectra recorded on the I^+ mass channel, since this ion has only one abundant isotope and is common to both isotopomers of the molecule. These were compared with spectra recorded on the $^{35}Cl^+$ mass channel, effectively a pure isotopomer. Hence, extra peaks, lying to lower wavenumber by a well-defined shift, in the I^+ ion excitation function were considered to be due to vibrational progression members of the Rydberg states of $I^{37}Cl$, since the heavier isotopomer is expected to possess a lower vibrational frequency. The expected shift was calculated using the expression relating the force constant of a molecule to its vibrational frequency and reduced mass ($\omega=\sqrt{k/\mu}$). Assuming the force constant, k, is similar for both isotopomers, the expression becomes that in equation (2).

$$\frac{\omega_{I^{35}Cl}}{\omega_{I^{37}Cl}} = \sqrt{\frac{\mu_{I^{37}Cl}}{\mu_{I^{35}Cl}}} \tag{5.1}$$

Effectively, $\omega_{I^{37}Cl}$ was calculated using known values for $\omega_{I^{35}Cl}$, $\mu_{I^{35}Cl}$ and $\mu_{I^{37}Cl}$. Wavenumber shifts, depending on the observed fundamental vibrational frequency of a particular Rydberg state of the $I^{35}Cl$ isotopomer, were calculated to be around 9 cm^{-1} for v'=1 and around 18 cm^{-1} for v'=2 progression members. Bands showing no shifted peak in the I^+ mass-resolved ion excitation func-

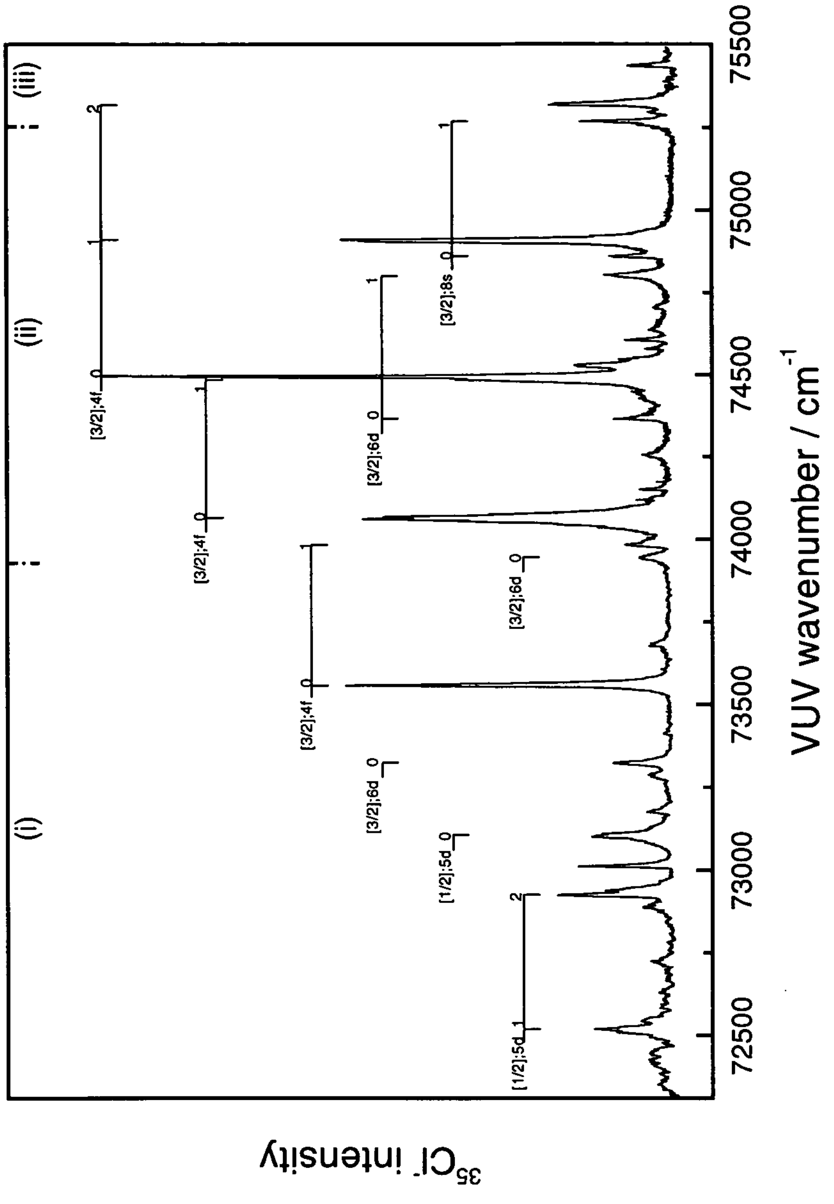

Figure 5.1: Ion excitation function from ICl recorded on ^{35}Cl$^-$ mass channel in wavenumber range 72 500-75 500 cm^{-1}. The following Kr resonance/dye combinations were used; (i) $[5/2]_2$/C307, (ii) $[1/2]_0$/C307 and (iii) $[1/2]_0$/C153.

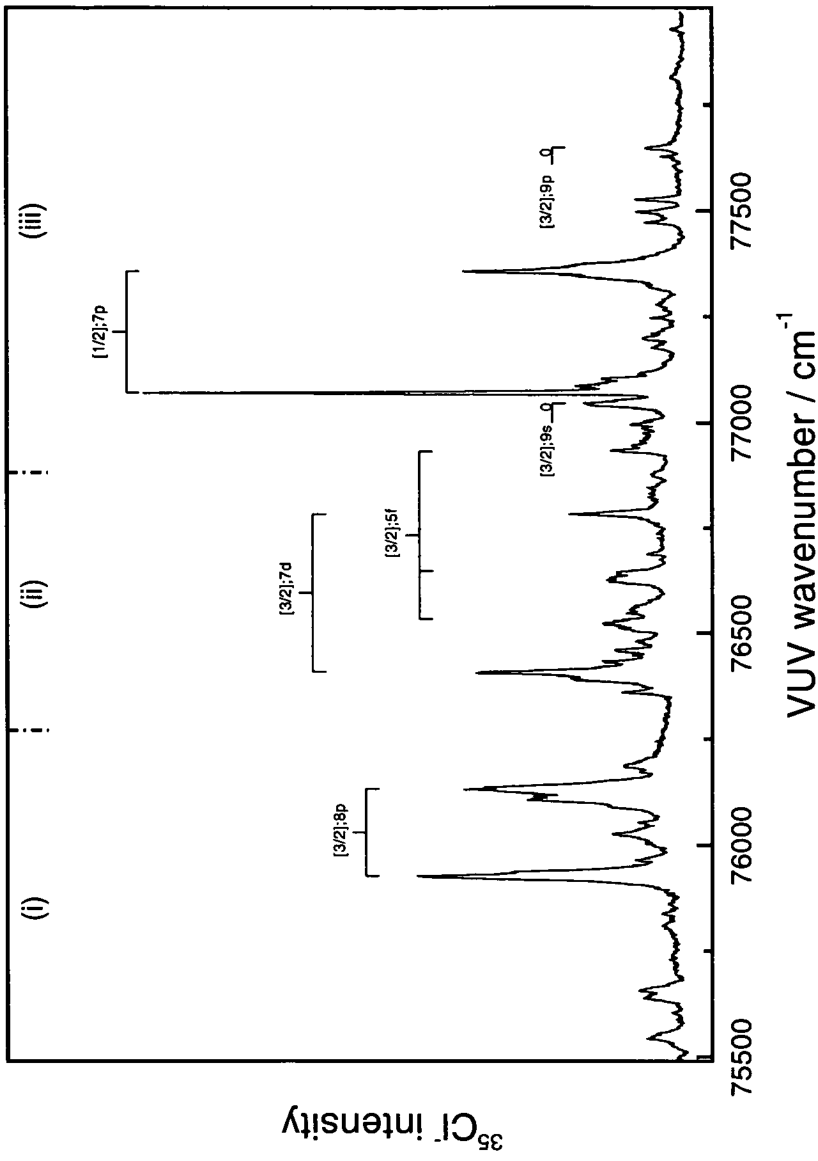

Figure 5.2: Ion excitation function from ICl recorded on $^{35}Cl^{-}$ mass channel in wavenumber range 75 500-78 000 cm^{-1}. The following Kr resonance/dye combinations were used; (i) $[1/2]_0$/C307, (ii) $[5/2]_2$/R101 and (iii) $[3/2]_2$/R101.

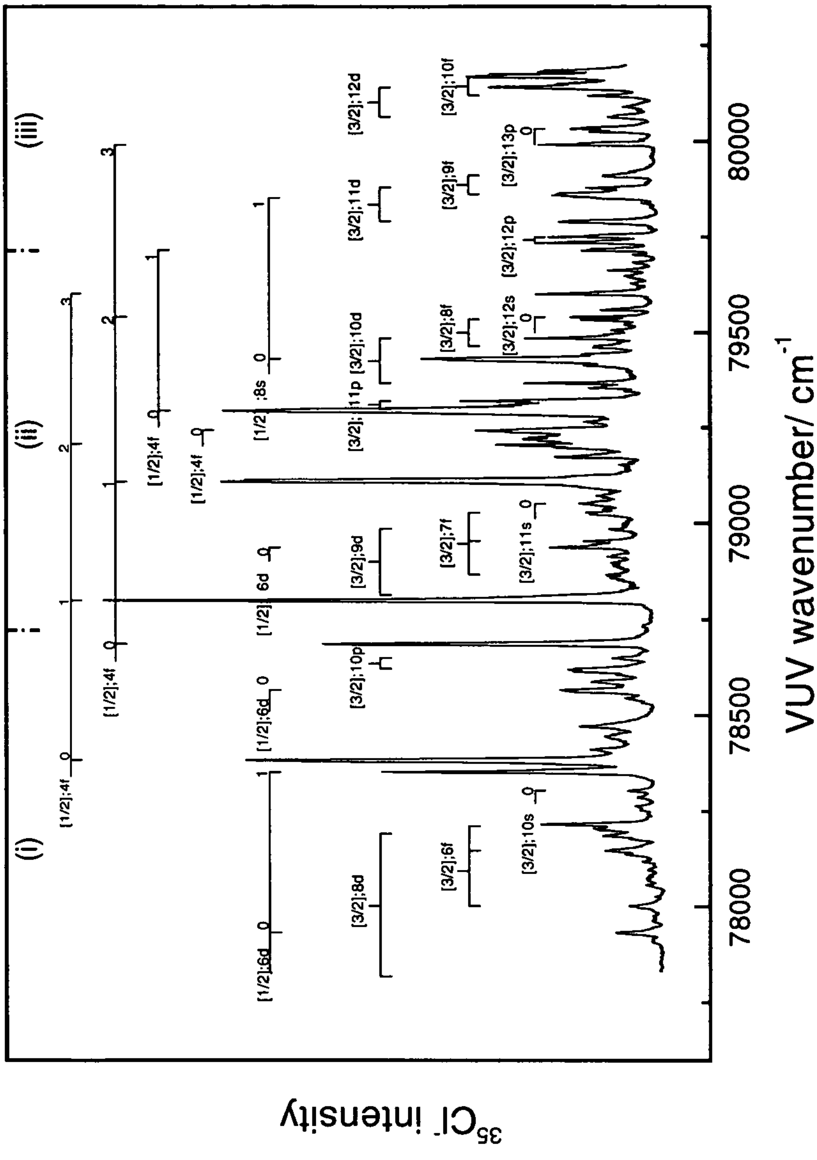

Figure 5.3: Ion excitation function from ICl recorded on $^{35}Cl^-$ mass channel in wavenumber range 78 000-80 300 cm^{-1}.. The following Kr resonance/dye combinations were used; (i) $[1/2]_0$/R101, (ii) $[3/2]_2$/R700 and (iii) $[1/2]_0$/R700.

tion were confirmed as Rydberg state origins. Similarly, vibrational progression members and vibrational quanta were identified by the magnitude of the shift observed.

5.3.4 Predissociation mechanism of Rydberg states

A number of studies have been made of the interaction between Rydberg states and bound levels of the ion-pair states of ICl, at energies below the first ion-pair threshold, using a variety of one- and two-photon excitation methods.

In the one-photon synchrotron spectrum[7], Rydberg states are seen strongly in absorption but are conspicuously absent in the fluorescence excitation spectrum, due to heavy predissociation by one or more repulsive states. A strong absorption into the $E0^+$ ion-pair state is observed in the synchrotron spectrum as an unresolved profile, rising in intensity with a sharp fall-off in the vicinity of the [3/2]6p; 1 Rydberg state at around 160 nm. Sharp, intense structure due to the spin-orbit split components of the 6s Rydberg state ([3/2]6s; 1 and [1/2]6s; 0, 1) is superimposed on this background to longer wavelength.

In questioning the predissociation mechanism of Rydberg states above the ion-pair threshold, into unbound ion-pairs, comparisons are drawn from the bound-

ion-pair state(Ω)	configuration $[ijkl]$
$E0^+$	[1441]
$\beta 1$	[2332]/[2431]†

Table 5.5: Ion-pair states involved in predissociation mechanism of Rydberg states of ICl. † indicates that the β state is a mixture of two configurations.

bound interactions comprehensively discussed in reference [7]. The important features include the nature of the predissociation; whether homogeneous or heterogeneous. It has been determined that in experiments which employ jet-cooling of a sample molecule the subsequent data generally do not provide information on rotationally dependent processes such as heterogeneous interaction or predissociation, since only a limited number of J levels are populated in transitions.

However, from the assignments presented in the current work we may neglect a heterogeneous mechanism based on the above observation. A suitable ion-pair state with Ω=1, in the lowest tier, exists which, although is essentially forbidden by direct one-photon absorption owing to the electronic configuration of the state requiring movement of two electrons, may nevertheless homogeneously predissociate Rydberg states with Ω=1 *via* two-electron exchange. This state has been labelled as the $\beta 1$ ion-pair state[18,21], which lies in close proximity with the observable $E0^+$ ion-pair state. The configurations of the $E0^+$ and $\beta 1$ ion-pair states are listed in table 5.5.

The predissociation mechanism for ion-pair formation from ICl can be considered to be essentially equivalent to that in I_2, detailed in the previous chapter. In both molecules, Rydberg states are predominantly based on the iodine atom and the same three-stage process from initial excitation from the ground state of the molecule to formation of unbound ion-pairs by predissociation can be applied, with a few exceptions. The process can be described by the following stages.

As an initial step, Rydberg states with Ω=0 or 1 are accessed by one-photon VUV excitation above the first ion-pair threshold. With the loss of g/u symmetry in ICl, *n*s, *n*p, *n*d and *n*f Rydberg states are accessible with one-photon. The same propensity rules determined for one- and two-photon transitions in the halogens and interhalogens apply here also; states with appreciable singlet character are accessed only. This entails one *n*s, two *n*p, three *n*d and three *n*f states on each ionic core, with the usual exceptions applying.

The next stage involves the interaction between the configurations of the Rydberg state and ion-pair state. As in I_2, the repulsive limbs of the high-lying Rydberg states observed and the first tier ion-pair states are in close proximity in $R - E$ space, conferring a good overlap of wavefunctions. Rydberg and ion-pair states homogeneously interact ($\Delta\Omega$=0) at small R through two-electron exchange. With the loss of the g/u symmetry classification in the heternonuclear case presented here, the π_g antibonding orbital in the valence shell becomes effectively a pπ orbital centred on the iodine atom (i.e. the less electronegative halogen atom). The two-electron exchange connecting the Rydberg and ion-pair state configurations does not have to be a dipole-dipole type and is therefore allowed, since the Laporte selection rule does not apply. The relative strengths of the interactions can be deduced by considering whether parallel or perpendicular electronic transitions are involved in the interaction. Finally, unbound ion-pairs, correlating with dissociation products $I^+(^3P_2)$ + $Cl^-(^1S_0)$ are formed as the component ions move apart.

5.4 Conclusion

Using laser radiation with VUV wavelengths, generated by four-wave mixing in krypton gas, in conjunction with time-of-flight mass spectrometry to detect positive and negative ions, several Rydberg states in ICl, lying above the first ion-pair threshold at 72 522 cm^{-1}, have been identified and assigned to *n*s, *n*p, *n*d and *n*f states on both spin-orbit components of the ion. The reproduction of the absorption spectrum by the mass-anlaysed spectra recorded on the I^+ and Cl^- mass channels shows that all Rydberg states in this region are efficiently predissociated.

Using propensity rules developed for one- and two-photon transitions to Rydberg states in the halogens, the Rydberg spectrum of ICl has been largely reassigned. This is attributable in part to using an accurate ionization potential for each ionic core. A predissociation mechanism based on that discussed for ion-pair formation from I_2 has been proposed, with account taken of the loss in g/u symmetry in the heteronuclear halogen case. Vibrational progression members of some of the Rydberg states have also been assigned using isotope shift data to aid identification.

5.5 References

[1] P. Venkateswarlu, *Can. J. Phys.* **53** (1975) 812

[2] P. Venkateswarlu, *Can. J. Phys.* **48** (1970) 1055

[3] P. Venkateswarlu, *Can. J. Phys.* **47** (1969) 2525

[4] D.K. Kela, A.J. Yencha, R.J. Donovan, A. Kvaran and A. Hopkirk, *Organic Mass Spec.* **28** (1993) 327

[5] R.J. Donovan, M.A. MacDonald, K.P. Lawley, A.J. Yencha and A. Hopkirk, *Chem. Phys. Lett.* **138** (1987) 571

[6] A.J. Yencha, D.K. Kela, R.J. Donovan, A. Hopkirk and A. Kvaran, *Chem. Phys. Lett.* **165** (1990) 283

[7] K.P. Lawley, E.A. Kerr, R.J. Donovan, A. Hopkirk, D. Shaw and A.J. Yencha, *J. Phys. Chem.* **94** (1990) 6201

[8] A.J. Yencha, R.J. Donovan, A. Hopkirk and D. Shaw, *J. Phys. Chem.* **92** (1988) 5523

[9] R.J. Donovan, J.G. Goode, K.P. Lawley, T. Ridley and A.J. Yencha, *J. Phys. Chem.* **98** (1994) 2236

[10] R.J. Donovan, R. Flood, J.G. Goode, K.P. Lawley, R.R.J. Maier, T. Ridley and A.J. Yencha, *IOP Conf. Ser.* **128** (1992) 177

[11] R.H. Lipson and A.R. Hoy, *J. Chem. Phys.* **90** (1989) 6821

[12] S.S. Dimov, R.H. Lipson, T. Turgeon, J.A. Vanstone, P.Wang and D.S. Yang, *J. Chem. Phys.* **100** (1994) 8666

[13] P. Wang, S.S. Dimov and R.H. Lipson, *J. Chem. Phys.* **107** (1997) 3345

[14] R.H. Lipson and A.R. Hoy, *Mol. Phys.* **68** (1989) 1311

[15] R.J. Donovan, A.C. Flexen, K.P. Lawley and T. Ridley, *Chem. Phys.* **226** (1998) 217

[16] L. Minnhagen, *Ark. Fys.* **21** (1962) 415

[17] U. Berzinsh, M. Gustaffson, D. Hanstorp, A. Klinkmuller, U. Ljungblad and A.M. Martensson-Pendrill, *Phys. Rev. A* **51** (1995) 231

[18] G.W. King, I.M. Littlewood, R.G. McFadden and J.R. Robbins, *Chem. Phys.* **41** (1979) 379

[19] M.C.R. Cockett, *unpublished results*

[20] A.W. Potts and W.C. Price, *Trans. Farad. Soc.* **67** (1971) 1242

[21] R.H. Barnes, C.E. Moeller, J.F. Kiehen and C.M. Verber, *Appl. Phys. Lett.* **24** (1974) 610

Chapter 6

Production of VUV Radiation by High Harmonic Generation

6.1 Introduction

High-order harmonic generation has been developed in recent years to provide a source of coherent laser radiation with wavelengths extending into the XUV and soft X-ray regions (λ=2.7 nm has been observed) of the electromagnetic spectrum[1]. This advance has been possible through the recent development of ultrashort pulse-length laser systems, on the picosecond or sub-picosecond timescale[2], which has allowed relatively easy access to high intensity laser radiation from a table-top laser source. These sources are able to produce significantly higher peak intensities than conventional (nanosecond) laser sources. Intensities developed are typically of the order 10^{14}-10^{18} W cm^{-2} when focussed, which is necessary for efficient high-order harmonic generation (HG).

This has prompted several groups$^{3-8}$ to study the fundamental aspects of the interaction between high intensity radiation and matter, experimentally. One of the most important applications arising from this research has been in the field of HG.

The high-order HG process is based on the nonlinear polarisation response of atoms and molecules to the strong electric field component of applied radiation. At the light intensities produced at the focus, the electric field component of the radiation can become comparable to or in excess of the atomic Coulomb field of 10^8-10^9 V cm^{-1}. Atoms in a strong field can emit coherent radiation at energies exceeding the ionisation potential. At laser intensities of the order 10^{14}-10^{18} W cm^{-2}, atoms or molecules may scatter incident radiation of input frequency ω yielding radiation at several frequencies equal to odd integer multiples of the fundamental radiation, $n\omega$, where $n \geq 3$.

The most efficient and widely used nonlinear media are the inert gases given their stability, ease of handling and high polarizability. Harmonics are propagated in the same direction as the applied fundamental beam and have similar pulse width characteristics. Discrete harmonics up to the 221st order have been observed using pulsed jets of He[1]. This approach may therefore provide a source of useable short wavelength radiation with picosecond or subpicosecond pulse widths[9,10].

Much of the preliminary experimental work in this area was directed towards characterising the harmonic output in terms of the experimental conditions or parameters used, such as the type of medium, confocal parameter (or beam geometry) and the laser pulse-length. This allowed optimisation of the range of generated harmonics and the conversion efficiency of individual harmonic orders and furthered understanding of the perturbations within the nonlinear medium under such conditions of high intensity and short timescale. Much of the research has been led by two major groups: L'Huillier/Wahlstrom at Saclay/Lund Institute of Technology[10] and Ditmire/Perry[9] at the Lawrence Livermore National Laboratory. These groups have also extended the fundamental research to applications of the high harmonic orders as sources of VUV and XUV radiation for atomic and molecular spectroscopy.

Applications have included measurement of the photoionization cross section of rare gases[9], lifetime measurements of the 2p state in He[11] and recording the photoion excitation spectrum of NO in a region where autoionization resonances are observed[10].

Two sessions were made available to use the Tsunami 50 fs laser system based at the Rutherford-Appleton Laboratory Central Laser Facility. A similar approach to the direction of research into high harmonic generation was employed in a two-phase programme. Results from each experimental session are presented here.

The aim of the first experiment was to generate the third and fifth harmonics in a simple static cell arrangement and to characterise the output in terms of pressure dependence, laser intensity dependence and bandwidth. The aim of the second experiment was to generate and observe harmonics with wavelengths below the transmission cut-off of MgF_2 at 120 nm, by providing a windowless beam path from the interaction or generation region to the detector. This was done by introducing the nonlinear medium into the laser focus *via* a pulsed jet, in order to maintain a high vacuum in a differentially pumped system. Harmonics up to the seventh order were generated in this way and, after optimisation, the photon yield of each harmonic was estimated in order to test the suitability of the technique as a source of short wavelength, VUV radiation for photoionization experiments.

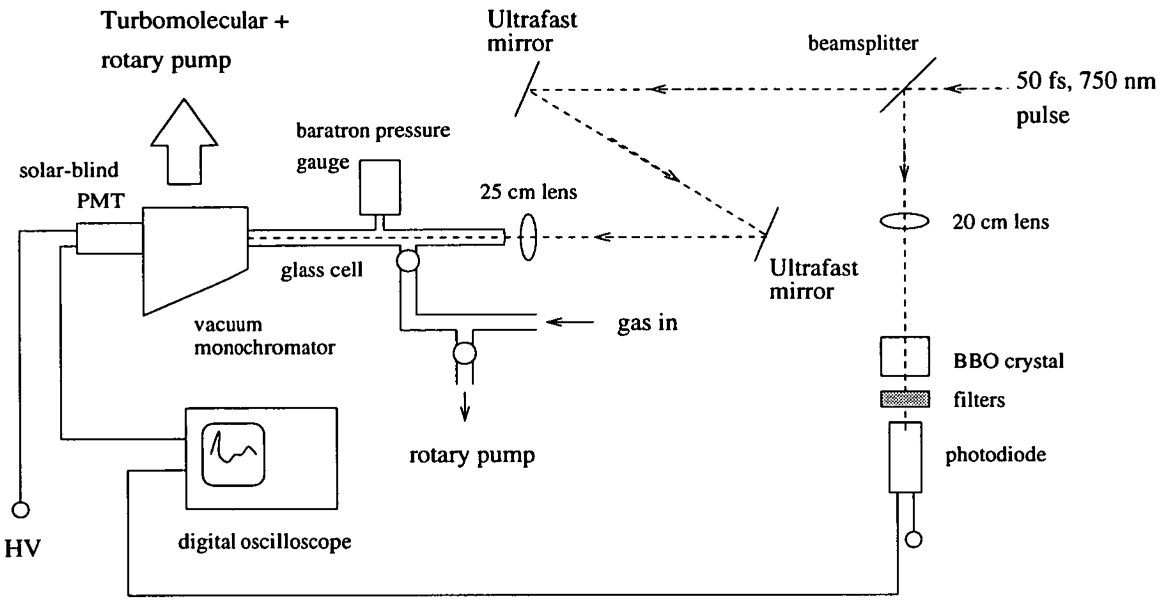

Figure 6.1: Experimental arrangement for generation and detection of harmonics $n \leq 5$. Apparatus consists of a windowed static cell containing nonlinear medium. The exit window was constructed of MgF_2 which has a transmission cut-off wavelength of 120 nm.

6.2 Experimental

6.2.1 Static cell apparatus, harmonics n=3-5

The experimental arrangement is shown on figure 6.1. Fundamental laser radiation (λ=750 nm, 50 fs) was directed and focused into a 30 cm length, 25 mm diameter cell containing the generating medium at pressures up to 760 Torr. Cell pressures were measured using a simple analogue dial gauge or a baratron (Chell) for preliminary experiments measuring cell pressures up to 120 Torr. Argon and xenon gas samples used were from BOC Gases. Harmonics were separated from the fundamental using monochromators and detected with a suitable photomultiplier tube (PMT). Third harmonic radiation at 250 nm was detected using a

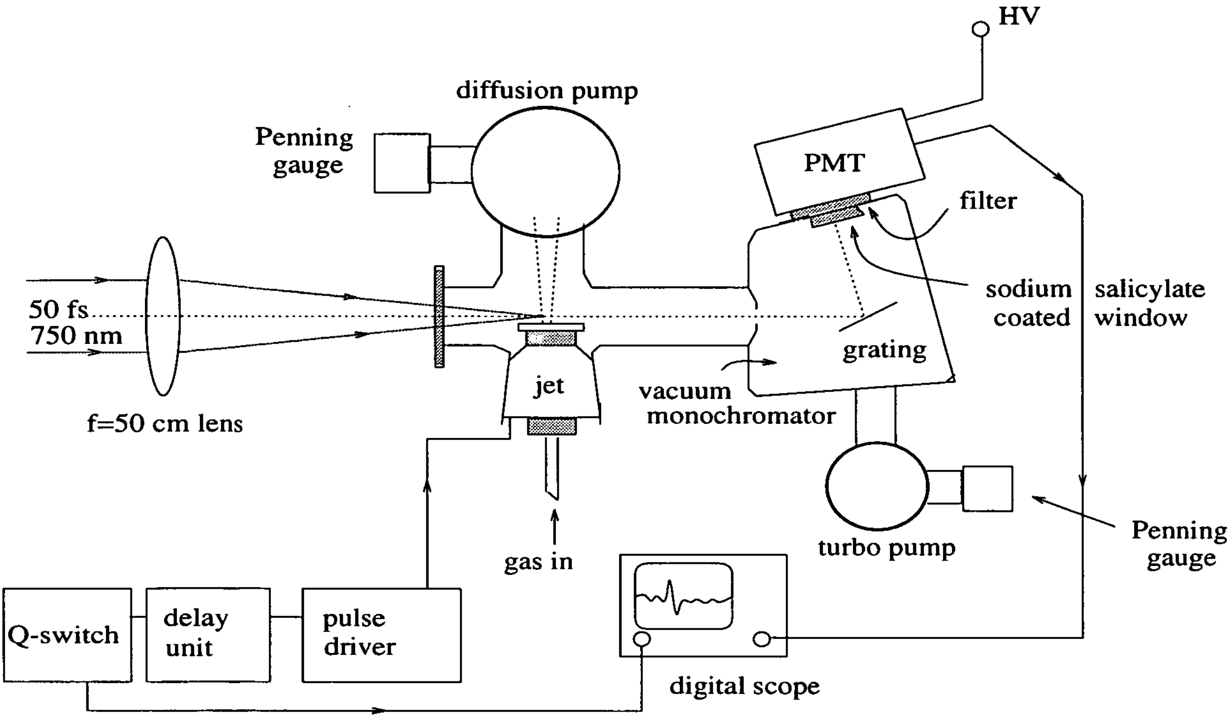

Figure 6.2: Windowless apparatus for harmonic generation and detection with nonlinear medium introduced into interaction region by pulsed jet.

0.25 m monochromator in a Czerny-Turner configuration, with an EMI 9781B PMT. For separation of the 5th harmonic (150 nm) a grating monochromator was used which could be evacuated to $<10^{-6}$ Torr. A solar-blind PMT (Hamamatsu R1459) was used for detection and had effectively no sensititivity to 250 nm or 750 nm light. Signals were amplified at the PMT and measured on a digital oscilloscope (Tektronix). The stability and pulse energy of the fundamental beam was monitored by detecting the second harmonic (375 nm) using a photodiode.

6.2.2 Pulsed jet appartus, harmonics n=3-7

The experimental arrangement is shown on figure 6.2. Laser pulses of around 50 fs pulse length and 10 nJ energy were generated by a CW argon-ion pumped mode-locked titanium sapphire laser in an 82 MHz train. Pulses were amplified in an Nd:YAG pumped dye laser and yielded 750 nm radiation with pulse energy 100 μJ at a repetition rate of 10 Hz. This provided peak intensities, when focussed, of the order 10^{14} W cm^{-2}. Laser radiation was directed and focussed, using a 50 cm focal length lens, into a glass cell close to the output of a pulsed nozzle with diameter 600 μm. The focal point was estimated to be around 200-300 μm from the nozzle. Fundamental and generated radiation was directed on to a concave holographic grating housed in an evacuable monochromator. No windows were present in the beam path between the generation region and grating.

Harmonic wavelengths were selected and directed to the exit window of the monochromator. The window was coated, on the vacuum side, with a thin layer of crystallised sodium salicylate. The compound, sodium salicylate fluoresces at 443 nm and has a high fluorescence quantum yield for a large range of wavelengths extending into the XUV region (from 400 nm to as low as 3 nm has been observed). A UV-visible photomultiplier with a peak response around 440 nm (EMI 9664B) was placed at the exit window with a BG18 filter in front which gave 60% transmission at 443 nm and effectively zero transmission at 250 nm and 750 nm. The 443 nm fluorescence was detected by the PMT and the signal output to the digital oscilloscope.

A high vacuum was maintained in the system by differentially pumping using a diffusion/rotary pump with cold trap removing the gas pulses and a turbo/rotary pump evacuating the monochromator, yielding a pressure in the system of $<10^{-6}$ Torr. The jet was triggered from the synchronous Q-switch output of the Nd:YAG laser. An initial delay of 100 ms between successive pulses was generated followed by optimisation of the timing between the valve opening and the gas pulse reaching the laser focus. The optimum time delay was found to be 750 μs between these events. A backing pressure of around 6 atm was used in the jet.

6.3 Results & Discussion

6.3.1 Harmonic output from static cell experiment

The main aims of the work using the femtosecond laser system at the Rutherford-Appleton Laboratory Central Laser Facility were to determine the optimum experimental conditions for generating high-order harmonics, to estimate the number of photons for each harmonic pulse and to study the characteristics of the generated radiation under variable experimental conditions. Several gases were tested as possible nonlinear media including xenon, argon, helium and nitrogen, however only xenon and argon were found to be suitable. The nonlinear medium was contained within a static cell environment, hence only harmonics with a wavelength greater than the transmission cut-off wavelength of the window material, forming the exit of the cell, could be observed. In this case n=5 (λ=150 nm) was the highest observable harmonic order, using an MgF_2 exit window ($\lambda_{cutoff} \simeq$110 nm).

Each harmonic order observed was detected readily by tuning the grating of either monochromator to roughly the desired position. Subsequent, preliminary optimisation of the harmonic signal involved careful alignment of the fundamental beam, through narrow entrance slits on the monochromator, followed by finely tuning the grating position for maximum signal. With this procedure completed, the apparatus was then prepared for further optimisation and characterisation experiments on the harmonic pulses.

Characterisation of the output harmonic pulses was divided into three sections corresponding to the dependence of the harmonic signal on three variable experimental parameters: (1) pressure of the medium in the cell, (2) intensity of the incident fundamental beam at the focus and (3) the grating position, dispersing the harmonic pulse.

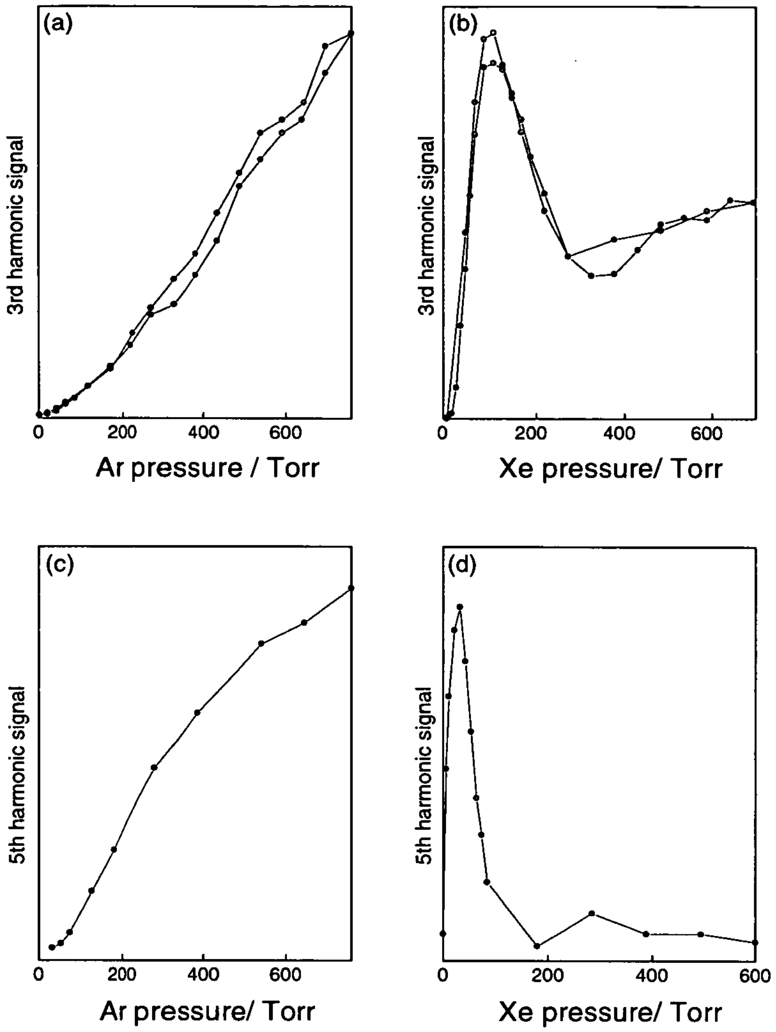

Figure 6.3: Variation of harmonic signal with cell pressure (Torr) for 3rd and 5th harmonics in argon and xenon.

Pressure dependence

Harmonic signals were measured at various pressures up to 1 atm (760 Torr) in both argon and xenon, for both 3rd and 5th harmonics. This allowed the optimum number density of atoms presented at the laser focus to be determined and furthermore, to obtain the best signal in either medium for the various other characterisation experiments.

The graphs shown in figures 6.3(a)-(d) show plots of the 3rd and 5th harmonic signals varying with pressure (of argon and xenon) up to 760 Torr. The plots for argon (figures 6.3(a) and 6.3(c)) show a continuously rising pressure-intensity relationship, for both harmonic orders, whereby the optimum output was reached at the highest measureable pressure of the medium in the cell. The equivalent plots for xenon (figures 6.3(b) and 6.3(d)), obtained under the same conditions of focussing and laser power show a very different pressure-intensity relationship. The third harmonic signal exhibited a maximum at *ca.* 100 Torr (figure 6.3(b)), before falling to a minimum around 350 Torr and slowly rising again up to the measureable limit at 760 Torr. The maximum and minimum turning points on this plot indicate that another pressure dependent competing process is occuring which inhibits HG in Xe over a range of cell pressures and is most efficient around 350 Torr. This may be ascribed to either multiphoton ionisation of Xe atoms or plasma formation at some critical density, both of which reduce the conversion efficiency of harmonic generation. Xenon was found to be the more efficient medium for conversion to the third harmonic, with a factor of 100 increase in the PMT signal measured relative to argon under conditions of optimum pressure in both gases.

Similarily, the fifth harmonic in xenon attained a maximum intensity at 30 Torr, before falling to effectively zero intensity above 200 Torr. The low measured intensity of the fifth harmonic, generated in xenon, was thought to be due to another pressure-dependent signal, detected at 156 nm which overlapped with the spectral bandwidth of the fifth harmonic at 150 nm. Figures 6.4(a)-(e) show plots of PMT signal versus monochromator grating position at different pressures, ranging from 10 to 110 Torr. As the pressure was increased, a second peak, centred around 156 nm, became progressively more intense relative to the peak due to the 5th harmonic. The measured intensity of the 156 nm emission became greater than that of the 5th harmonic at cell pressures greater than 50 Torr.

The origin of this emission is uncertain but, given the specificity to xenon only, would appear to originate from a transition from a high-lying state in the xenon atom or dimer. No atomic levels in xenon can account for a transition with this energy ($\Delta\nu$= 64 100 cm^{-1})[12]. The xenon dimer, which exists only as an excited molecule, Xe_2^*, has been reported to fluoresce at wavelengths, $\lambda \geq 155$ nm, corresponding to an emission from the 6s; $0u^+$ or 1u states[13]. The exciting source

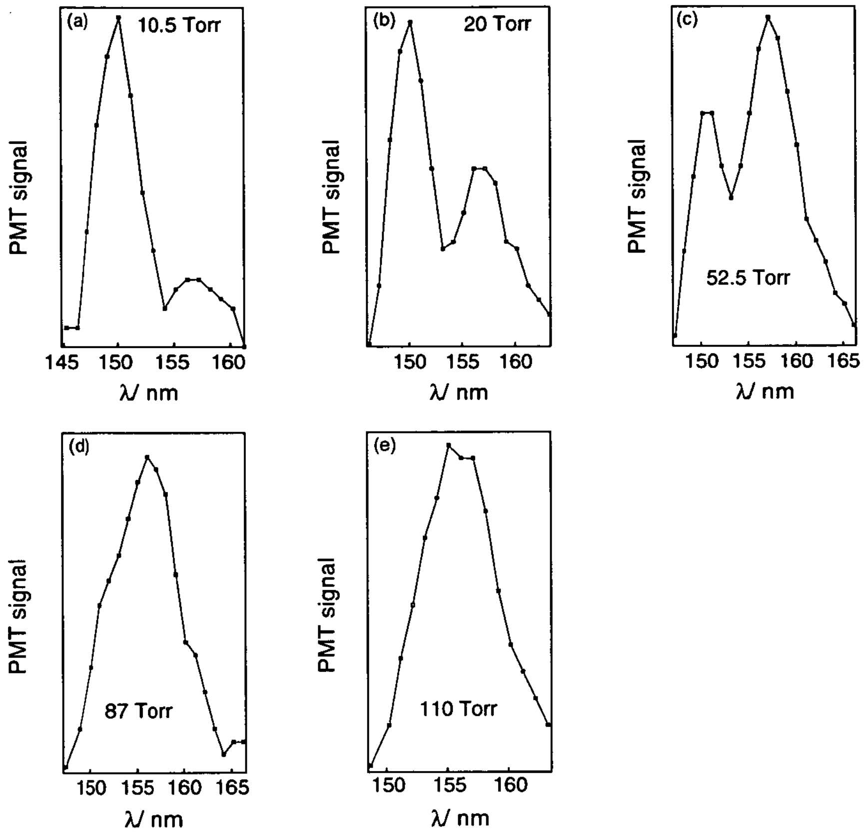

Figure 6.4: Bandwidth profiles of 5th harmonic and 156 nm emission in Xe at various cell pressures.

for this fluorescent emission may either be due to the generated fifth harmonic or a multiphoton excitation process of the applied 750 nm fundamental. However, any residual fluorescence from such a species would not be expected to exhibit an intensity greater than the exciting source, unless the source was absorbed over a long path length of the medium. This would tend to favour the fifth harmonic as the exciting source, since the xenon dimer absorbs strongly around 151 nm which lies within the bandwidth of the 150 nm pulsed output.

The differences in the pressure dependence relationships in xenon compared to argon are expected by considering the physical properties of each atom. Xenon is by far the more polarizable, hence is more likely to exhibit a greater harmonic conversion efficiency and to produce excited dimers. Xenon also has a much lower ionization potential than argon and hence is more likely to ionize or form a plasma through removal of electrons by a multiphoton process. Plasma formation, MPI and dimer formation are pressure dependent processes which appear to influence the form of the pressure dependence functions of the output of the third and fifth harmonics, shown on figure 6.3.

750 nm laser energy dependence

The laser power dependence on harmonic output was measured under conditions of optimum pressure in xenon and grating position for both the third and fifth

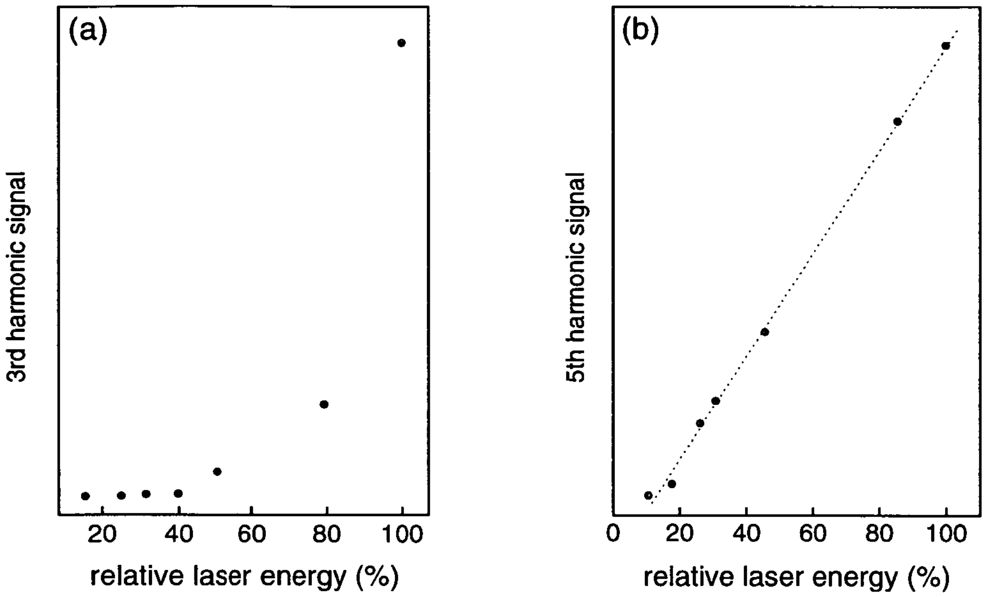

Figure 6.5: Variation of a) third harmonic intensity and b) fifth harmonic intensity with relative laser energy.

harmonic orders. Fundamental laser power was varied by systematic attenuation of the beam using a series of neutral density (ND) filters. The focussing conditions of the fundamental beam were also varied separately to determine the optimum intensity conditions for HG. Fluctuations in the power output of the fundamental laser pulses required significant averaging of the detector signal of up to 50 shots.

Figures 6.5(a) and 6.5(b) show the intensity variation of the third and fifth harmonics, respectively, in xenon, plotted against the relative laser energy of the 750 nm fundamental, expressed as a percentage. The third harmonic showed a

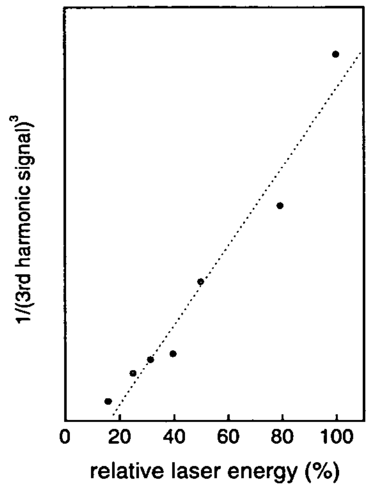

Figure 6.6: Plot of the inverse of the cube of the measured third harmonic signal plotted against relative laser energy. Graph shows cubic dependence of third harmonic intensity on laser energy.

cubic dependence on the laser energy and is shown on figure 6.6 as a linear plot of the reciprocal of the cube of the third harmonic against relative energy. The fifth harmonic showed a linear dependence with laser energy which suggested that the plateau of harmonics had been reached. The plateau region is a characteristic of high harmonic spectra where the intensities of harmonics vary linearly with input laser energy.

The focussing conditions were also varied in order to determine the optimum intensity of the fundamental beam. A 25 cm focal length lens was found to satisfy this condition. Shorter focal length lenses (10 cm) promoted plasma formation, while longer focal lengths (50 cm) reduced the conversion efficiency of HG. The

Harmonic	No. of photons	Conversion efficiency
3rd	$1\text{x}10^{8}$	$2\text{x}10^{-6}$
5th	$5\text{x}10^{4}$	$1\text{x}10^{-10}$

Table 6.1: Number of harmonic photons per pulse generated in Xe in a static cell and corresponding conversion efficiency.

peak intensity developed using a 25 cm lens was estimated to be *ca.* 5x10^{14} W cm^{-2}.

An estimate of the number of photons of each harmonic was calculated using the highest recorded PMT signals for harmonics generated in Xe under optimised conditions of pressure and laser intensity. A detection efficiency of 5% was assumed due to losses in the optics and monochromator. Table 6.1 contains the estimated number of photons and the corresponding conversion efficiency.

Harmonic wavelength dependence

Accurate measurements of the bandwidth of each harmonic were obtained using the Acton vacuum monochromator, utilising the precise grating control and variable slit adjustment of this instrument. The resolution of the grating was tested to provide an estimate of the instrument bandwidth of the monochromator when the entrance and exit slits are set to a width typical of those used for experiments involving detection of high harmonic orders. A mercury lamp was placed at the entrance to the monochromator with the entrance and exit slits set

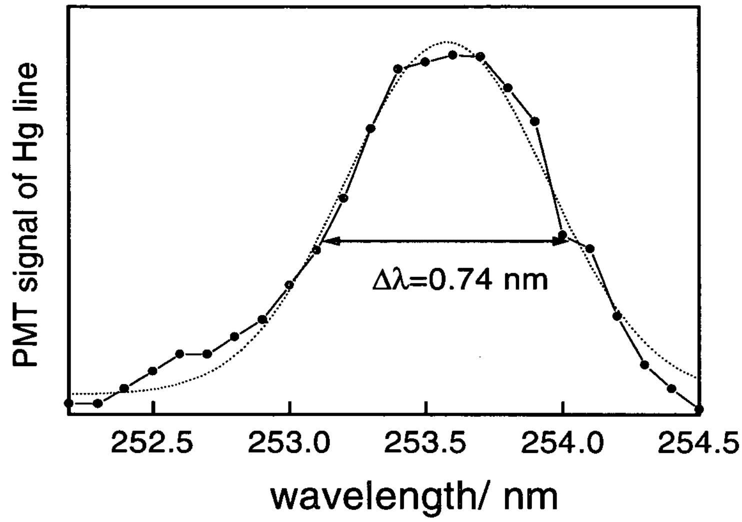

Figure 6.7: Bandwidth profile of 253.7 nm emission line from Hg lamp resolved by grating of 0.25 m vacuum monochromator. The plot shows the instrument bandwidth of the monochromator with slit separations of 0.1 mm.

to 0.1 mm. The grating position was set to disperse the 253.7 nm line in mercury and a bandwidth profile was obtained by recording the PMT signal of this line, at various grating positions to the red and blue of this wavelength. Figure 6.7 shows the wavelength dependence of the monochromated output. From this plot. the resolution or instrument bandwidth of the monochromator, using a typical slit-width of 0.1 mm, was deduced to be 0.74 nm.

The bandwidths of harmonic pulses were measured in a similar way and profiles of the third and fifth harmonics are shown on figures 6.8(a) and 6.8(b), respectively. Typically, the harmonic pulses possess a bandwidth of *ca* 3.5 nm,

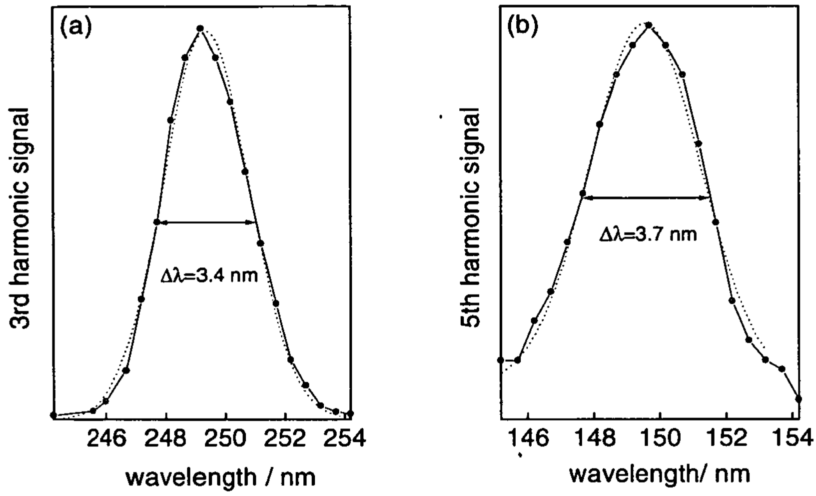

Figure 6.8: Bandwidth profiles of a) 3rd harmonic and b) fifth harmonic pulses generated in Xe and Ar respectively.

determined from the plots. However, accounting for the resolution of the grating of the monochromator an error of ±0.37 nm should be included with this result.

In the transform limit determined by the time-bandwidth equation $\Delta\nu\Delta\tau$=0.4, the pulse widths of the third and fifth harmonics were calculated to be 25±4 fs and 8.2±1.5 fs respectively. These results are in agreement with previous work on the temporal parameters of high-order harmonics, which are found to have pulse durations shorter than the generating source[14].

Harmonic	No. of photons	Conversion efficiency
3rd	$4\text{x}10^{11}$	$1\text{x}10^{-3}$
5th	$2\text{x}10^{9}$	$5.6\text{x}10^{-6}$
7th	$1.6\text{x}10^{6}$	$4.2\text{x}10^{-9}$

Table 6.2: Number of harmonic photons per pulse generated in Xe in a pulsed jet and windowless experimental arrangement and corresponding conversion efficiency.

6.3.2 Harmonic output from pulsed jet experiment

The main aim of the work was to generate and observe harmonic radiation with wavelengths below the transmission cut-off of magnesium fluoride at 110 nm. This was successful up to the 7th harmonic at 107 nm. Xenon and argon gases were used as nonlinear media with xenon found to be the more efficient. Table 6.2 shows the number of photons per pulse generated for each harmonic and the corresponding conversion efficiency relative to a 100 μJ pulse of 750 nm fundamental radiation.

The values for conversion efficiency reported here compare well with the results from other work performed on quantifying harmonic yields[9]. However, a number of assumptions were made in the calculations used to derive these values and therefore an uncertainty of 50% should be included. Comparison with our previous work, generating harmonics in a static cell, shows that a very large increase in yield has been obtained (a factor 10^3 increase for the 3rd and a factor 10^5 increase for the 5th harmonics. The large increase at the 5th harmonic is possibly due to the absence of a long path length, in the jet system, of Xe which absorbs, in its excited dimer form, around 150 nm).

Optimisation was performed on the 3rd harmonic signal by varying the position of the laser focus in the direction of the atomic beam. In this way the gas density profile was mapped and the optimum distance from the nozzle output determined. It was found that the signal decayed exponentially to effectively zero over ca. 2 mm distance. A simple backing pressure versus intensity relationship was derived. The backing pressure of Xe was varied from 0.2 to 6 atm and an approximately linear dependence on the 3rd harmonic signal was observed.

Photon yields and conversion efficiencies were calculated using data on the specification of the PMT and grating and by estimating the efficiency of the fluorescent (sodium salicylate) screen. The results given in table 6.2 correspond to the estimated number of harmonic photons generated at the laser focus.

6.4 Conclusion

The feasibility of using relatively simple experimental arrangements to generate high order harmonics, with the nonlinear medium contained within a static cell environment or introduced to the laser focus by a pulsed jet, has been demonstrated. The first phase of the work performed using the Tsunami 50-fs laser system at the RAL-CLF involved characterising and optimising harmonic output generated in argon and xenon. The pressure dependence of the harmonic output in argon and xenon were widely different, with the form of the relationship in xenon thought to be due to competing pressure dependent processes including MPI, plasma formation and dimer formation.

The relationship between input (fundamental) laser energy and harmonic output was also examined. The third harmonic was found to be vary as the cube of laser energy, while the fifth harmonic varied linearly with laser energy. This latter may suggest that the fifth harmonic is the first member of the plateau region in the harmonic spectrum, where all harmonics vary in a similar manner with input laser energy.

Bandwidths of the third and fifth harmonics were measured. As expected from previous results, the calculated pulse widths, assuming a Fourier transform limited pulse, were shorter than the generating pulse (50 fs).

The second phase, using a windowless setup to allow higher harmonics to be observed ($n \geq 7$) with the nonlinear medium introduced as a pulsed jet, used the optimum conditions derived from the static cell work to attempt to improve the harmonic yield and extend the range of harmonic orders. This was successful up to the seventh harmonic. Furthermore, the large photon yields observed for harmonics n=5 and 7 was encouraging for future work, using the technique as a source of short wavelength, VUV or XUV laser radiation. Harmonic yields and conversion efficiencies were comparable to reported results where high order harmonics were used for spectroscopic applications.

6.5 References

[1] Z.H. Chang, A. Rundquist, H.W. Wang, M.M. Murnane and H.C. Kapteyn, *Phys. Rev. Lett.*, **79** (1997) 2967

[2] G. Mourou and D. Umstadter, *Phys. Fluids B*, **4** (1992) 2315

[3] C.-G. Wahlstrom, *Physica Scripta*, **49** (1994) 201

[4] K. Miyazaki, *J. Nonlinear Opt. Phys. & Mat.*, **4** (1995) 567

[6] T. Ditmire, J.K. Crane, H. Nguyen, L.B. DaSilva and M.D. Perry, Phys. Rev. A, **51** (1995) R902

[7] S.L. Chin, Y. Liang, S. Augst, P.A. Golovinski, Y. Beaudoin and M. Chaker, *J. Nonlinear Opt. Phys. & Mat.*, **4** (1995) 667

[8] A. L'Huillier, P. Balcou and L.A. Lompre, *Phys. Rev. Lett.*, **68** (1992) 166

[9] P. Balcou, P. Salieres, K.S. Budil, T. Ditmire, M.D. Perry and A. L'Huillier, *Z. Phys. D*, **34** (1995) 107

[10] P. Erman, A. Karawajczyk, E. Rachlew-Kallne, E. Mevel, R. Zerne, A. L'Huillier and C.-G. Wahlstrom, *Chem. Phys. Lett.*, **239** 6

[11] J. Larsson, E. Mevel, R. Zerne, A. L'Huillier, C.-G. Wahlstrom and S. Svanberg, *J. Phys. B. Lett.*, **28** (1995) L53

[12] C.E. Moore, *Atomic Energy Levels*, Vol. 3, Natl. Bur. Std. (1971)

[13] A.V. Kanaev, T. Moller and P. Gurtler, *Chem. Phys.*, **177** (1993) 297

[14] A. L' Huillier, T. Auguste, P. Balcou, B. Carre, P. Monot, P. Salieres, C. Altucci, M.B. Gaarde, J. Larsson, E. Mevel, T. Starczewski, S. Svanberg, C.-G. Wahlstrom, R. Zerne, K.S. Budil, T. Ditmire and M.D. Perry, *J. Nonlinear Opt. Phys. & Mat.*, **3** (1995) 647

University Regulations

Whilst pursuing postgraduate research at the Department of Chemistry at the University of Edinburgh I have attended the following lecture courses:

(i) Numerical Data Handling, Postgraduate lectures

(ii) IR Spectroscopy, Practice and Theory, Postgraduate lectures

(iii) Physical Section colloquia 1994-98

In addition I have attended the following conferences:

(i) ECAMP 5, University of Edinburgh, April 1995

(ii) RSC Faraday Division, "Dynamics of Electronically Excited States", University of Manchester, March 1995

(iii) RSC Annual Chemical Congress, Heriot-Watt University April 1995

(iv) RSC High Resolution Spectroscopy Group Annual Meeting, University of Reading 1995

(v) Laser Support Facility Users Meeting, Rutherford-Appleton Laboratory, 1996

(vi) University of Edinburgh Laser Group seminars, 1994-1998

(vii) Annual Meeting of the Physical Section of the Department of Chemistry, University of Edinburgh at Firbush Point Field Centre, June 1995/96/97.

List of Publications

Harmonically Generated VUV Wavelengths Using 50 fs Pulsed Laser Radiation

A.C. Flexen, R.J. Donovan, R.R.J. Maier, A.J. Langley and W. Shaikh, *Rutherford Appleton Laboratory Annual Report* (1995-96) 141

VUV Laser Radiation by High Order Harmonic Generation

A.C. Flexen, R.J. Donovan, A.J. Langley and W. Shaikh, *Rutherford Appleton Laboratory Annual Report* (1996-97) 149

The [2+1] REMPI Spectroscopy of Jet-Cooled Br_2

R.J. Donovan, A.C. Flexen, K.P. Lawley and T. Ridley, *Chem. Phys.* **226** (1998) 217

The VUV Spectroscopy of I_2, Br_2 and ICl; a Re-analysis of the One-Photon Absorption and Free Ion Excitation Spectra

R.J. Donovan, A.C. Flexen, K.P. Lawley, R.R.J. Maier, A. Manck and T. Ridley, *in preparation* (1998)